PROPAGATION LOSS IN SLOW LIGHT PHOTONIC CRYSTAL WAVEGUIDES

Sebastian Andreas Schulz

A Thesis Submitted for the Degree of PhD
at the
University of St. Andrews

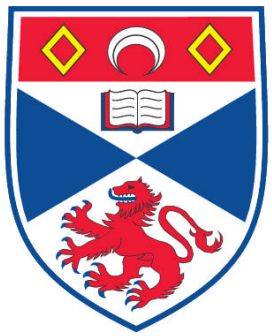

2012

Full metadata for this item is available in
Research@StAndrews:FullText
at:
http://research-repository.st-andrews.ac.uk/

Please use this identifier to cite or link to this item:
http://hdl.handle.net/10023/2837

This item is protected by original copyright

Propagation Loss in Slow Light Photonic Crystal Waveguides

Sebastian Andreas Schulz

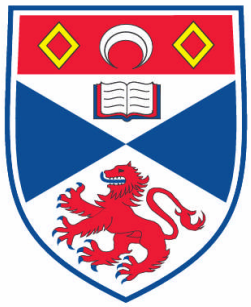

This thesis is submitted in partial fulfilment for the degree of PhD
at the
University of St Andrews

April 2012

1. Candidate's declarations:

I, Sebastian Andreas Schulz, hereby certify that this thesis, which is approximately 32000 words in length, has been written by me, that it is the record of work carried out by me and that it has not been submitted in any previous application for a higher degree.

I was admitted as a research student in October 2008 and as a candidate for the degree of Doctor of Philosophy in October 2008; the higher study for which this is a record was carried out in the University of St Andrews between 2008 and 2012.

Date ….....… signature of candidate …….....

2. Supervisor's declaration:

I hereby certify that the candidate has fulfilled the conditions of the Resolution and Regulations appropriate for the degree of Doctor of Philosophy in the University of St Andrews and that the candidate is qualified to submit this thesis in application for that degree.

Date ….....… signature of supervisor …….....

3. Permission for electronic publication: (*to be signed by both candidate and supervisor*)

In submitting this thesis to the University of St Andrews I understand that I am giving permission for it to be made available for use in accordance with the regulations of the University Library for the time being in force, subject to any copyright vested in the work not being affected thereby. I also understand that the title and the abstract will be published, and that a copy of the work may be made and supplied to any bona fide library or research worker, that my thesis will be electronically accessible for personal or research use unless exempt by award of an embargo as requested below, and that the library has the right to migrate my thesis into new electronic forms as required to ensure continued access to the thesis. I have obtained any third-party copyright permissions that may be required in order to allow such access and migration, or have requested the appropriate embargo below.

The following is an agreed request by candidate and supervisor regarding the electronic publication of this thesis:

Access to printed copy and electronic publication of thesis through the University of St Andrews.

Date ….....… signature of candidate ……..... signature of supervisor …….....

Acknowledgments

This PhD gave me the opportunity to meet and work with many great people, whom I would like to thank for all their support and inspiration.

I would like to thank Prof. Thomas Krauss for all the help and guidance that I received during my time in St Andrews, as well as all the great opportunities that I was offered. Next, I would like to thank Prof Michele Midrio and Dr. Chris Hooley for agreeing to be my examiners.

My PhD allowed me to work in a research group with excellent colleagues and great friends. I want to thank Dr. William Whelan-Curtin (Liam O'Faolain) and Dr. Daryl Beggs in particular for their patience when I started my PhD, as well as their continued advice. Additionally, I would like to thank Dr. Chris Reardon for his help with image processing software and his general comments on life. A big thank you to Dr. Karl Welna and Emiliano Rezende Martins for organising the group football matches.

One of the great opportunities that I was given, was the chance to work within the EU project Splash, during which I met many great minds. Out of these, I would like to thank Prof Andrea Melloni, Prof. Kobus Kuipers and Prof Philippe Lalanne for all their inspiration and support. Additionally, I would like to thank Prof Andrea Melloni for welcoming me to his lab at the Politecnico Di Milano.

I would also like to thank Dr. Sigmar Roth, and all the members of his group at the Max Planck Institute for solid state research in Stuttgart, for the opportunities given to me before I started my PhD. These convinced me that Physics was the way forward for me.

Outside of the lab, I would like to thank all my friends in St Andrews for the support, and distractions, they offered me during my time here. In particular I want to thank Jess, Yann, Darran, Feli, Christine, Graeme, Symke and James. Life in St Andrews would have been boring without you.

Last but not least, I would like to thank my parents, Andrea and Jürgen as well as my brother and his wife, Christoph and Claire for all their support and love. Christoph, without you I never would have come to St Andrews.

Thank you all

Abstract

The field of nanophotonics is a major research topic, as it offers potential solutions to important challenges, such as the creation of low power, high bandwidth interconnects or optical sensors. Within this field, resonant structures and slow light waveguides are used to improve device performance further. Photonic crystals are of particular interest, as they allow the fabrication of a wide variety of structures, including high Q-factor cavities and slow light waveguides.

The high scattering loss of photonic crystal waveguides, caused by fabrication disorder, however, has so far proven to be the limiting factor for device applications. In this thesis, I present a detailed study of propagation loss in slow light photonic crystal waveguides.

I examine the dependence of propagation loss on the group index, and on disorder, in more depth than previous work by other authors. I present a detailed study of the relative importance of different components of the propagation loss, as well as a calculation method for the average device properties.

A new calculation method is introduced to study different device designs and to show that photonic crystal waveguide propagation loss can be reduced by device design alone. These "loss engineered" waveguides have been used to demonstrate the lowest loss photonic crystal based delay line ($35\,dB/ns$) with further improvements being predicted ($< 20\,dB/ns$).

Novel fabrication techniques were investigated, with the aim of reducing fabrication disorder. Initial results showed the feasibility of a silicon anneal in a nitrogen atmosphere, however poor process control led to repeatability issues.

The use of a slow-fast-slow light interface allowed for the fabrication of waveguides spanning multiple writefields of the electron-beam lithography tool, overcoming the problem of stitching errors.

The slow-fast-slow light interfaces were combined with loss engineering waveguide designs, to achieve an order of magnitude reduction in the propagation loss compared to a W1 waveguide, with values as low as $130\,dB/cm$ being achieved for a group index around 60.

Publications arising from this work

Journal Papers

1. J. Li, L. O'Faolain, S. A. Schulz and T. F. Krauss "Low Loss Propagation in Slow Light Photonic Crystal Waveguides at group indices up to 60" *submitted to Photonics and Nanostructures-Fundamentals and Applications*

2. H. Lotfi, N. Granpayeh and S. A. Schulz "Photonic crystal waveguides with ultra-low group velocity" *accepted for publication at Optics Communications* (2012)

3. I. H. Rey, Y. Lefevre, S. A. Schulz, N. Vermeulen and T. F. Krauss "Scaling of Raman amplification in realistic slow-light photonic crystal waveguides" *Physical Review B* **84,** 035306 (2011)

4. L. O Faolain, S. A. Schulz, D. M. Beggs, T. P. White, M. Spasenović, L. Kuipers, F. Morrichetti, A. Melloni, S. Mazoyer, J. P. Hugonin, P. Lalanne and T. F. Krauss "Loss engineered slow light waveguides" *Optics Express* **18,** 27627 (2010)

5. S. A. Schulz, L. O'Faolain, D. M. Beggs, T. P. White A. Melloni and T. F. Krauss "Dispersion engineered slow light in photonic crystals: a comparison" *Journal of Optics* **12,** 104004 (2010)

6. M. Patterson, S. Hughes, S. Schulz, D. M. Beggs, T. P. White , L. O'Faolain and T. F. Krauss "Disorder-induced incoherent scattering losses in photonic crystal waveguides: Bloch mode reshaping, multiple scattering and breakdown of the Beer-Lambert law" *Physical Review B* **80,** 195305 (2009)

Proceedings

1. S. A. Schulz, L. O'Faolain, I. H. Rey, and T. F. Krauss, "Understanding Propagation Loss in Slow Light Waveguides," *in Slow and Fast Light,* OSA Technical Digest (CD) (Optical Society of America, 2011), paper SLTuB1.

2. T. F. Krauss, L. O'Faolain, S. Schulz, D. M. Beggs, F. Morichetti, A. Canciamilla, A. Melloni, P. Lalanne, A. Samarelli, M. Sorel and R. M. De La Rue, "Understanding the rich physics of light propagation in slow photonic crystal waveguides," *Proc. Soc. Photo Opt. Instrum. Eng.* 7612, 76120L (2010) (SPIE)

3. L. O'Faolain, S. Schulz, D. M. Beggs, T. P. White, A. Di Falco, A. Samarelli, M. Sorel, R. M. de la Rue, F. Morichetti, A. Canciamilla, A. Melloni and T. F. Krauss "Low loss dispersion engineered photonic crystal waveguides for optical delay lines" *Group IV Photonics*, 40-42 (2009)

4. L. O'Faolain, S. Schulz, D. M. Beggs, T. P. White, T. F. Krauss, A. Samarelli, M. Sorel, and R. M. D. L. Rue, "Losses in engineered slow light photonic crystal waveguides," *in CLEO/Europe and EQEC 2009 Conference Digest,* (Optical Society of America, 2009), paper CK6_3

Conferences attended

1. Advanced Photonics Congress, Slow and Fast light topical meeting (OSA), Toronto 2011, invited talk: "Understanding propagation loss in slow light waveguides"

2. SU2P Symposium (SUPA), St Andrews 2011, poster: "Loss and dispersion engineered photonic crystal waveguides"

3. PECS IX- The 9th international Photonic & Elcetromagnetic Crystal Structures Meeting, Granada 2010, talk: "How to make a Low-Loss Slow Light Waveguide"

4. PECS VIII- The 8th international Photonic & Elcetromagnetic Crystal Structures Meeting, Sydney 2009, poster: "Losses in engineered slow light photonic crystal waveguides"

Awards

1. 130 000JPY grant to attend the JSPS International Schooling on silicon photonics, Kyoto 2011

2. Best student presentation at the Slow and Fast light topical meeting of the OSA Advanced Photonics Congress, Toronto 2011

3. Best student group project during the 2011 silicon photonics summer school, St Andrews

4. 2nd Prize for 2nd year School of Physics and Astronomy PhD student talk, St Andrews 2010.

Contents

1 Introduction

"There's Plenty of Room at the Bottom"

Richard P Feynman

The overwhelming success of the electronics industry was made possible through the invention of the integrated circuit, and the resulting low cost, high yield production of silicon based chips. To achieve a similar success, the photonics industry also needs to move from expensive, large footprint and high power tabletop set-ups to integrated circuits.

Silicon nanophotonics allows the combination of a high refractive index material with a mature fabrication technology, providing an ideal opportunity to achieve high yield production of low cost, low power consumption components. These components can be used for a variety of applications, such as optical modulators, interconnects or sensors. Within the field of nanophotonics, photonic crystals (PhC) are a promising paradigm for a wide variety of applications, due to their ability to slow down light [1, 2].

1.1 Slow Light

The slow light effect has several consequences; first of all, it increases the optical length of devices, leading to a reduced footprint of optical switches [3] and delay lines [4, 5]. Additionally, the slow light effect increases the intensity of light inside the waveguide, leading to an enhancement of nonlinear processes, such as Raman scattering [6], third harmonic generation [7] or four wave mixing [8, 9]. These enhanced nonlinear efficiencies allow a smaller footprint and lower power operation than other nanophotonic designs, such as photonic wires.

Furthermore, photonic crystal waveguides are intrinsically lossless, increasing their appeal for integrated photonics applications. However, real structures have extrinsic propagation loss due to disorder induced scattering, the disorder being introduced during the fabrication process. This loss is further enhanced by the slow light effect. In this section, I will explain the basics of slow light enhancement for optical delay, modulators, nonlinear effects and propagation loss, providing the motivation for my research on methods aimed at reducing the propagation loss in these structures.

1.1.1 Optical delay

The basic principle of optical delay in photonic structures is very simple. Increasing the optical length of a device leads to a longer transit time for a pulse of light traveling through this device and therefore can be used to delay this pulse with respect to others. There are three simple ways of achieving optical delay. These are an increased physical length of the device, resonant cavities or a reduced group velocity of light inside the structure.

Increasing the physical length has the drawback that it leads to an increased device footprint and is very limited in its tunability. Unless the out- or in-coupling point can be moved physically, the device length is fixed, giving a fixed delay. On the other hand, if broadband waveguides such as optical fibres or photonic wires are used, a broad frequency range and therefore very short pulses can be delayed.

Cavities, on the other hand, offer the opposite properties. They can be very small with high quality factors, thus leading to a large delay with tiny footprint. For example, ring resonator and photonic crystal cavities with a footprint on the order of $> 100\,\mu m^2$ can be fabricated [10, 11], and cavity lifetimes close to 1 ns have been reported [5]. However, in order to achieve a large delay, a high Q factor is required. Since the Q factor can also be described as $Q = \frac{\omega}{\Delta\omega}$, this leads to a very narrow bandwidth, making cavities unsuitable for the delay of short pulses (e.g. a cavity with a Q-value of 1 million, operating at 1500 nm only has a 1.5 pm bandwidth).

Here, the third approach offers an intermediate solution. By using slow light photonic crystal waveguides, intermediate delays (one byte) can be achieved with usable bandwidths. Most photonic crystals have a broad wavelength region over which the group index is constant and approximately 5, before it increases rapidly. However, the advent of dispersion engineering (more in section 2.1.4) has allowed the fabrication of photonic crystal waveguides with a bandwidth of over 10 nm and a group velocity less than $1/30$ of the vacuum speed of light [12]. Using such low dispersion waveguides, continuously tunable delay lines have been demonstrated [4, 13]. The working principle of these devices is very simple. As the group velocity is decreased, the optical length of the device increases, delaying light traveling through it. The change of the group velocity can be achieved with different methods. One can tune the wavelength to sample different regions of the group velocity curve, either through tuning the wavelength of the input pulse [13], or by adiabatically tuning the wavelength once the pulse is inside the photonic crystal waveguide [14]. Alternatively, it

is possible to tune the group index curve of the structure by heating it. This second approach, combined with dispersion compensating structures also gives continuously tunable delay lines with large delay values (72 ps) [15].

1.1.2 Modulators

The slow light enhancement of modulators is very similar to that of optical delay lines. Most modulators proposed for photonic crystals are phase shift modulators. In a phase shift modulator, interference processes are used to produce either a zero, destructive interference, or a one, constructive interference. Here, I will use a Mach-Zehnder interferometer as an example. The incoming signal is split into two arms, which are later recombined and interfere with each other. If the phase difference ($\phi = nL\Delta k$, where n is the refractive index, L the physical length and Δk the shift in the wavevector) [16] between the two arms is either 0 or a multiple of 2π, constructive interference takes place, leading to a large signal intensity (see fig. 1). However, if the phase difference is an odd multiple of π, destructive interference takes place, leading to a zero. In order to switch between the two states, the optical length of one of the arms needs to be modified. In silicon, which has no direct electro-optic effect ($\chi^{(2)} = 0$), this change is achieved using either the plasma effect or the thermo-optic effect. In the first case, a change of carrier concentration leads to a refractive index shift, while, in the second case, the refractive index shift is achieved through a change in temperature. In both cases, the amount of power consumed is directly linked to the area over which the temperature, or carrier concentration, is being altered. Here, the slow light effect can be exploited to decrease the power consumption. The phase difference between the two arms in the MZ interferometer is dependent on the optical length of the structure, not the physical length. The slow light effect reduces the physical length required for the same difference in the optical path between the two arms, as the same Δn leads to a larger Δk. Therefore, a smaller area needs to be modulated, increasing the power efficiency of these modulators.

A strong reduction in the length of optical switches, by a factor of 36, to 5 μm [3], as well as optical modulators, by a factor of approximately 3, to 80 μm [17], was observed, by using PhC structures. Other groups, using PhC cavities, have achieved extremely low switching powers, around 100 fJ [18].

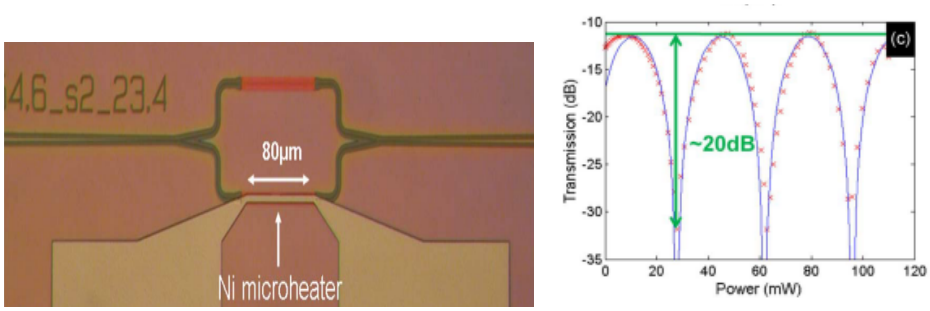

(a) (b)

Figure 1: **a)** Optical microscope image of a MZ modulator based on thermal tuning of photonic crystal waveguides. **b)** Graph showing the transmission through the modulator as a function of the power applied to the heater. Both calculated (blue) and measured (red) curves are shown. The multiple drops and peaks occur as the interferometer is tuned through multiple cycles, each adding an extra 2π phase shift. Both figures taken from reference [17] © 2010 IEEE.

1.1.3 Nonlinear optics

Slow light photonic crystals have already been used to demonstrate a wide range of nonlinear effects in silicon, such as third harmonic generation (THG) [7], four wave mixing (FWM) [8, 9] and self phase modulation (SPM) [19].

The scaling of the slow light enhancement of nonlinear process with the slowdown factor is strongly dependent on the nature of the process itself, although it is generally based on an increased intensity inside the slow light waveguide, given by:

$$I_\omega \propto \frac{P_\omega}{A_\omega} * S \tag{1}$$

where the slowdown factor $S = \frac{n_g}{n_\phi}$, n_g is the group index, n_ϕ is the phase index, P_ω is the power coupled into the waveguide and A_ω is the effective mode area, all at frequency ω. Therefore, any scaling of the process with the intensity of either the pump (or one of the resulting photons) relates directly to a scaling with the group index at the appropriate frequency.

For example, for THG three pump photons combine to give one signal photon at the third harmonic frequency, as shown in fig. 2. As all three pump photons are of identical wavelength, they have the same group index, while the signal photon is in a different, fast PhC mode. Therefore the THG efficiency scales with the cube of the pump intensity, leading to a S^3 enhancement if the pump photons are slowed down [7]. On the other hand, during

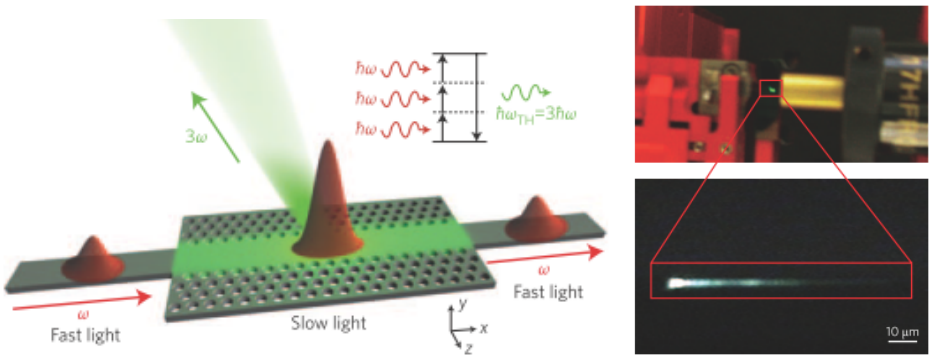

(a) (b)

Figure 2: **a)** Sketch showing the principle of THG. The photonic crystal acts as a grating for the green light, leading to a fast out-coupling of the light, before it is absorbed by the silicon. **b)** Optical image showing the green light emission from a sample. Figures taken from reference [7].

FWM, all four photons involved (two pump photons and one for each signal and idler), can be slowed down using dispersion engineered waveguides, as discussed in more detail in section 4.5.1. This results in an S^4 enhancement of the FWM efficiency [8, 9]. For a more detailed discussion of nonlinear effects in slow light waveguides, I suggest the review by Monat et al. [20].

It is easy to see the effect of propagation loss on these processes. The nonlinear effects require a high pump intensity. In the presence of high propagation loss, however, the pump intensity decays quickly, limiting the length over which the nonlinear conversion dominates over the propagation loss of the signal wavelength. Therefore, the useful device length is limited, a phenomena that has been discussed both for stimulated raman scattering (SRS) [21] and FWM [9] (see sections 4.5.1 & 4.5.2).

1.1.4 Propagation Loss

As will be discussed later, photonic crystals are intrinsically lossless, as long as the operating region lies below the light line (see section 2.1.1). However, due to finite fabrication quality, any real photonic structure has extrinsic scattering loss. Unfortunately, this scattering loss also increases as the light is slowed down (more information in section 2.4.2).

As a consequence of this extrinsic scattering, which generally results in propagation losses $> 10\,\mathrm{dB/cm}$ (although values as low as $2\,\mathrm{dB/cm}$ have been achieved [22]), most photonic crystal based devices are either based on PhC cavities [18, 23, 24], are very short ($< 100\,\mu\mathrm{m}$) [3, 17], or their performance is limited by propagation loss [25]. For example,

the delay line discussed in reference [15] has an estimated propagation loss of 100 dB/ns (24 dB/cm). Therefore, the reported delay of 72 ps has a loss of over 7 dB, i.e. approximately only 20 % of the incident power is transmitted. It is obvious that such a high loss is prohibitive for real life applications. Similarly, as already discussed above (section 1.1.3), the usable device length for nonlinear optics applications is limited by the propagation loss, as the pump is quickly depleted in the presence of high propagation loss.

Therefore, reducing the propagation loss, especially in the slow light region, is of utmost importance, if photonic crystals are to be used for the applications discussed above. In this thesis, I will show what the exact causes of propagation loss are and discuss the theoretical background required to describe the scaling of propagation loss with group index. I will then clarify the impact of important parameters in the theory of propagation loss, before moving on to show how improved design and fabrication of photonic crystals can reduce propagation loss. I will also show that these advances have been used to improve measurements and applications of photonic crystals.

1.2 Aim of my work

The aim of my work was to increase our understanding of propagation loss in photonic crystal waveguides and to investigate methods of fabricating samples with reduced propagation loss.

This aim was to be achieved through the study of loss in a variety of types of waveguides, including the standard W1 waveguide as well as different dispersion engineered waveguides. Additionally, novel techniques for improved sample fabrication were investigated.

The improved fabrication techniques and understanding of the problem could then be combined to yield better, which in the context of this thesis means lower loss, photonic crystal waveguides, for the use in optical delay lines and in nonlinear experiments.

2 Concepts and technology

"If I have seen further it is by standing on the shoulders of giants"

Isaac Newton

In order to be able to address the problem of propagation loss in photonic crystal waveguides, we need to properly understand the physical concepts and technologies underlying these structures. In the first part of this chapter, I will give an introduction to slow light in photonic crystal waveguides. A discussion of suitable figures of merit for slow light waveguides and of dispersion engineering follows. The second part of this chapter discusses the fabrication and measurement techniques used during my project, as well as the origin of disorder in photonic crystal waveguides.

2.1 Concepts

2.1.1 Photonic crystal waveguides

The concept of a photonic crystal, as first discussed in 1987 [26, 27], does not in itself introduce new physics. However, it combines the well known effect of an optical stop-band with the language of solid state physics. The resulting description of optical systems has led to new insight into the propagation of light in one, two and three dimensional periodic systems. In my work, I focus exclusively on 2 dimensional photonic crystal slab (PhC) waveguides. These structures consist of a line defect in a 2D photonic crystal slab. A 2D PhC slab consists of a periodic modulation of the refractive index in 2D. As with electronic crystals, where a periodic modulation of the electric potential leads to a bandstructure, the periodic modulation of the refractive index leads to transmission bands for light. More importantly, it also leads to a region in the dispersion curve where no mode exists, i.e. the photonic band gap (PBG). The most common structure, for 2D photonic crystals, is a triangular lattice of holes (air or other low refractive index materials) in a semiconductor (high refractive index) [28]. Such a slab has a bandgap for transverse electric field (TE) polarized light (see fig. 3). Here I would like to clarify that I am using the same nomenclature as Joannopolous & Johnson in their book "Molding the flow of light" [29]. In this nomenclature TE polarisation refers to light where the electric field oscillates in the plane of the photonic crystal (I will call this the x-y plane) and the z-component of the field is near zero. Since real structures

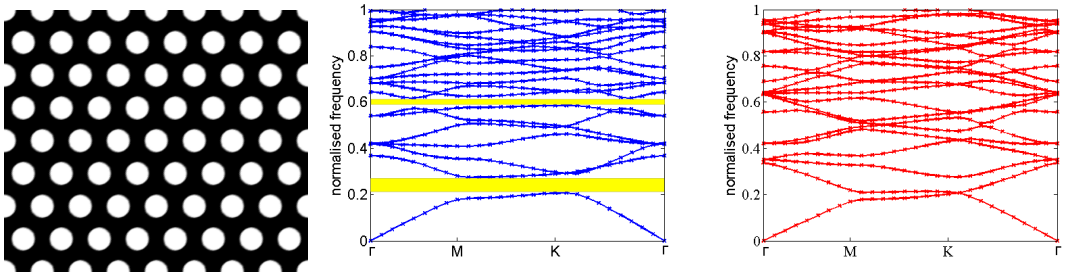

(a) (b) (c)

Figure 3: **a)** Sketch of a 2D photonic crystal, consisting of a triangular lattice of air holes in silicon. **b)** TE bandstructure of this PhC. There are 2 bandgaps visible, shown in yellow, one around $\omega = 0.2 - 0.3$ and one around $\omega = 0.6$. **c)** Corresponding TM bandstructure. The PhC displayed here has no TM bandgap.

have a finite height, the z-component is not exactly zero, but it is significantly smaller than the other components of the electric field and can be neglected during most calculations. Additionally, in this air hole configuration, the electric field is concentrated inside the high refractive index material, a necessity for the nonlinear processes and modulators discussed in the introduction.

If we introduce a defect into the photonic crystal, by removing or shifting specific holes, we create defect states that can lie inside the bandgap of the photonic crystal. Removing one or only a few holes leads to a cavity and by removing a single row of holes we form a so called W1 waveguide (see fig. 4) [30, 31, 32]. In this waveguide the photonic bandgap confines light inside the defect region, as it cannot penetrate into the photonic crystal cladding on either side. In the z-direction the light is confined by total internal reflection, as long as the device is operated below the light line. Therefore this planar waveguide achieves efficient confinement of light, with a very small mode volume, without requiring a 3D photonic crystal, simplifying the device fabrication significantly.

2.1.2 Slow light in photonic crystal waveguides

The slow light effect in these structures can be explained by considering the bandstructure from fig. 5 a) in more detail. The group velocity of light is defined as $v_g = \frac{d\omega}{dk} = \frac{c}{n_g}$, where n_g is the group index. Looking at the dispersion curve of the defect mode, we can see that the slope vanishes near the Brillouin zone (BZ) edge, giving a vanishing group velocity and therefore slow light (fig. 5). We get a more intuitive picture of the slow light effect by considering a ray picture of light propagation in the photonic crystal waveguide, as was

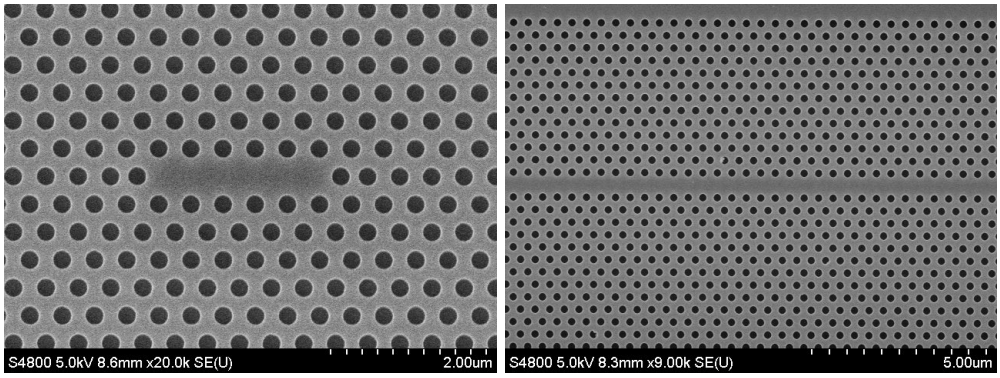

(a) (b)

Figure 4: **a)** SEM images of L5 cavity, where 5 holes have been removed. **b)** SEM image showing a W1 waveguide.

done by T. F. Krauss in 2007 [16]. Within the PhC waveguide, the light is scattered at each unit cell (this refers not to scattering from defects, but from the refractive index difference between the hole and slab material). The backscattered light and the forward propagating light interfere. If we are operating at the BZ boundary, then the light will be completely in phase, leading to a standing wave and a vanishing group velocity at the BZ boundary (see fig. 5). Operating slightly away from the BZ boundary leads to a very small phase difference between the two waves. A slow moving envelope, the slow light mode, is formed. As we move further away from the BZ boundary, the phase difference between the two waves increases, leading to an increased group velocity of the resulting envelope. For a typical W1 waveguide, the region below the light line yet away from the BZ boundary, the fast light region, has a group index of around 5. The group index increases rapidly as we approach the BZ boundary and enter the slow light region. In theory, the group velocity completely vanishes at the BZ boundary. However, in fabricated photonic crystals, the group index that can be observed is limited by high propagation loss and measurement limitations (more details in section 2.4.3).

Fig. 5 also demonstrates one of the major problems with slow light in W1 waveguides. At the BZ boundary, the group index increases rapidly, leading to a very narrow bandwidth for the slow light region and a very large second order (or group velocity) dispersion.

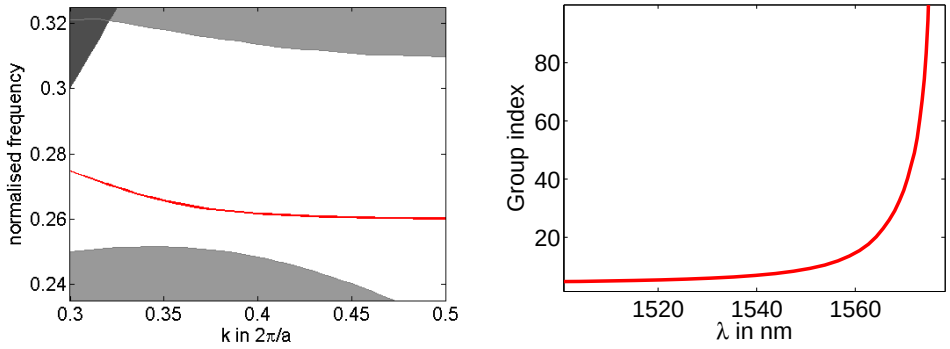

(a) (b)

Figure 5: **a)** Typical bandstructure of a W1 waveguide. The dark gray area is above the light line, while the light grey area represents the bulk PhC modes. The defect mode is shown in red. The reduced slope of the defect mode near the BZ boundary leads to an increased group index. **b)** Corresponding group index curve, showing the increase in group index for longer wavelength.

2.1.3 Figures of merit

Before I move on to the topic of dispersion engineering and how it is used to increase the bandwidth in slow light waveguides, we have to consider the figures of merit (FOM) that should be used to describe the structures. Suitable FOM are required to describe both the slow light performance and propagation loss of different photonic crystal waveguides.

As we have already seen, the group index (n_g) is generally used to describe the slow down of the light inside the waveguide. Another commonly used FOM is the delay-bandwidth product (DBP). This is generally defined as

$$DBP = \Delta t \Delta \omega \tag{2}$$

where Δt is the achievable time delay and $\Delta\omega$ is the bandwidth over which this delay can be achieved. The DBP is a very sensible FOM for slow light based on a narrow resonance, such as a photonic crystal cavity. In these structures, as the Q factor is increased, the loss per optical cycle reduces, increasing the delay that can be achieved. However, the increased Q factor also leads to a sharper resonance and therefore a reduction in the associated bandwidth. Since the Q factor is directly linked to the device design, the DBP can be used to describe the device performance. For slow light waveguides, whether coupled cavity or photonic crystal based devices, no such direct link between DBP and device design exists. Assuming that the device is not loss limited (i.e. the transmission of the device is high

enough to have a useful signal for subsequent processing/detection), then the bandwidth of a slow light waveguide is dependent on the device design only. However, the total achievable delay depends on both the device design (giving the group velocity reduction) and device length. Doubling the device length leads to a doubling of the achievable delay, without a reduction in the device bandwidth, resulting in a doubling of the DBP. Therefore the DBP is a poor figure of merit for slow light waveguides [33]. Instead, the group index bandwidth product (GBP, sometimes also referred to as normalised delay bandwidth product) should be used. It is defined as:

$$GBP = n_g \frac{\Delta\omega}{\omega} \tag{3}$$

where n_g is the group index, ω the central operating frequency and $\Delta\omega$ the bandwidth over which the group index has a $\pm 10\,\%$ variation [12]. Although $10\,\%$ is an arbitrary number, it has now been widely accepted and used in many publications, as it turns out that the $10\,\%$ variation gives an acceptable group velocity dispersion (GVD) in realistic structures. The advantage of this FOM over the DBP is its length independence. If I double the length of a PhC waveguide delay line, the achievable delay doubles, while both the group index and bandwidth remain constant. Therefore the GBP is not affected by such a change. Additionally, for a given device length, the DBP can be calculated from the GBP. The typical GBP of a W1 waveguide is around 0.01 (resulting in only 0.8 pm bandwidth for $n_g = 20$), but it can be much larger, > 0.3, for other waveguide designs, as I will show in the section on dispersion engineered waveguides (section 2.1.4).

The standard FOM for propagation loss is the loss per unit length (dB/cm). This FOM is very useful for many applications, such as nonlinear processes or modulators, where the critical design parameter is the device length that results in the optimal nonlinear conversion or the required phase shift respectively. However, for some applications, such as optical delay lines, the device length is secondary. Two different devices, one with $n_g = 20$ and length l and the second device with $n_g = 10$ and length $2l$ result in the same optical delay. However, since the propagation loss also depends on the group index, the two structures will have a different loss per unit length. Therefore, it is not immediately clear which of these waveguides is better suited for optical delay applications. To resolve this ambiguity, I introduce the concept of loss per unit time (dB/ns), as an additional figure of merit for slow light waveguides [13, 33].

The lowest propagation loss reported for photonic crystal waveguides was 2 dB/cm in the fast light region [22], with typical values for my fabrication being around $5-15$ dB/cm, giving $30-90$ dB/ns (there is a spread here, as different e-beam writers and different parameters for e-beam writing were used during my research).

2.1.4 Dispersion Engineering

Apart from propagation loss, the main limitation of slow light in W1 waveguides is the very narrow bandwidth of the slow light region. The rapidly changing group index, near the BZ boundary, leads to a large group velocity dispersion, resulting in pulse distortion for any signals traveling through such a device. However, through appropriate device design, the slow light bandwidth can be increased. The resulting waveguides are generally referred to as dispersion engineered waveguides and have a significantly lower GVD. There are many different mechanisms for dispersion engineering [12, 30, 33, 34, 35, 36], all based on the same principle. As shown in fig. 6, the mode of a W1 waveguide is the result of an anticrossing between two modes. The first mode is an index guided mode, while the second one is a gap guided mode. For index guided modes, the electric field is contained mainly within the defect region and very little of it samples the photonic crystal cladding on either side, the resulting distribution looks very similar to that of a waveguide based on a refractive index contrast. For the second, gap guided mode the field samples more of the photonic crystal region [30, 34]. Both modes have equal, in this case even, symmetry, leading to an anticrossing at the point where they would intersect (dotted lines in fig. 6). This anticrossing results in a changeover in the field distribution, from index guided to gap guided, and a curving of the bandstructure. The modified curvature of the bandstructure leads to a reduced slope and therefore a slow mode. To differentiate it from the slow light at the BZ boundary, it is often referred to as "anticrossing slow light". The slightly different field distributions in the two modes have a useful consequence. Because the extent to which they penetrate into the photonic crystal cladding varies, they react differently to changes in the design parameters. Changes to the waveguide width, or the radius of the first row, have a stronger effect on the index guided mode, while changes to subsequent rows have a stronger effect on the gap guided mode. Therefore, changes in these parameters can be used to influence the position and strength of the anticrossing, modifying the resulting slow light mode (see fig. 7). This process is called dispersion engineering.

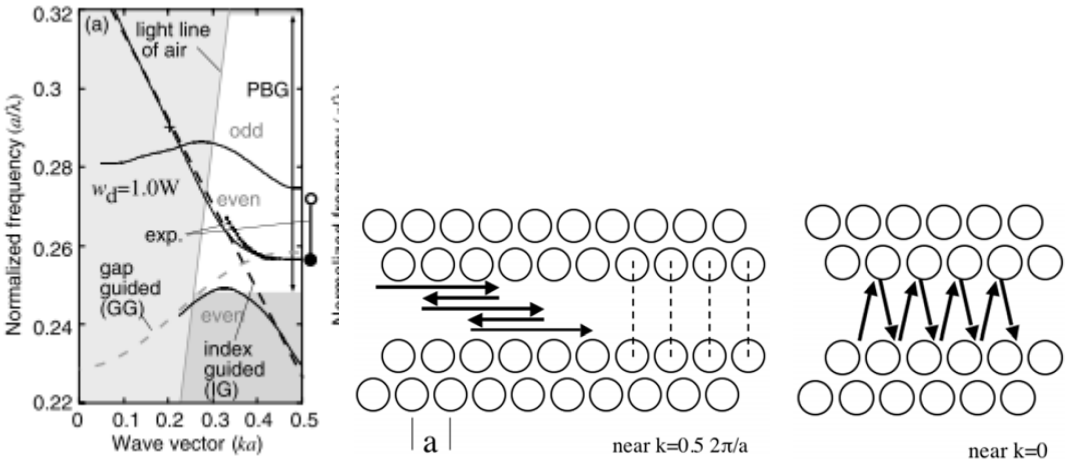

Figure 6: **a)** Sketch from Notomi et al. [30] showing the anticrossing between the index and gap guided mode for a W1 waveguide. By tuning the photonic crystal structure, the relative position of these two modes can be tuned, changing the bandstructure in the anticrossing region and leading to slow light away from the bandgap [12, 33, 35]. **b)** and **c)** Sketches from T.F. Krauss [16] showing the different guiding mechanisms that can lead to slow light in a PhC waveguide. **b)** Near the bandedge (left) the light is coherently scattered and interference of the forward and backward propagating modes leads to a slow moving envelope, the slow light mode. **c)** The PhC cladding has no cutoff angle, therefore light at near normal incidence is still guided. These modes, near $k = 0$, only have a very small forward component, leading to a slow light mode.

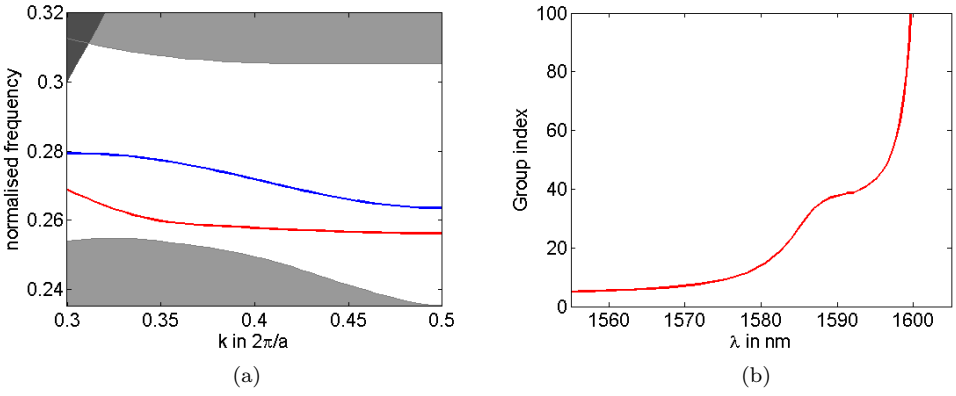

Figure 7: **a)** Bandstructure of a dispersion engineered waveguide. The odd waveguide mode is shown in blue, while the even mode is shown in red. Compared to a W1 bandstructure, the anticrossing has been shifted to a lower k-value (0.35), resulting in a wider slow light region. **b)** Corresponding group index curve, showing the slow light region around $n_g = 37$.

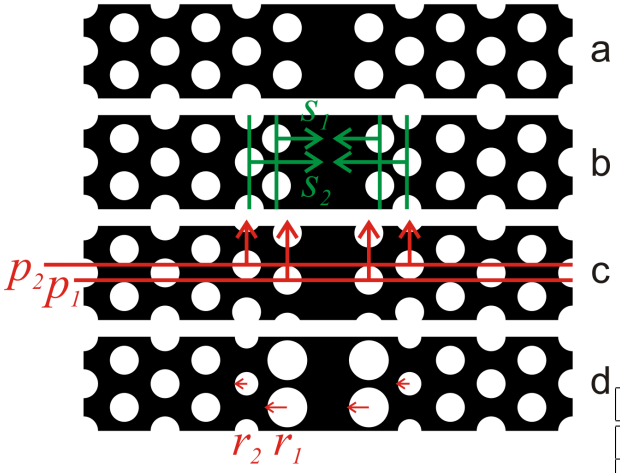

Slow light type	n_g	GBP
lateral hole shift	111	0.31
radius reduction	37	0.24
longitudinal hole shift	50	0.16

Figure 8: Left: Sketch showing different types of slow light waveguides. **a)** A standard W1 waveguide **b)**, **c)** and **d)** waveguides, where the anticrossing is modified by shifting rows of holes perpendicular to the waveguide (lateral hole shift), along the waveguide (longitudinal hole shift) and modifying the hole radius respectively.
Right: Table showing the highest measured group index and GBP for the dispersion engineering types shown here. The data is taken from reference [33] and presents the state of the art as of spring 2010.

The first mechanism explored for dispersion engineering was the variation of the waveguide width [30, 34]. However, in 2005, Kuramochi et al. showed that while a reduced waveguide width leads to better slow light performance, it also leads to a strong increase in the propagation loss, both in the fast and slow light region [37]. Therefore alternative methods were investigated, such as a change in hole radius of selected rows [35], shifting rows of holes lateral to the waveguide [12] and along the waveguide [36], as shown in fig. 8. In this work, most of the waveguides are fabricated using either type of hole position shift, as the hole position is easier to control during fabrication compared to the hole radius ($< 1\,\mathrm{nm}$ [38] error compared to $2 - 4\,\mathrm{nm}$ [3]) and the resulting waveguides have a good GBP. A comparison of the GBP achievable, with the varying dispersion engineering methods, is given in fig. 8.

2.2 Sample fabrication

In this section, I will outline the fabrication of photonic crystal waveguides (see fig. 9) in silicon on insulator (SOI) technology. The process is based on the approach from reference [39]. In my project, all samples were fabricated in SOI, consisting of approximately $220\,\mathrm{nm}$ Si

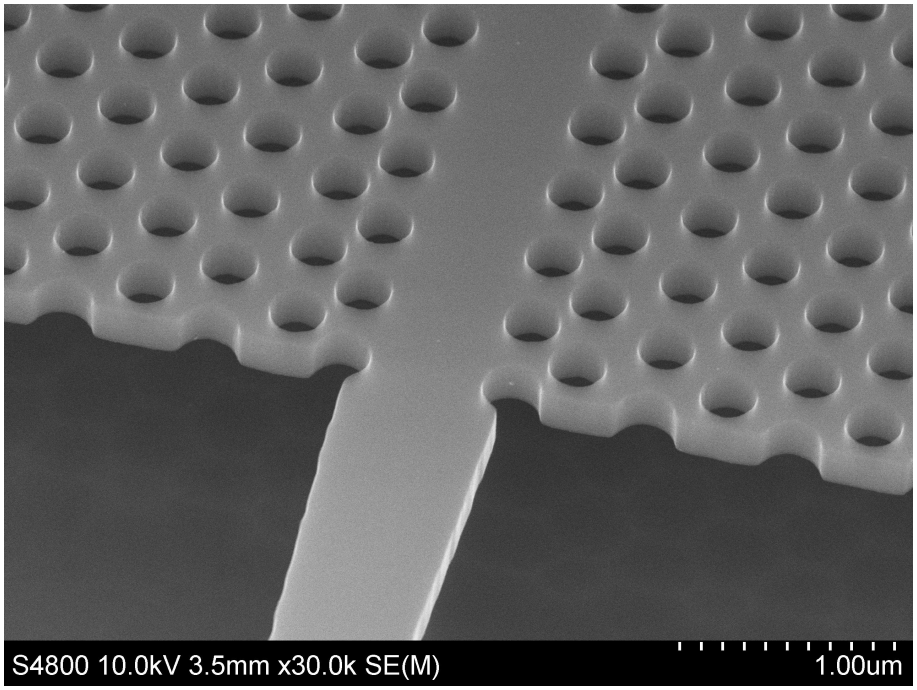

Figure 9: SEM image of a dispersion engineered waveguide after fabrication is completed.

on 2000 μm buried silicon dioxide. The underlying substrate is again silicon. The wafers are fabricated by SOITEC and can have a variation in the top silicon thickness of ± 5 nm, between wafers or different parts of the same wafer [40]. This thickness variation needs to be taken into account during fabrication, as it can shift the operating wavelength of PhC based devices.

The process flow is outlined in fig. 10. A suitably sized piece of silicon is cleaned before being spin-coated with electron beam resist. Electron beam lithography is then used to write the desired pattern in the resist layer. The exposed area of the resist is removed, using a developer, and the pattern transferred into the sample, by reactive ion etching (RIE). After removing any remaining resist, the sample is again coated with a new layer of lithography resist. In the next step, windows are opened in this resist, using either UV or electron beam lithography. These windows are then used to selectively remove the buried oxide layer underneath the photonic crystals, using hydrofluoric acid (HF), which etches silica but not silicon. After a final cleaning step, to remove the polymer resist, the sample is cleaved to form optical facets. All steps are described below in more detail.

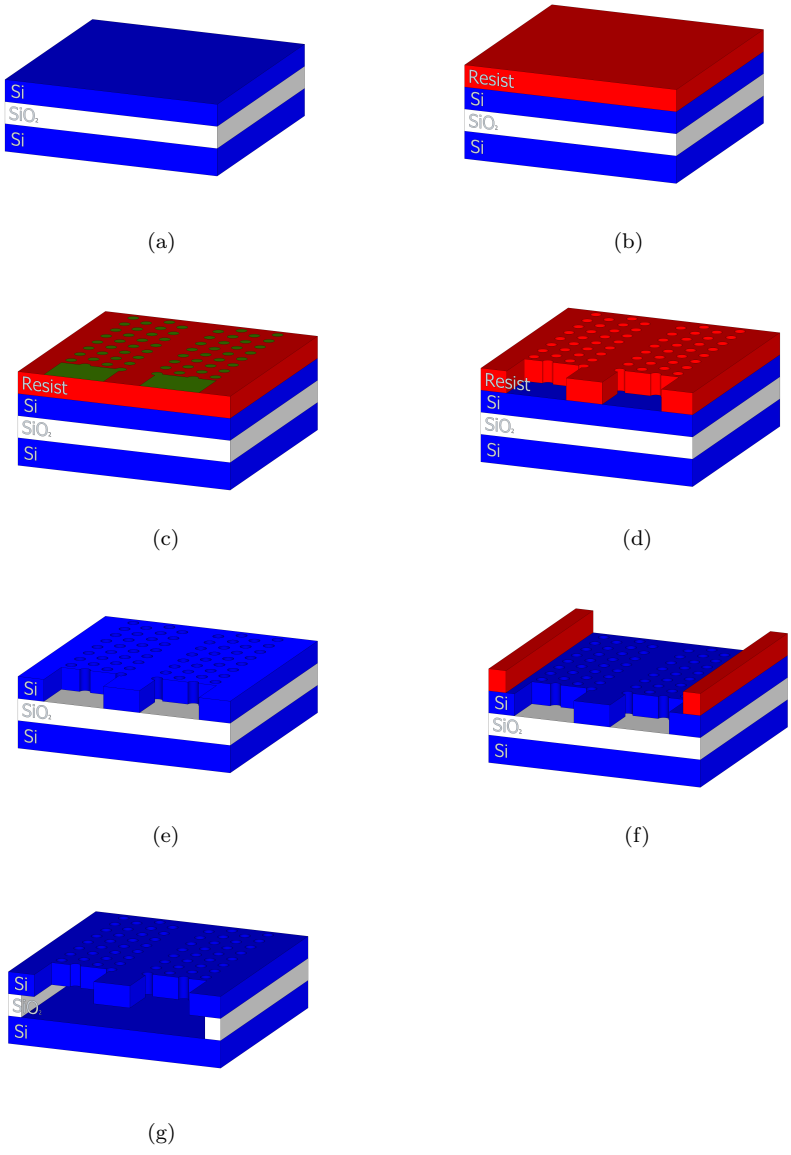

Figure 10: Schematic of the fabrication flow. **a)** A sample of SOI is cleaved from the wafer and cleaned. **b)** The sample is covered in e-beam resist. **c)** The resist is exposed. **d)** The exposed areas of the resist are removed using a developer. **e)** The pattern is transferred into the top silicon layer using a RIE etch and afterward the remaining resist is removed. **f)** The sample is again covered in resist and windows are opened above the photonic crystals. **g)** The photonic crystal membrane is formed, by removing the underlying SiO_2 using HF. The resist layer is removed, the sample is cleaned once again and then cleaved, to give optical facets.

2.2.1 Sample cleaning

A SOI wafer is first cleaved into suitably sized pieces that can be processed in the different machines used later. During this process, the sample can collect dust and other contamination that needs to be removed. Cleaning is achieved by placing the sample in a sonic bath in acetone, followed by isopropan-2-ol (IPA). The aceton removes most organic and inorganic contaminants, but it can leave a residue on the sample, which is removed by the subsequent IPA treatment. Once removed from the IPA bath, the sample is blow dried with nitrogen, to avoid redeposition of contaminants contained within the IPA.

While this cleaning recipe is generally sufficient, some processes require further cleaning, which can be achieved using a "Piranha" etch. The Piranha etch consists of a 3:1 mixture of sulphuric acid and hydrogen peroxide. This solution is a very aggressive and attacks any organic materials, and as such is well suited to removing contamination originating from organic chemicals, such as polymer resists. The sample is placed inside the piranha solution for 5 min, before being washed in distilled water (DI water). The piranha etch is followed by a standard cleaning in aceton and IPA, to remove any remaining (non organic) contamination.

2.2.2 Resists

I used two different positive resists for my work, i.e. ZEP-520A as electron beam lithography resist and S1818 as UV-lithography resist. ZEP has sufficient etching resistivity to allow for a direct transfer of the pattern from the resist into the silicon, without requiring a hard mask, while at the same time allowing high resolution lithography. Both ZEP and S1818 can be used as mask layers for the HF underetch described later. Using any resist normally follows the same procedure. First, the resist is deposited on the sample by spin-coating, then the solvents are driven from the resist by baking. Afterwards, the resist is exposed, and the exposed area is removed using a developer. In order to avoid overdeveloping the sample, any residual developer is removed, using a suitable solvent. Once the resulting polymer mask is not required any more, it can be removed using a resist stripper. Finally, the sample is cleaned once more, as described in section 2.2.1. The exact times and chemicals used are given in table 1.

resist	spin speed	thickness	baking time	baking temperature
ZEP-520A	$3200 - 3800$ rpm	$350 - 400$ nm	10 min	180^{o}C
S1818	5000 rpm	$\sim 2\mu$m	90 s	100^{o}C

resist	developer	development time	developing temperature	developer remover	resist stripper
ZEP-520A	Xylene	45 s	23^{o}C	IPA	1165
S1818	MF319	35 s	room temperature	DI water	aceton

Table 1: Table showing the recipes used for both ZEP-520A and S1818 resist. Both resist are spun for 1 min at the given spin speed. There is a range of spin speeds given for ZEP, as it can vary over time, as solvent evaporates from the resist. The resist thickness has to be kept in the given range to achieve optimal results during e-beam lithography and subsequent etching.

2.2.3 Electron beam lithograph

Most of my samples were fabricated on a hybrid RAITH ELPHY Plus/Leo Gemini 1530 electron beam writer, which has a maximum acceleration voltage of 30 kV and a $200*200\,\mu$m writefield. However, a few samples, especially those with longer waveguides, were fabricated at Glasgow University, using a VISTEC VB6 electron beam writer, with 100 kV acceleration voltage and a $1200 * 1200\,\mu$m writefield. With an electron beam writer there are several factors that contribute to the best resolution that can be achieved, as shown below:

$$d_f = 0.9 \left(\frac{R_t}{V_b} \right)^{1.5} \tag{4}$$

where d_f is the effective beam diameter at the silicon/resist interface, R_t is the resist thickness and V_b is the acceleration voltage. This equation assumes a spot size of approximately 1 nm on the top resist surface.

Additionally, the resolution is affected by the proximity effect; as the electrons impact on the silicon, they are scattered in random directions (see fig. 11). These scattered electrons expose the resist, too. Therefore, the electron beam exposes a resist area larger than the actual spot size, and each point gets an electron dose depending on the patterns in its proximity. This proximity effect needs to be taken into account when designing the samples. In our research group, the proximity error correction is done using Nanopecs, a software that calculates the proximity effect and adjusts the exposure dose of each object in the design pattern accordingly.

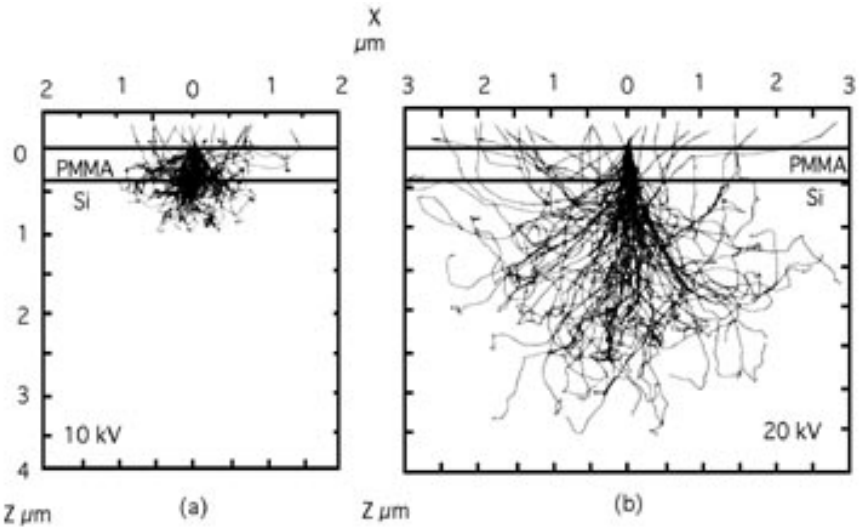

Figure 11: Monte Carlo simulations showing the scattering of electrons in a silicon substrate at e-beam lithography using **a)** 10 kV and **b)** 20 kV acceleration voltage. The spot size on the top of the resist does not correspond to the resist area that is exposed. Figures taken from reference [41] © 1975 IEEE

2.2.4 Reactive Ion Etching

All pattern transfer, from the polymer resist layer into the silicon slab, was done using reactive ion etching (RIE). During reactive ion etching, the sample is placed between two electrodes inside a vacuum chamber (see fig. 12). The top electrode has a small ring around it, through which gases can be injected into the chamber. An RF field is then applied to the electrodes and ionizes the gas, leading to the formation of a plasma containing the reactive ions, which etch the sample. The applied RF field also has a DC component, i.e. the DC bias that accelerates the ions towards the sample. The DC bias introduces a physical component, and downward directionality, to the etching process. However, unlike some other dry etching techniques, such as chemically assisted ion beam etching, the chemical and physical components of the RIE process are interlinked. The physical component is dependent on the downward acceleration from the DC bias. This DC bias is directly dependent on the RF power, which in turn also causes the plasma formation and, therefore affects the chemical component of the etch. The same applies for the choice of gases used and the etch pressure.

During my project, an equal volume mixture of SF_6 and CHF_3 was used to etch the photonic crystals in silicon. The etch pressure was around $5 * 10^{-2}$ mbar with 2 min etch time and a DC bias between -205 V and -215 V. This recipe was developed by Dr. Whelan-

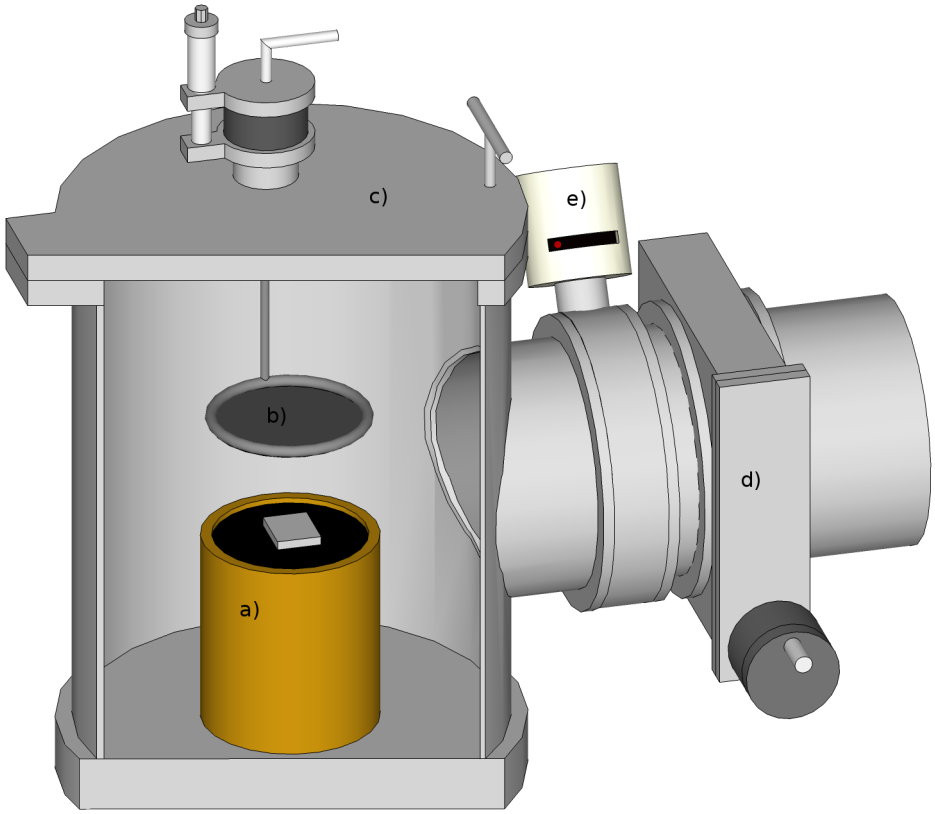

Figure 12: Sketch of the RIE chamber. **a)** and **b)** are the electrodes between which the sample is placed. Around electrode **b)** is the ring, through which the gases are injected into the camber. **c)** Lid for loading and unloading the sample. **d)** Gate valve connecting the RIE chamber to a turbo pump. **e)** Butterfly valve for pressure control during the etch process. Sketch courtesy of Dr. Reardon.

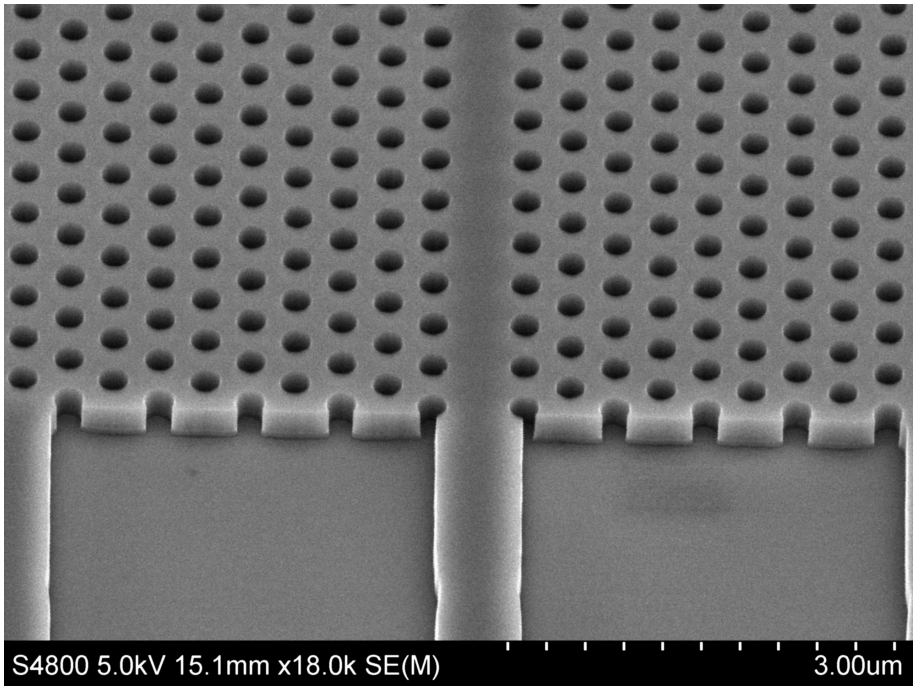

Figure 13: SEM image of a W1 waveguide before the HF etch.

Curtin (Dr. O'Faolain) and shown to produce some of the lowest loss photonic crystals in the world [39].

2.2.5 Hydrofluoric acid etching

After all these fabrication steps, the photonic crystal still resides on the buried oxide layer (see fig. 13). Such a structure has an asymmetry in the vertical direction, leading to coupling of the TE and TM like modes, and a severely reduced bandgap [29]. Therefore a symmetric structure is preferred. The vertical symmetry can be restored, either by covering the photonic crystal in silicon dioxide [42] or by removing the buffered oxide. An oxide top layer protects the photonic crystal from mechanical damage, and is much more stable than a thin silicon membrane, but it also has significant disadvantages. First of all, the reduced refractive index difference between the hole and slab materials gives a reduced bandgap, and a reduced bandwidth for slow light dispersion engineered waveguides [17, 29, 43]. Secondly, and possibly counterintuitively, a reduced refractive index contrast leads to an increased propagation loss, because the field is less confined and samples the sidewall roughness more strongly [42]. Therefore, the best results are achieved in photonic crystal membranes, where the buried oxide is removed at the end of the sample fabrication. Hydrofluoric acid is used

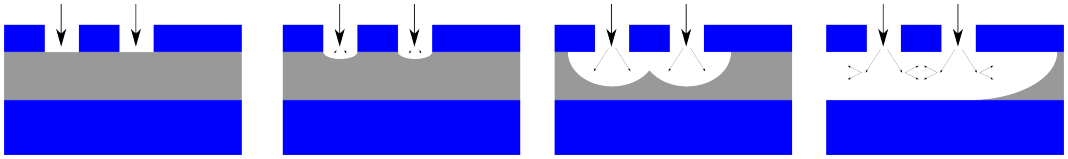

Figure 14: Schematic showing the HF etching procedure. The silica (grey) is etched by HF, while silicon (blue) is not. The etch is isotropic, resulting in an undercut under the silicon membrane (shown on the right of the last image)

to selectively remove the SiO_2, but not the Si. During the HF etch, at least 1 μm and ideally the full 2 μm of the underlying oxide are removed, to achieve optical isolation of the waveguide mode. Since HF etches silica isotropically, the etch will lead to a $1-2\,\mu$m wide undercut under any silicon structure on top of the buried oxide (see fig. 14). This undercut is very useful, as it ensures that not only the silica below the holes, but also that below the photonic crystal defect (waveguide) region is removed. However, since the access waveguides are only $3-4\,\mu$m wide, and are underetched from both sides, the resulting structure is mechanically unstable. Therefore, before the HF etch, the sample is covered in a polymer resist (see section 2.2.2). Windows are then opened in the resist above the photonic crystal, while the access waveguides are still masked. The etch mixture consists of 5:1 H_2O:HF, with an initial etch time of 15 min. The undercut is then checked and, if necessary, the sample is etched for an additional 5 min. This procedure is repeated, until a sufficient undercut is achieved. The etch time varies due to small deviations from the ideal etch mixture, slight variations in the hole size and variations in the ambient conditions. The undercut is checked repeatedly, as an excessive etch time leads to mechanically unstable samples, where the photonic crystal membrane or the access waveguides can collapse (see fig. 15). An insufficient etch time, on the other hand, leads to increased propagation loss as the evanescent tail of the waveguide mode samples the remaining buried oxide and scatters at the now rough oxide/air interface.

2.3 Roughness and Disorder

As already mentioned earlier, a photonic crystal mode below the light line is intrinsically lossless. However, in real structures, propagation loss is caused by disorder introduced during the fabrication process. In this section, I will discuss the different types and origins of the disorder present in real PhC structures. Furthermore, I will mention several standard procedures aimed at minimising the disorder introduced during the fabrication steps. To

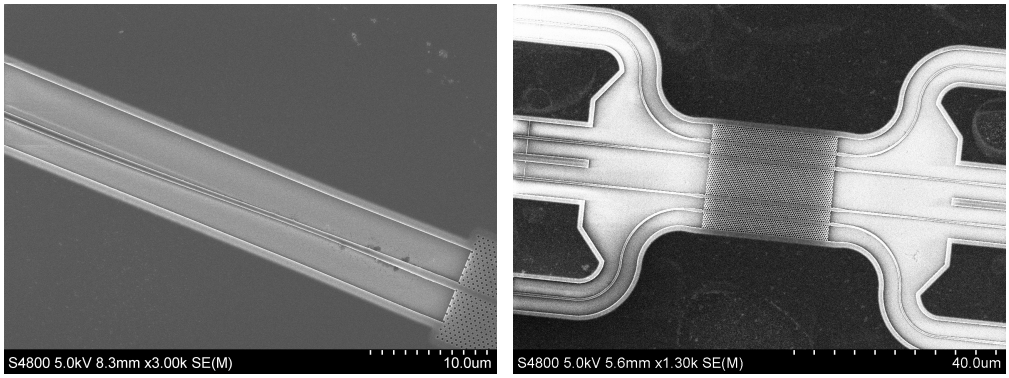

(a) (b)

Figure 15: SEM images of HF treated samples. The darker regions correspond to silicon supported by underlying buried oxide. The brightest region is the silicon back-substrate while the intermediate regions correspond to underetched silicon. **a)** Sample etched without HF mask. The access waveguide has been underetched too much and started bending, leading to a mechanical instability of the sample. **b)** Sample etched with appropriate HF mask. The photonic crystal and coupling regions are underetched, while the main body of the access waveguides is still supported by buried oxide. The resulting structure is mechanically stable and suitable for optical measurements.

begin with I will clarify that, in this context, disorder refers to any deviation of the fabricated structure from the ideal photonic crystal design, due to both random and systematic errors in the fabrication process.

The two fabrication steps, which are the main origin of disorder, are the electron beam lithography and the reactive ion etch (sections 2.2.3 & 2.2.4 respectively). Any disorder introduced during the electron beam exposure, or subsequent resist development, is transferred into the silicon slab during the pattern transfer. Additionally, a poor etch recipe can lead to further disorder, in the form of sidewall roughness, being introduced during the etch step. All this disorder contributes to the extrinsic scattering loss and is enhanced by the slow light effect.

2.3.1 Disorder due to electron beam lithography

The disorder introduced during the electron beam exposure can belong to one of three different categories. These categories include deviations in the hole radius, the hole position or the hole shape compared to the ideal design, as shown in fig. 16. The three different categories have a different physical origin, as explained below.

The variation in hole shape is due to the polymer resist used, as well as noise on the e-beam writer, both the electron source and the beam control units. During the e-beam

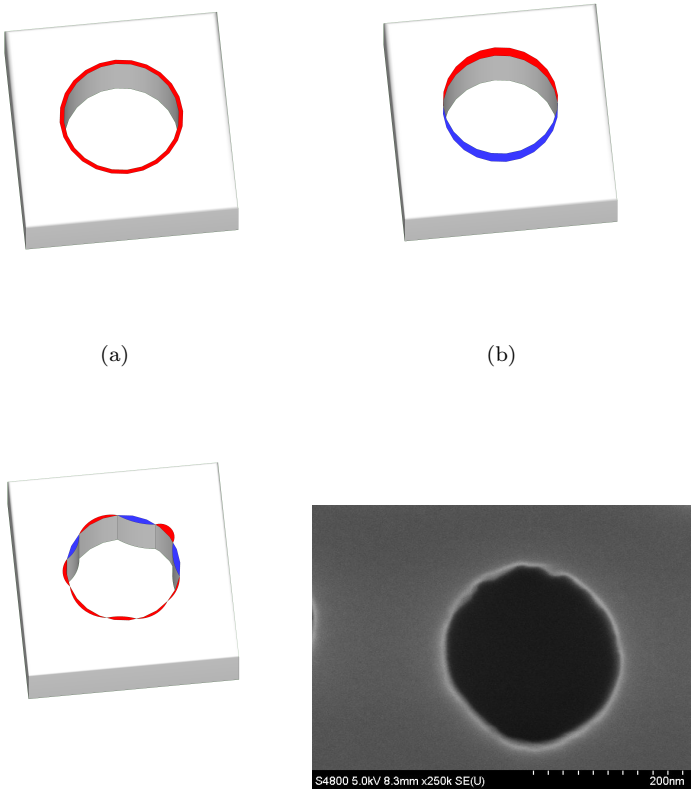

Figure 16: Sketches showing the different types of disorder that can exist in a photonic crystal system. Red areas represent regions that should be made of slab material but are hole material and vice verse for blue areas. **a)** An increase in the radius of a single hole. **b)** A hole position error. **c)** A variation of the hole boundary, generally due to the finite resolution of the electron beam resists used. **d)** SEM image of a circle that has a distorted shape, caused by the transfer of an imperfect mask pattern into the silicon slab.

exposure, the polymer chains are broken into smaller components by the electrons and these elements have a finite chain size. Therefore an exposed line or circle is never perfect and instead has deviations from the ideal structure. Additionally, noise on the e-beam writer, both the electron source and the beam control unit can lead to a variation in the hole shape. During the subsequent etching step, these irregularities in the mask are transferred into the silicon layer and result in irregularly shaped holes, as shown in fig. 16. The resist used during my project, ZEP-520A, was chosen since it has a good mixture of etch resistance and small chain size, resulting in high resolution, low disorder devices.

The variation in hole radius is generally due to a deviation of the dose received by the resist from the ideal exposure dose. Near the sample edges, the resist thickness can increase, forming so called edge beads, therefore slightly larger than necessary samples are normally

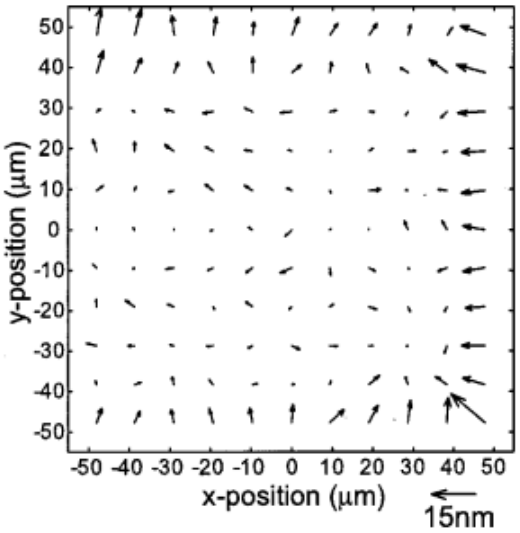

Figure 17: Graph showing the pattern positioning error within a 100 μm writefield. From reference [44].

used for the lithography step. In this case, all devices can be placed in the centre of the sample, where the resist thickness is more uniform, away from the edge beads. However, even with this precaution, variation in the hole radius can occur, due to inaccuracies during proximity correction. In our fabrication, each circle is treated as one object and cannot be split into smaller parts during the proximity correction. Therefore the complete circle receives the same electron dose, while, in the ideal case, the dose should vary slightly across a hole. The second origin of radius disorder is the statistical fluctuation in the beam current during the electron beam exposure.

The hole position disorder has several origins, too. As with all processes, the positioning of each hole, achieved by deflecting the electron beam using magnetic coils, only has a finite accuracy. This accuracy leads to a sampling noise, as the hole position is locked onto the e-beam grid. Additionally, there is a random variation in the hole position due to noise on the magnetic coils used to deflect the electron beam. This shift increases as the holes are closer to the edge of the writefield [44], as shown in fig. 17.

The second origin, which can also lead to errors in the hole shape of some holes, is called the stitching error. When a feature exceeds the size of the writefield, the area that can be exposed by deflecting the beam using magnetic coils, the stage is moved to a new position to continue exposing the feature. This movement is less accurate than the deflection of the beam and can lead to positioning errors at the borders between two writefields (see fig. 18).

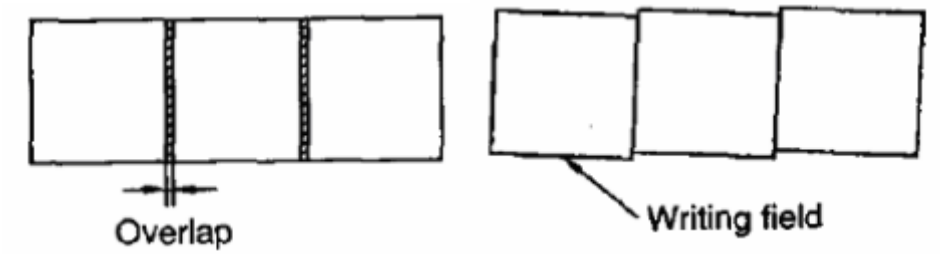

(a) (b)

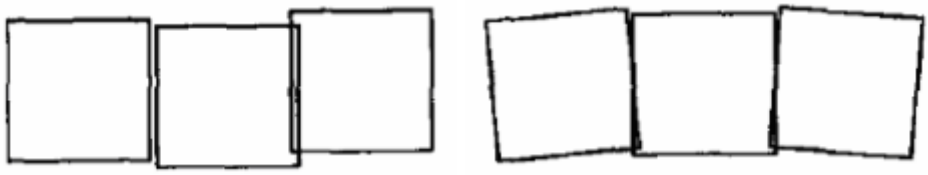

(c) (d)

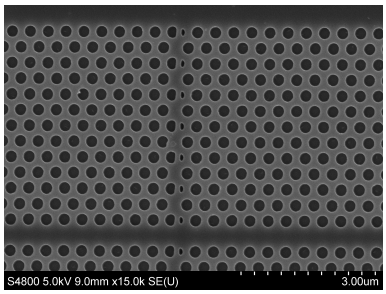

(e)

Figure 18: Sketches showing the different possible stitching errors. **a)** overlapping writefields **b)** rotated writefields (**a)** and **b)** are both systematic errors) **c)** shifts in the writefield due to limited resolution when stage position is determined **d)** stage rotation (**c)** and **d)** are random errors) [45] **e)** SEM image of a stitching error leading to hole deformation, caused by a slight gap between two adjacent writefields.

These stitching errors are a large defect, on the length scale of a PhC, and as such can lead to significant propagation loss.

2.3.2 Disorder due to reactive ion etch

As already mentioned in section 2.2.4, the reactive ion etch has both a chemical and a physical component. It is important to balance both of these components through an appropriate etch recipe. An etch that is predominantly chemical loses directionality, leading to an underetch of the resist mask, a widening of the bottom of the photonic crystal holes or curved sidewalls. If, on the other hand, the physical component dominates the etch, then the silicon is effectively sputtered and not removed from the sample. Therefore, it can rede-

posit at the bottom of the hole, leading to an angled sidewall or redeposit on the sidewalls themselves. Both represent deviations from the ideal photonic crystal structure and as such represent disorder leading to scattering losses. Additionally, the angled sidewalls destroy the symmetry of the structure and can lead to TE-TM conversion.

Fig. 19 shows several SEM images of good and poor etch results. In fig. 19 a) and b) we can see the effect of a physical etch. In a), the etch resulted in sidewalls that curve in at the bottom, while b) shows roughness on the sidewall due to redeposition of previously etched material. In c), on the other hand, we can see the sidewall roughness caused by poor e-beam exposure. In this exposure the electron dose was slightly too low, leading to highly disordered edges. Upon etching, this roughness in the etch mask is then transferred into the silicon itself, resulting in vertical ridges running the whole height of the sidewall. To contrast these images, d) shows an example of a good etch with vertical sidewalls and no recognisable sidewall roughness. Here, it has to be emphasised that the roughness present in state of the art photonic crystal waveguides has an rms value of less than 2 nm [38] (see section 3) and therefore is very difficult to recognise on a SEM image.

2.4 Measurement techniques

During my project I used four different optical measurement techniques, which are all based on the transmission of light through a photonic crystal or wire. In addition to these optical measurement techniques, samples were examined using optical and scanning electron (SEM) microscopy.

2.4.1 Transmission measurement

The most basic measurement that can be performed on a photonic crystal waveguide, or wire, is the measurement of the transmission through the structure. For a photonic wire waveguide, this consists of coupling light from a source to the waveguide and then collecting the transmitted light at the output, before examining it using an optical spectrum analyser (OSA). For a photonic crystal waveguide the measurement is very similar, the only difference is that light is not coupled directly into the photonic crystal, but first into an access waveguide. Similarly, the transmitted light is coupled into an access waveguide and from there to the OSA. Although this sounds very simple, there are several issues that need to be addressed when performing this measurement. The main issue is the small size of a single

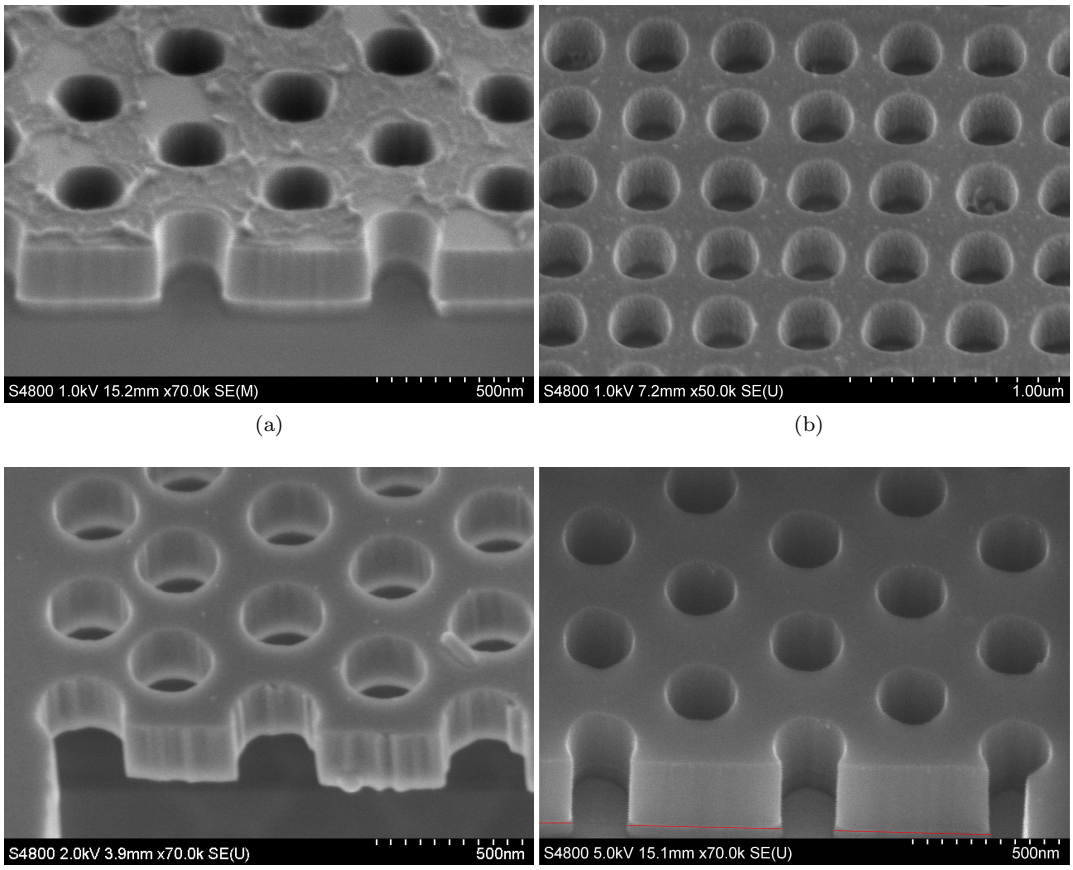

(a) (b)

(c) (d)

Figure 19: SEM images showing **a)** etch with angled sidewalls (the sample also was a small resist layer remaining on the top surface that was subsequently removed) **b)** sidewall roughness caused by redeposited material. **c)** sidewall roughness caused by mask imperfections that are transferred into the sample. **d)** A good etch with low sidewall roughness and straight sidewalls. This sample is still on the buried oxide layer ($Si - SiO_2$ interface highlighted in red) and a small angulation of the etched oxide walls is visible. However this layer is removed before measurements and therefore does not affect the sample quality.

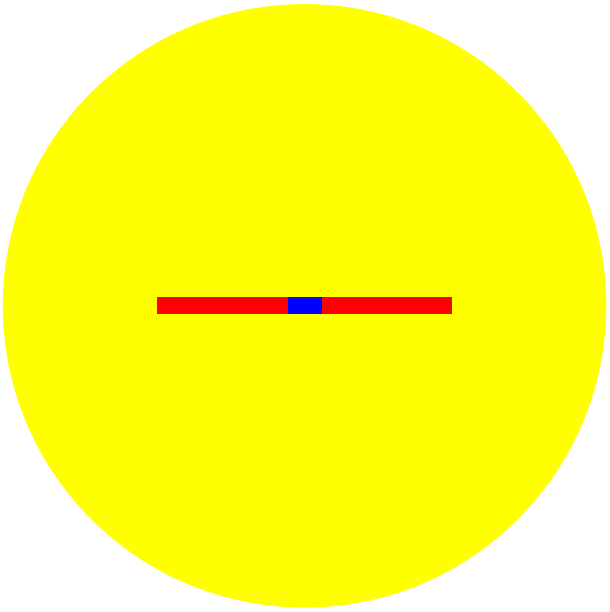

Figure 20: Sketch showing the relative size of a single mode fibre core (yellow, 8.2 μm core diameter), a wide access waveguide (red) and a single mode photonic wire (blue).

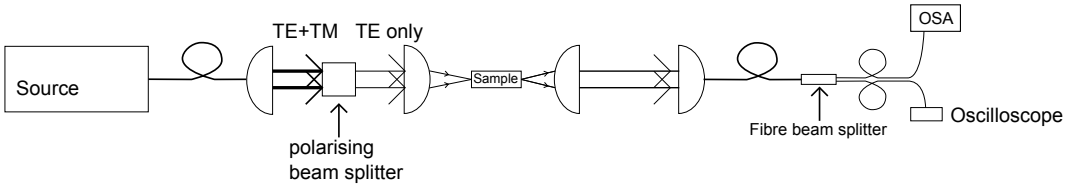

Figure 21: Sketch of the transmission measurement setup. All lenses are mounted on 3-axis stages for alignment optimisation. The signal on the oscilloscope is used during sample alignment and the OSA is used to measure the spectrum.

mode photonic waveguide and therefore the mismatch with a fibre mode (see fig. 20). This size mismatch affects both the in and out coupling of light from the sample. Additionally, the polarisation control (the photonic crystals discussed here only have a bandgap for TE like modes), as well as variations of the source spectrum with varying output power have to be considered. During my project, I used a free space coupling setup to inject light into and collect light from the sample. In this setup, which is shown in fig. 21, the light from a fibre coupled source is collimated using a lens. The collimated beam is then passed through a polarisation beam splitter, allowing only the TE mode to pass towards the sample, while the TM mode is dumped onto a beam blocker. The TE polarised light is then focused onto the cleaved facet of the sample, using a second lens. After passing through the sample, a third lens is used to collect and collimate the out-coupled light. A fourth lens focuses the light onto the facet of another fibre, which is connected to a 3 dB fibre splitter, the two

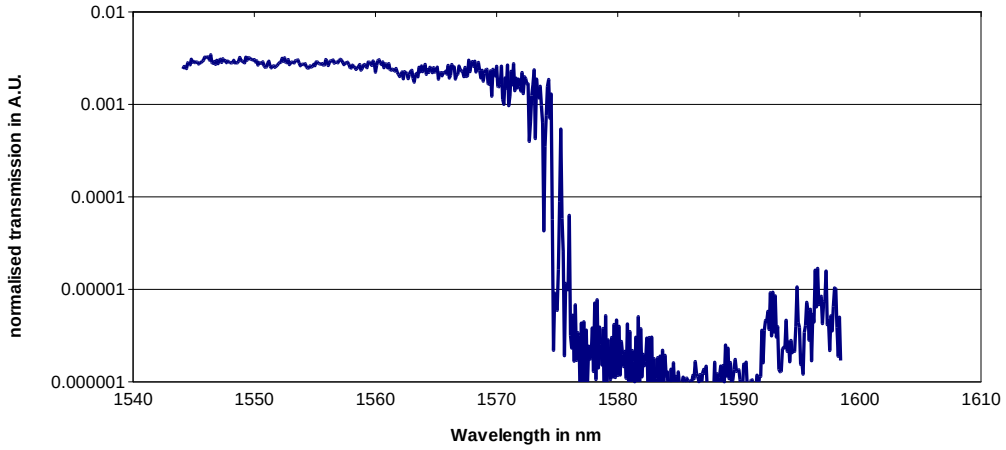

Figure 22: Example of a transmission measurement for a PhC waveguide. The transmission is normalised to the source spectrum.

output ends of which are connected to the OSA (with a maximum resolution of 0.01 nm) and a photo diode. The sample is mounted on a translation stage, while all four lenses are on three axis micro-blogs, which can be controlled to within 50 nm accuracy. The photo diode is connected to an oscilloscope and the trace on the oscilloscope is used to measure the transmitted power during the alignment procedure. The source is then coupled directly into the OSA to measure the source spectrum and allow for a normalisation of the measured transmission spectrum, as shown in fig. 22.

In order to improve the coupling efficiency, wide access waveguides of $3-4\,\mu$m width are used. When coupling light to a photonic crystal, these wide waveguides are tapered down to a 450 nm wide single mode section, using a 300 μm long adiabatic taper (see fig. 23). This single mode waveguide is then widened to match the width of the photonic crystal line defect, to achieve optimal coupling. This setup results in approximately 10 dB coupling loss at each facet.

Coupling at high group indices When injecting light directly into a slow light waveguide from a photonic wire, the coupling efficiency is strongly n_g dependent and reduces significantly for higher group index values [46, 47]. Therefore all my samples include mode conversion interfaces [33], as shown in fig. 23. The coupling region works as follows; the stretched lattice period of the initial photonic crystal section shifts the defect mode to a longer wavelength. The resulting mode of the initial PhC section has a lower group index

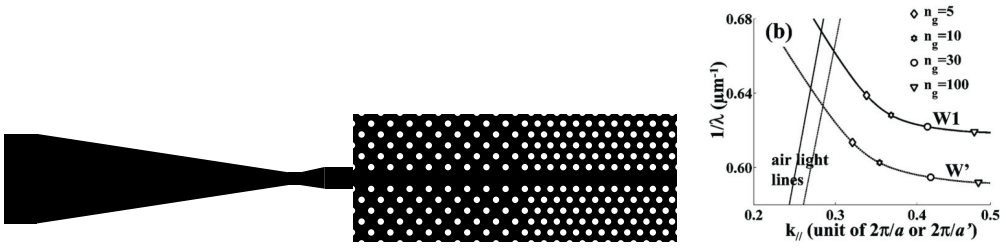

(a) (b)

Figure 23: **a)** Sketch of the elements used to reduce coupling losses into PhC waveguides. On the left is an adiabatic taper from a wide access waveguide to a short single mode section. This section is then tapered out to match the width of the W1 waveguide. For the first section of the photonic crystal, the lattice is stretched along the waveguide to give a better coupling efficiency, followed by the normal W1 waveguide. Sketch is not to scale. **b)** Graph showing the defect mode for both the stretched (dotted line) and normal (solid line) lattice regions (from reference [48]).

than the main waveguide (see fig. 23 b) and light is initially coupled from a photonic wire to a fast light waveguide [48, 49]. At the second interface, the lattice changes from the stretched to a normal lattice, and light couples from a fast photonic crystal mode to a slow photonic crystal mode. At this interface a nearly complete transfer of power from the fast to the slow light mode occurs. Initially, part of the incident light from the fast-mode couples directly to the slow mode of the bulk waveguide, while the remaining power of the fast mode couples to evanescent modes. As the distance from the interface increases, the evanescent modes decay and the power contained within them is coupled into the slow light mode, leading to very high ($> 90\,\%$) coupling efficiencies [48, 50].

2.4.2 Propagation loss measurements

To measure the propagation loss of photonic crystals, and wires, two different measurement techniques, namely the Fabry-Perot interference and the cutback measurement, were used. Both techniques have in the past been used to measure propagation loss for both types of waveguides. In my project, however, the propagation loss of photonic wires was measured exclusively using the Fabry-Perot interference techniques, while that of photonic crystals was measured using the cutback method.

Cutback measurement The cutback measurement is conceptually the easiest measurement of propagation loss in waveguides. The first loss measurement of a photonic crystal waveguide using this technique was performed by C. Smith et al. [51].

In this measurement, one simply measures the transmission through waveguides of vary-

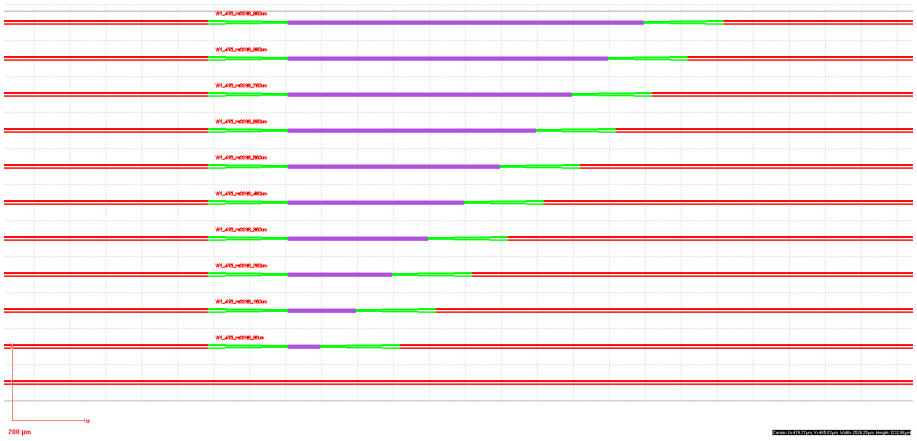

Figure 24: Layout of a typical cutback measurement chip. The wide access waveguides (red) are tapered down through the use of adiabatic tapers (green). The photonic crystals of varying length are shown in purple. The transmitted light is again coupled through adiabatic tapers to an access waveguide. Mode conversion interfaces, as shown in fig. 23, are used.

ing length. After normalising the transmission to the source spectrum, the linear fit of $< lnT >$ as a function of L gives the propagation loss according to the equation below:

$$\langle \ln T \rangle = -\alpha L \tag{5}$$

where T is the optical transmission, L is the device length and α is the propagation loss in dB/cm [52].

While this is very simple in theory, there are several complications that affect this measurement in practice. First of all, while one can easily fabricate photonic crystal waveguides of varying length, the total length of a sample on which the devices are located has to be constant for each fabrication run. Therefore, the photonic crystal length was varied across the sample and the length of the access waveguides was changed accordingly, to keep the total length constant, as shown in fig. 24. When using eqn 5 to extract the loss coefficient α for the photonic crystals, the resultant loss is not the real propagation loss of the photonic crystal waveguides, but instead the difference between the loss of the photonic crystals and the access waveguides ($\alpha_{meas} = \alpha_{PhC} - \alpha_{access}$). Additional blank waveguides, with the same dimensions as the photonic crystal access waveguides, are included on the sample and their propagation loss is then measured using the Fabry-Perot method described below. This loss value is then added to the initial value of α_{meas} to give the real propagation loss of the PhC waveguides, as shown in fig. 25.

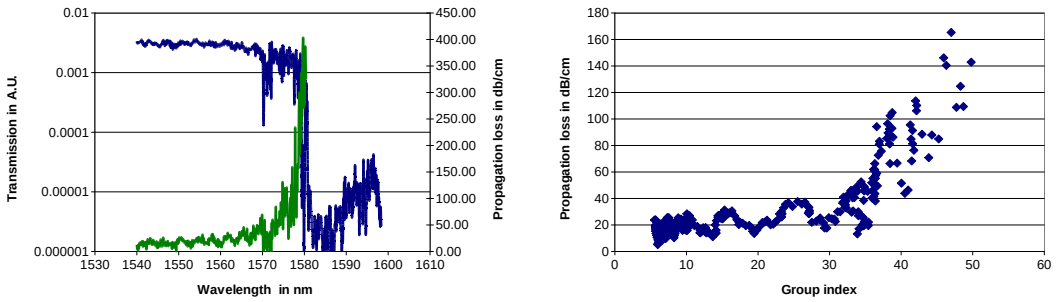

(a) (b)

Figure 25: **a)** Graph showing a typical transmission spectrum (blue) and propagation loss curve (green) of a PhC waveguide, taken during a cutback measurement. The transmission curve is normalised to the source spectrum. **b)** Propagation loss vs group index for the same waveguide.

The accuracy of the cutback measurement is limited by the assumption that the total power coupled into each device is constant. This assumption requires very straight and even facets along the sample, as well as a constant alignment of the input and output lenses to the access waveguides. Due to the small size of the access waveguides, around 220 nm in height, and the 50 nm alignment accuracy achievable with the equipment used, this alignment accuracy cannot be achieve consistently. However, the use of many sampling points, typically $5 - 15$ waveguides, each measured with a resolution better than 0.1 nm, allows for the use of statistical methods to determine the error in the measured propagation loss. The typical error achieved with this setup is on the order of $1 - 2$ dB/cm, assuming that some waveguides of a 1 mm length or longer are included.

Fabry-Perot Interference Measurement As stated in the previous section, the cutback measurement technique only gives the difference in propagation loss between the access waveguides and the photonic crystal waveguides. Therefore blank waveguides are added to the sample and their propagation loss is measured using the Fabry-Perot (FP) interference technique, which was first proposed by D. Hofstetter and R. I. Thornton in 1997 [53]. The implementation I used is the numerical realisation of this proposed analysis developed by M. Kotlyar et al. [54, 55]. In this technique, a high resolution transmission spectrum of the access waveguides is measured. The facets of the sample have a relatively high reflectivity (30%), due to the high refractive index difference between air and silicon. Therefore the light inside the sample experiences multiple reflections resulting in a FP cavity. The transmitted intensity through this cavity can be calculated using the following equation:

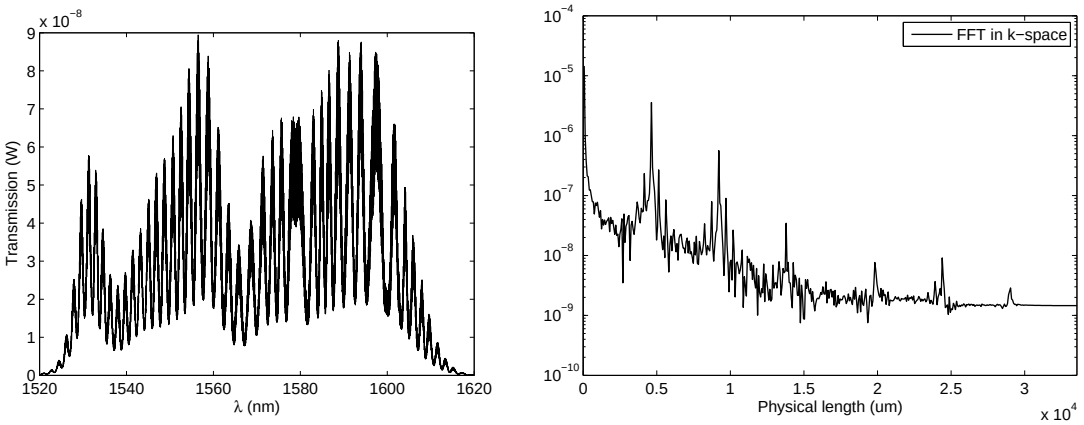

(a) (b)

Figure 26: **a)** Transmission spectrum of a photonic wire showing strong FP fringes due to the facet reflection. **b)** Graph showing the FT harmonics corresponding to round trips through the sample. In this case the waveguide was approximately $4.5\,mm$ long.

$$I(\beta) = \frac{(1-R)^2 \exp(-2kL\beta) + 4\sin^2(\phi)}{[1 - R * \exp(-2kL\beta)]^2 + 4R * \exp(-2kL\beta)\sin^2(\phi + nL\beta)} \tag{6}$$

where $\beta = \frac{2\pi}{\lambda}$ is the wave number and $\phi = \arctan(-2k/(n^2 + k^2 - 1)$ is the phase change of the light due to the reflection at the facets [53]. This FP cavity results in an oscillation superposed on the transmission through the waveguide, as shown in fig. 26. The Fourier transform of the FP oscillations gives all harmonics that contribute to the transmitted intensity. Each of these harmonics corresponds to a round trip of light within the samples, with the peak spacing equal to $2nL$ (see fig. 26). The difference in amplitude between peaks is linked to the amount of power lost during each round trip. The two mechanisms contributing to the power loss are the out coupling of light at each facet $(1 - R)$ and the power lost due to the propagation loss of the device (αL). From this, it can be shown that a fit to the peak height using the equation below gives the loss coefficient α:

$$y = P_0 + (\ln(R) - (\alpha L)) * x \tag{7}$$

where P_0 is the amplitude of the first peak and x is the peak number.

However, due to the small but finite dispersion of the silicon waveguides the above equation should only be fitted to fairly narrow wavelength sections, as explained in reference [55]. In my work 5 nm windows were generally used. A 5 nm waveguide window also ensures that the transformed data set has a high enough resolution, as seen in fig. 26 b). This proce-

dure is repeated to cover the complete transmission spectrum and the loss coefficients of all wavelength windows are then averaged to get the waveguide loss.

While M. Kotlyar used this technique to measure the propagation loss in photonic crystals, there are several issues that prohibit the use of this measurement for slow light photonic crystal waveguides in silicon. As shown in fig. 27, the FT harmonics for a PhC waveguide, here measured in the fast light region, look similar to those of the blank waveguide from fig. 26 b). This similarity implies that the propagation loss calculated using this method would be an average of the access waveguide and PhC loss, not the photonic crystal itself. Additionally, there are no clear fringes visible that correspond to the 200 μm device length and the inclusion of the photonic crystal facet leads to several new FP cavities formed on the sample, complicating the data analysis significantly. Even if clear peaks, corresponding to the PhC round trip length, were visible, the measurement would still not be suitable for slow light waveguides. As the group index in a slow light waveguide increases, the dispersion of the device increases and the propagation loss changes quickly over a narrow wavelength band. Therefore measuring the propagation loss of a 5 nm wavelength window would give the average loss over this wavelength range (ignoring GVD) and would lead to widening of the harmonic peaks in the presence of GVD. However reducing the wavelength window leads to a reduced spatial resolution, making it impossible to resolve the PhC round trip peaks (as is the case for fig. 27).

2.4.3 Slow light measurement

The last optical measurement, which needs to be performed in order to investigate propagation loss properly, is the measurement of the group index. There are several different approaches to this measurement, but generally they can be broken up into two basic types. In the first measurement type, an optical pulse is transmitted through the slow light sample and the time delay is measured [30, 56]. Since the device length can be measured, or is known from the device design, the group index can then be calculated from this delay. However, this is very cumbersome compared to other methods. The other basic principle is to measure the interference of light transmitted through the slow light sample with a reference signal [57, 58, 59, 60]. The interference pattern is dependent on the phase difference between the two signals, which in turn depends on the delay between the two signals. Several different interferometer geometries can be used for this measurement. The setup used during

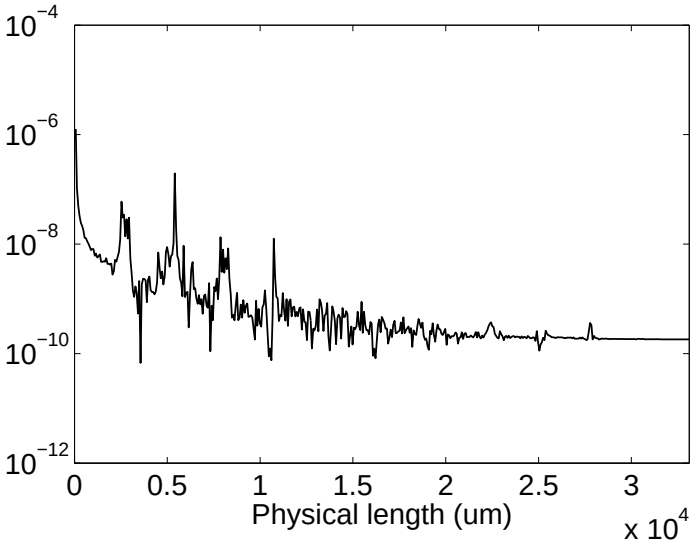

Figure 27: Graph showing the FT harmonics for a sample containing Photonic crystal waveguides. There are intermediate peaks present due to the formation of extra cavities formed between the PhC ends and the facets.

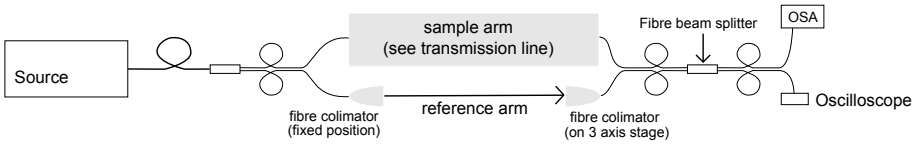

Figure 28: Sketch of the fibre based MZ interferometer used for slow light measurements. The sample arm consists of the same free space optics used for the transmission measurement (see fig. 21). One of the fibre collimators is mounted on a 3 axis stage for alignment purpose and to allow fine control over the reference arm length. Coarse control off the reference arm length is achieved by shifting the 3 axis stage with the fibre collimator.

this project was an external MZ interferometer [60], as shown in fig. 28 .

In this setup, the optical signal from the source, which can be both CW or pulsed, is separated into two using 3 dB fibre splitters. The sample is included in one arm (the sample arm) of the MZ interferometer, while an optical delay is included in the other arm (the reference arm). In our implementation, the optical delay is a section of free space transmission of variable length. The signals are recombined using a second 3 dB fibre splitter and the optical signal is then detected using an OSA.

Before taking a measurement, the delay in the reference arm is adjusted such that its optical length is just shorter than the sample arm in the fast light regime. Therefore, as the group index increases, the phase difference between the two signals increases, with the sign of the phase difference remaining constant, simplifying the calculation of the group velocity. In order to measure the group index of the chip several measurement are necessary. For each

device three spectra are measured, one for each arm of the MZ individually and one of the interference pattern (see fig. 29). These three spectra contain all the information necessary to work out the optical path difference between the two arms of the interferometer. However, this difference is made up of three components. Namely, the optical path difference due to the PhC slow light effect, the optical path difference due to the access waveguides (which have $n_g \sim 4$) and that due to the different physical length of the free space region in the two arms. In order to separate the first component from the other two, the measurement is also performed on a photonic wire on the same chip and the delay extracted from this measurement is subtracted from the total delay for the PhC measurement. The resultant optical path difference is due the photonic crystal waveguide.

With this technique, there are two main mechanisms that restrict the highest group index value that can be measured. As can be seen in fig. 29, the spacing of the interference fringes is reduced as the group index increases. This reduction in fringe spacing is due to an increase in the optical path difference between the two arms of the interferometer, leading to an associated increase in the phase difference. Therefore, at some point the fringe spacing has reduced such that Nyquist theorem is no longer satisfied, i.e. the resolution of the OSA is not sufficient to take at least two data points per cycle, leading to aliasing and random values for the group index. Consequently, higher n_g values can be measured in shorter photonic crystals, as an increase in n_g only leads to a small increase in optical length. It is very important to initially adjust the length of the reference arm to be only slightly shorter than the sample arm, increasing the fringe spacing in the interferogram and therefore allowing for a larger increase in optical path difference before being limited by the OSA resolution, when compared to a more unbalanced MZ interferometer.

The second mechanism restricting the measurement is the propagation loss, which has a more fundamental impact. First of all, propagation loss leads to a reduction of the transmitted power, which leads to a worsening signal to noise ratio as the propagation loss increases with group index. While a reduction in transmitted power is a limitation of the measurement, it could be resolved by increasing the input power or using more sensitive detection equipment. However, this compensation is not possible for the case of multiple scattering, where backscattered light is scattered again and therefore travels in the forward direction once more. This double-backscattered light can now interfere with the normal transmitted light, distorting the interference pattern of the MZ interferometer, leading to fluctuations

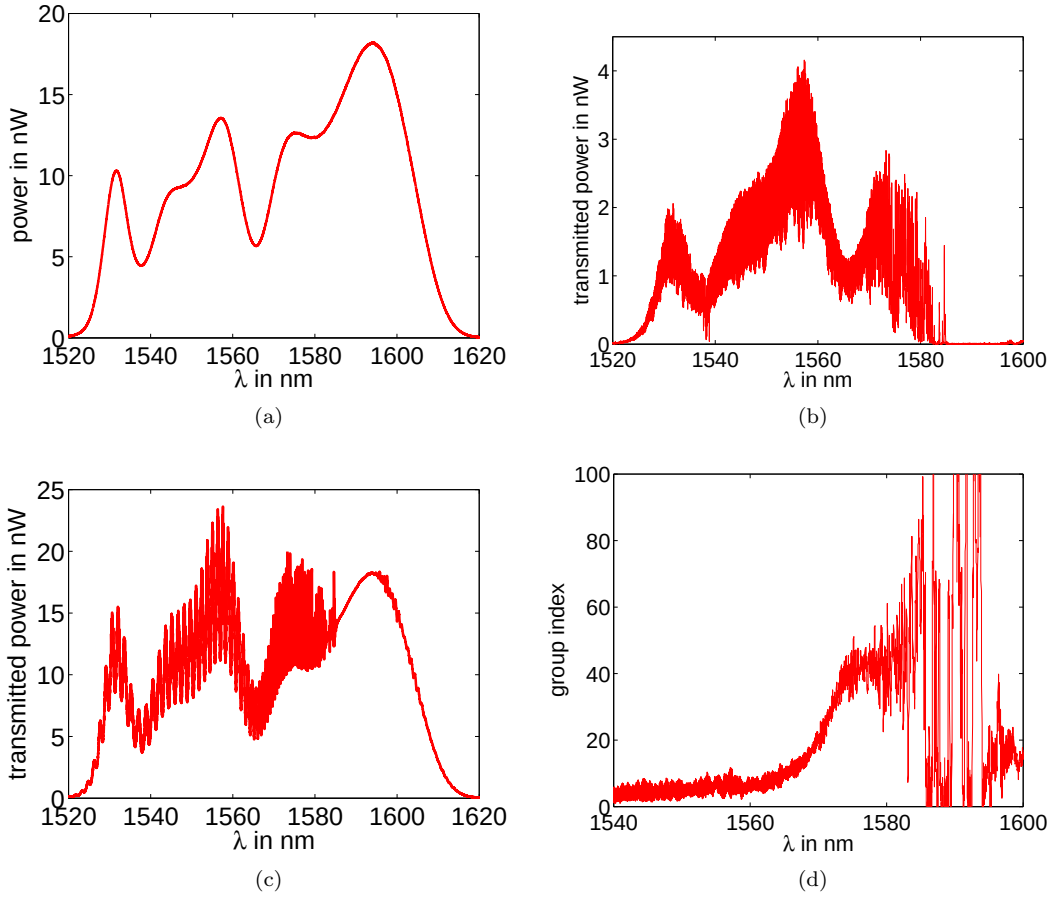

Figure 29: Graphs showing the data taken during a group index measurement. **a)** The signal from the reference arm. This correspond to the source spectrum, attenuated by coupling losses. **b)** The transmission spectrum of the sample (not normalised). One can see the cutoff at 1585 nm and strong oscillations in the signal due to multiple scattering between 1580 nm and 1585 nm. **c)** Interference pattern for the previous two graphs. One can see the wide fringe spacing in the fast light region ($1520 - 1560$ nm) being compressed as the group index increases (> 1560 nm). **d)** Resulting group index curve for this sample. Above 1580 nm the group index starts to fluctuate randomly due to the effect of multiple scattering on the phase, and amplitude, of the signal transmission. All measurements were taken with 0.02 nm resolution on a 186 μm long dispersion engineered PhC waveguide, with 10 period coupling regions on either end.

of the group index around its true value as shown in fig. 29. If the fluctuations become too large it is impossible to extract the true group index value, or, more precisely, the group index value of the waveguide cannot be defined anymore [61, 62], limiting not only the measurement, but the use of group index as a FOM. S. Mazoyer et al. [52] showed that, for 3 dB backscattered power, the transmission through a PhC is dominated by this interference effect. Once again, the use of short waveguides for a group index measurement reduces the effect of the backscattering loss, since a shorter device can reach a higher loss per unit length region, corresponding to a larger part of the slow light spectrum, before the total backscattered power reaches 3 dB.

3 Loss in photonic crystal waveguides

"Opportunity is missed by most people because it is dressed in overalls and looks like work"

Thomas A. Edison

In this chapter I will discuss propagation loss in photonic crystals. A history of important milestones in the fabrication of low loss waveguides, as well as the theoretical understanding of propagation loss follows. A perturbative approach is used to derive an equation, suitable for the calculation of propagation loss in photonic crystals, from first principles. Afterwards, a combined experimental and theoretical study will show that the previously assumed n_g^2 scaling is not universally correct. Through a closer examination of the roughness models used, and free parameters present in these models, the origin of this misconception will be revealed. Initial results on propagation loss in slotted photonic crystal waveguides will also be discussed. Finally, the calculation method developed during this project will be compared to other, especially non-perturbative, approaches for the calculation of propagation loss. The work presented in this chapter was performed in the framework of the EU-FP6 project SPLASH, in collaboration with the groups of Prof. A. Melloni, Prof. L. Kuipers, Prof P. Lalanne and Prof. R. De La Rue.

3.1 History of Propagation loss

3.1.1 Experimental measurements

An ideal (i.e. non disordered) photonic crystal has no optical loss mechanisms, other than coupling to the air mode continuum for k-vector components above the light line. Therefore, those modes that lie below the light line are intrinsically lossless, making these waveguides promising devices for nanophotonics.

The need for operation below the light line was demonstrated when C. Smith et al. [51] measured 100 dB/cm propagation loss for devices above the light line. In addition to the intrinsic leakage loss, this device also showed extrinsic scattering loss from fabrication disorder.

This initial measurement was followed by a rapid reduction in propagation loss, through the introduction of air-bridge structures and improved fabrication recipes [22, 37, 39, 63, 64]

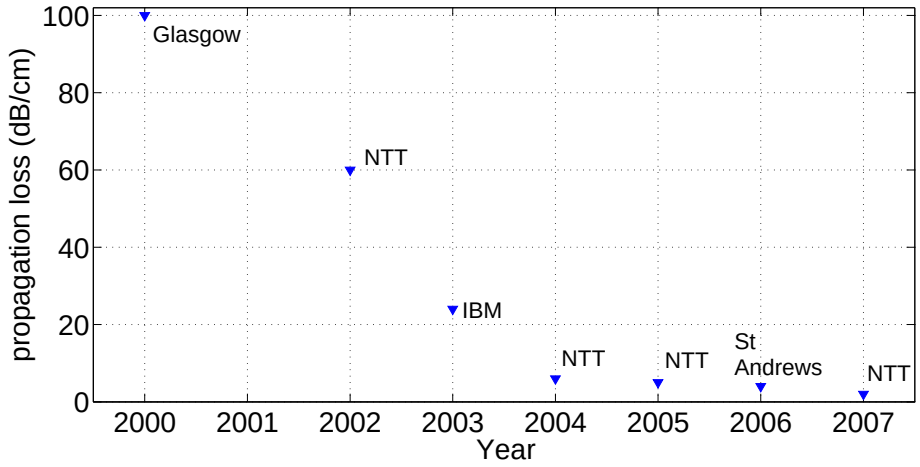

Figure 30: Graph showing record low propagation loss values in planar photonic crystal waveguides against the year that is was published [22, 37, 39, 51, 63, 64]. If more than one improvement was presented in one year, then only the lowest value is shown. The adjacent text indicates the University/company at which the experiment took place.

(see fig. 30). Air-bridge (or membrane) structures, where the underlying oxide is removed, have a larger bandwidth below the light line, and improved fabrication methods lead to reduced scattering losses. The reduced fabrication disorder was achieved through advances in electron beam lithography and improved etch recipes.

The advancement in reduction of propagation loss ended in 2007, when the group of Dr Notomi at NTT reported a loss of 2 dB/cm for a group index around 5 [22]. This value is very close to the best propagation loss achieved in silicon based photonic wires (1 dB/cm [65]). However, the lack of progress since 2007 begs the question why no further reduction of propagation loss has been achieved, and how the propagation loss can be reduced further. The answer to the first question lies in the size of the disorder present. Recent studies have shown that the disorder in low loss photonic crystal devices (~ 10 dB/cm) has a rms value of only $1 - 2$ nm [38]. To understand how such a small roughness can lead to this large propagation loss, we need to have a look at the theory underlying propagation loss.

3.1.2 Theoretical understanding

As already described in the last paragraph, an ideal photonic crystal is intrinsically lossless, if operated below the light line. For the purpose of nanophotonic applications, and my project, all waveguides are designed to operate below the light line. Therefore, all propagation loss is due to extrinsic scattering loss, caused by fabrication defects.

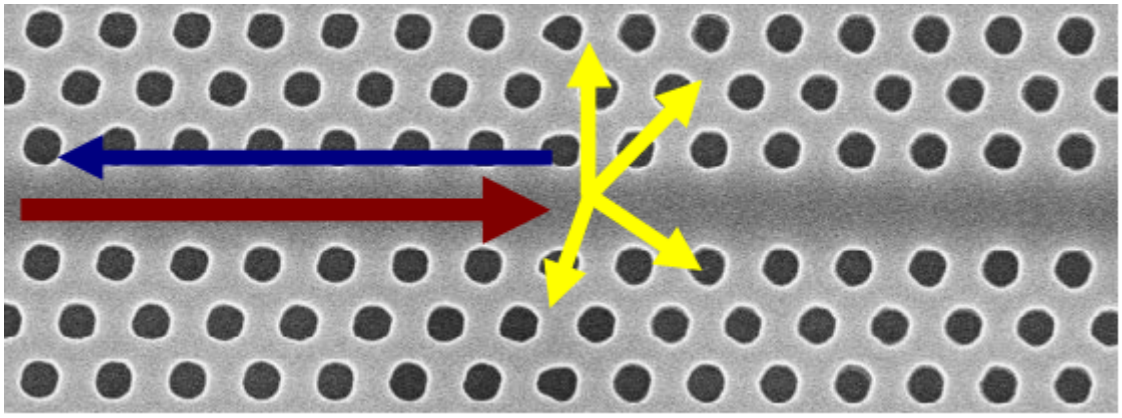

Figure 31: Sketch showing the two possible loss path. Incoming light (red) is scattered at a defect (here a stitching error). Light is either scattered out of the plane of the photonic crystal (yellow) or coupled back into the counter-propagating waveguide mode (blue).

Scattering in PhC waveguides can lead to several loss paths. First of all, light can be scattered out of the sample plane, and couple to modes in the cladding, or be scattered into the plane of the photonic crystal. The latter can be further broken down into light scattered into the forward propagating mode, the backward propagating mode, a different waveguide mode or into the photonic crystal side cladding. However, low loss photonic crystals are designed to be single mode, i.e. there is no overlap between the operating mode and a second, different order mode in the wavelength region of interest, eliminating inter-mode scattering as a source of propagation loss. Similarly, if the photonic crystal side cladding is sufficiently large, to avoid leakage through it, then scattering of light into the PhC cladding is negligible, as the PBG provides an efficient mechanism for suppression of this loss path. Light scattered into the forward propagating mode of the waveguide once again travels in the mode that it was scattered from and is not actually lost from the waveguide. We are now left with coupling into the backwards propagating mode (the backscatter loss), and out of plane scattering as the only components of propagation loss (see fig. 31).

A milestone in the understanding of propagation loss in PhC waveguides was reached in 2005, through the works of Hughes et al. [66] and Johnson et al. [67]. Both groups presented mathematical methods for the calculation of propagation loss in photonic crystal waveguides. According to these methods, backscattering loss scales as n_g^2 and out of plane loss scales as n_g. Additionally, later the same year Kuramochi et al. [37] used the method from reference [66] to calculate the propagation loss of fabricated PhC samples. In this work, they found that in the absence of inter-mode scattering (the region of interest to this

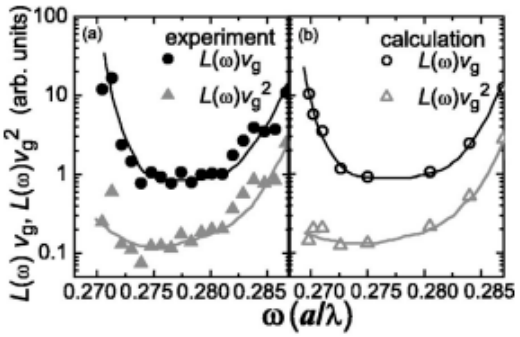

Figure 32: Graphs showing the product of propagation loss ($L(\omega)$) and group velocity (v_g) against frequency (ω) for the W1 waveguide measured by Kuramochi et al. [37]. **a)** shows experimental data, while **b)** shows theoretical data. The near constant behaviour of $L(\omega)v_g^2$ near the bandedge lead to the conclusion that backscattering is the dominant loss component in this region, and that slow light losses scale as n_g^2. Reprinted with permission from [37]. © 2005 by the American Physical Society

thesis), the propagation loss is explained by a combination of out-of-plane scattering and backscattering only. Kuramochi et al. further concluded that the n_g^2 scaling, and therefore backscattering, is dominant in the slow light regime (fig. 32).

If this scaling was universally true, then the future of slow light waveguides would be very bleak. With losses scaling as n_g^2 in the slow light regime, these devices would be of little use for most applications, as the transmission through devices would be too low. Any benefit achieved by operating in the slow light regime would be overshadowed by the increased device loss.

However, shortly after this n_g^2 scaling was observed, additional experiments showed conflicting results that were not in agreement with the previous conclusion. The first experiment was a loss measurement in deliberately disordered waveguides, showing a n_g^2 scaling in the slow light region, while losses in the fast light regime scaled as $n_g^{0.5}$ [38], a result that is consistent with neither the predicted scaling of out-of-plane nor backscatter losses [67, 68]. The second piece of conflicting evidence came from nonlinear experiments in dispersion engineered waveguides, where the nonlinear response was best explained by a linear scaling of propagation loss, for group indices as high as $n_g = 30$ [19]. Again this scaling is not consistent with the assumption that backscatter loss dominates in the slow light regime.

To summarise, at the beginning of my PhD work, propagation loss in photonic crystals was generally assumed to be due to a combination of out-of-plane and backscattering losses, with a n_g and n_g^2 scaling respectively. The losses in the slow light region were assumed to be dominated by the backscattering component, which would place major restrictions on the

use of slow light waveguides in applications. However, conflicting experimental results led to uncertainty in the field and warranted further studies of this topic.

3.2 Theory of propagation loss

One can use two approaches to calculate the propagation loss of PhC waveguides. The first is a full vectorial treatment of all disorder and the associated effects on the field distributions [52, 69, 70], while the second one is a perturbation theory approach. In our case, the perturbation theory approach is used, as it presents a much simpler approach (both computationally and intuitively). Furthermore, PhC based devices should be operated in the region where scattering is low [52] and perturbation theory is an adequate description of the system under these circumstances. S.Mazoyer et al. have recently shown that perturbation theory provides good descriptions of the average device properties, even if multiple scattering becomes an issue [52]. Please refer to the summary in section 3.4, at the end of this chapter, for a further discussion of the relative merits of different calculation methods.

Having decided on the approach used to calculate the propagation loss, the problem can be broken down further. In a perturbation theory approach, the assumption is that the presence of the scatterers has no influence on the electric and magnetic field distribution. Therefore, the calculation of propagation loss consists of a calculation of the electric field of an ideal structure, a disorder model and modeling of the interaction between the disorder and the electric field present in the structure.

The first point is fairly straight forward (by now). Any electric field can be written as a sum of components from an orthonormal basis, due to the superposition principle. Several groups have developed software programs, which, using such a basis, calculate the field distribution in a photonic crystal. The two most common implementations are based on a plane wave expansion method (PWE) [71] or on a guided mode expansion method (GME) [68, 72]. For all calculations in my project, I used the MIT photonics band package (MPB) [71], a free implementation of the PWE method.

While the calculation of the electric fields in the device is not a big issue anymore, the choice of disorder model is more controversial, with different groups favouring different models [66, 73, 74]. However, the effect of the disorder model on the calculation results is more easily understood once we have an expression for the interaction between disorder and the electric fields present. For now, it is sufficient to say that the disorder can be

characterised by a parameter $\Delta\epsilon(\mathbf{r})$. $\Delta\epsilon(\mathbf{r})$ gives the change in dielectric constant at position $\mathbf{r}$, due to a deviation fom the ideal structure. Furthermore, we neglect the roughness on the top and bottom surface of the slab, therefore $\Delta\epsilon(\mathbf{r})$ is only non-zero in the vicinity of the etched slab-hole material interfaces.

3.2.1 Scattering in Photonic crystals

A mathematically rigorous method for the calculation of the extrinsic scattering loss was presented by Hughes et al. [66] and is described in more detail by Patterson [75]. I will go through the derivation presented in [75], before introducing a more intuitive explanation, based on work by Johnson et al. [67] as well as Lecamp et al. [76]. This explanation allows for a better understanding of the physical processes involved.

For our rigorous derivation, we start with Maxwell's equations, assuming no free charges or currents:

$$\begin{aligned} \nabla.\mathbf{D} = 0 \qquad & \nabla.\mathbf{B} = 0 \\ \nabla \times \mathbf{E} = -\tfrac{\partial \mathbf{B}}{\partial t} \quad & \nabla \times \mathbf{H} = \tfrac{\partial \mathbf{D}}{\partial t} \end{aligned} \tag{8}$$

For ease of calculation, and since we are interested in the frequency response and not time response of our system, we now transform these equations to the frequency domain, such that:

$$\nabla \times \mathbf{E}(\mathbf{r},\omega) = i\omega\mathbf{B}(\mathbf{r},\omega) \qquad \nabla \times \mathbf{H}(\mathbf{r},\omega) = -i\omega\mathbf{D}(\mathbf{r},\omega) \tag{9}$$

where $\mathbf{D}(\mathbf{r},\omega) = \epsilon(\mathbf{r})\,\epsilon_0\mathbf{E}(\mathbf{r},\omega)$ and $\mathbf{B}(\mathbf{r},\omega) = \mu(\mathbf{r})\,\mu_0\mathbf{H}(\mathbf{r},\omega)$. Furthermore, we assume that all materials are non-magnetic ($\mu(r) = 1$ for all r) and transparent in the region of interest, resulting in the standard wave equation:

$$\frac{1}{\epsilon(r)}\nabla \times \nabla \times \mathbf{E}(\mathbf{r},\omega) = \left(\frac{\omega}{c}\right)^2 \mathbf{E}(\mathbf{r},\omega) \tag{10}$$

The wave equation is satisfied by a complete orthonormal set of solutions of the form $\sqrt{\epsilon(r)}\mathbf{E}(\mathbf{r},\omega)$, with:

$$\int_{unit\,cell} \mathbf{dr}\epsilon(\mathbf{r})\,\mathbf{E}_k^*(\mathbf{r},\omega).\mathbf{E}_{k'}(\mathbf{r},\omega) \quad = \quad \delta_{k,k'} \text{ and } \mathbf{E}_{-k}(\mathbf{r},\omega) = \mathbf{E}_k^*(\mathbf{r},\omega) \tag{11}$$

Here, I have chosen a slightly different normalisation than Hughes et al. [66, 69, 70, 75].

The normalisation I have chosen is consistent with that used by the MPB software package and avoids problems when extrapolating the propagation loss to long waveguides [70, 73, 75, 77]. In the presence of disorder within the system, the electric field can accurately be described by a Dyson equation of the form:

$$\mathbf{E}(\mathbf{r},\omega) = \mathbf{E}_0(\mathbf{r},\omega) + \int \overleftrightarrow{G}(\mathbf{r},\mathbf{r}',\omega) . \frac{\mathbf{P}(\mathbf{r}',\omega)}{\epsilon_0} \mathbf{dr}' \tag{12}$$

where $\mathbf{E}_0(\mathbf{r},\omega)$ is the initial field in the ideal structure, and the Green's function tensor $\overleftrightarrow{G}(\mathbf{r},\mathbf{r}',\omega)$ can be decomposed into a bound mode component $\overleftrightarrow{G_b}(\mathbf{r},\mathbf{r}',\omega)$ and a radiative component $\overleftrightarrow{G_r}(\mathbf{r},\mathbf{r}',\omega)$. $\mathbf{P}(\mathbf{r}',\omega)$ is the perturbation originating from the disorder. This equation, which is completely self-consistent and non perturbative, describes the change in the electric field due to scattering from the perturbation.

3.2.2 Born Approximation

Eqn. 12 can, in principle, provide an exact solution to the electromagnetic scattering problem. However, since the perturbation of the electric field in a PhC is best described as $\Delta\epsilon(\mathbf{r}) E(\mathbf{r},\omega)$, the equation cannot be solved accurately. Iteratively substituting in for $\mathbf{P}(\mathbf{r}',\omega)$ leads to an infinite series, which needs to be terminated for a calculation of real device properties. We will make the first order Born approximation, i.e. we will iteratively substitute the equation into itself, only keeping those terms that are first order, or lower, with respect to the Green's function. This approximation gives us:

$$\mathbf{E}(\mathbf{r},\omega) = \mathbf{E_0}(\mathbf{r},\omega) + \int \mathbf{dr}' \Delta\epsilon(\mathbf{r}') \overleftrightarrow{G_b}(\mathbf{r},\mathbf{r}',\omega) . \mathbf{E_0}(\mathbf{r},\omega) + \int \mathbf{dr}' \Delta\epsilon(\mathbf{r}') \overleftrightarrow{G_r}(\mathbf{r},\mathbf{r}',\omega) . \mathbf{E_0}(\mathbf{r},\omega) \tag{13}$$

where the first integral gives backscattering into the backwards propagating mode, the second integral term describes the out of plane scattering, and all other possible scattering mechanisms described earlier are neglected, as they would be second order with respect to the Green's function. This result is consistent with our intuitive argument, in that out-of-plane and backscattering are the only loss mechanisms present. Therefore the first order Born approximation should be sufficient to describe the propagation of light through a PhC waveguide.

So far, we have made two assumptions. The first assumption is that the perturbation

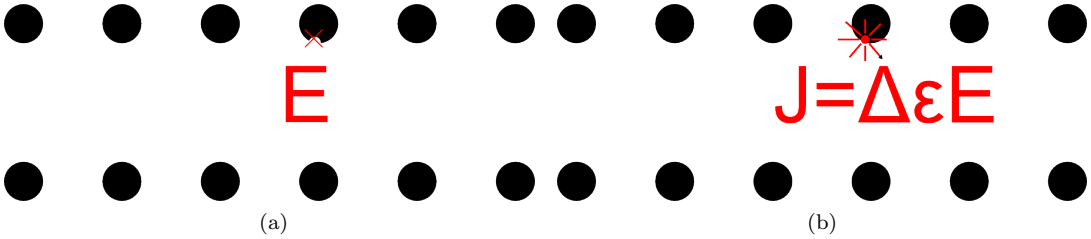

Figure 33: The effect of a scatterer ($\Delta\epsilon(\mathbf{r})$) within an incident electric field $\mathbf{E}(\mathbf{r},\omega)$ (**a**), is equal to a current $\Delta\epsilon(\mathbf{r})\,\mathbf{E}(\mathbf{r},\omega)$ being emitted by a dipole source at the same position (**b**).

can be expressed as:

$$\mathbf{P}(\mathbf{r},\omega) = \Delta\epsilon(\mathbf{r})\,\mathbf{E}(\mathbf{r},\omega) \tag{14}$$

Effectively we replace the disorder, which acts as a scattering location, by a dipole source with emission $\Delta\epsilon(\mathbf{r})\,\mathbf{E}(\mathbf{r},\omega)$, as shown in fig. 33. This approach is widely used [37, 66, 67, 73, 76] and it has been shown that the effect on the field distribution is identical to that of the original scatterer [76].

In our second approximation, we neglect all those terms of second order, or higher, with respect to the Green's function. Physically each appearance of the Green's function represents a scattering event. Therefore, first order terms with respect to $\overleftrightarrow{G}$ include backscattering, out of plane scattering and scattering into the PhC cladding. The latter can be excluded because of the bandgap. Any higher order term corresponds to a multiple scattering event, such as scattering from the air mode continuum into a waveguide mode or scattering of light that has already undergone a backscattering event. However, coupling from the air mode continuum back into the waveguide is negligible in realistic structures, as the out-of-plane scattered light propagates away from the waveguide over a very short distance, and the exclusion of multiple backscattering does not, on average, affect the calculated properties of the device, as described towards the end of this chapter (section 3.4).

3.2.3 Backscattering

In order to proceed further, we treat backscattering and out of plane scattering independently. For our calculation of the backscattered light (see fig. 34), we need an expression for the bound mode Green function in eqn 13. Here I take the same expression as used in [75]:

$$\overleftrightarrow{G}_b(\mathbf{r},\mathbf{r}',\omega) = i\frac{a\omega}{2v_g}\left[\mathbf{E}_k(\mathbf{r},\omega)\otimes\mathbf{E}_k^*(\mathbf{r}',\omega)\,\mathbb{H}(x-x') + \mathbf{E}_k(\mathbf{r}',\omega)\otimes\mathbf{E}_k^*(\mathbf{r},\omega)\,\mathbb{H}(x'-x)\right] \tag{15}$$

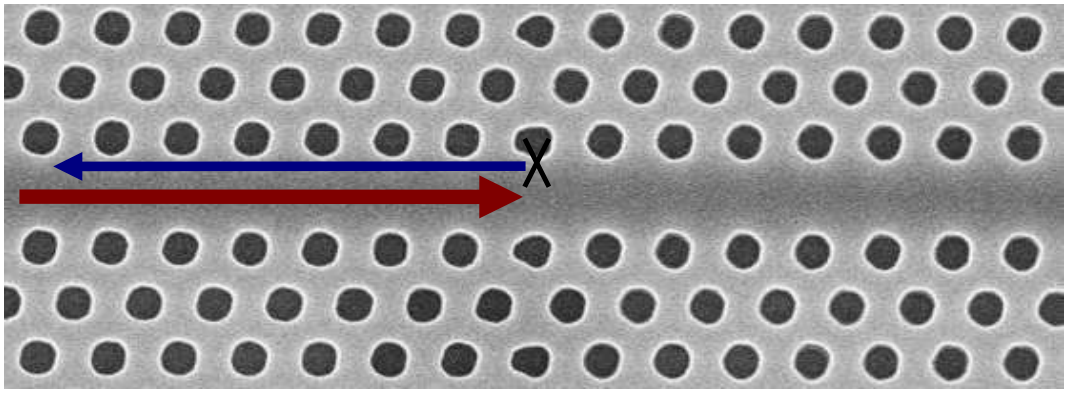

Figure 34: Sketch illustrating backscattering (blue) of the forward propagating mode (red), from a defect (black cross). Here the defect is a stitching error.

where x is the component of $\mathbf{r}$ along the waveguide, and $\mathbb{H}$ is the Heaviside step function. We find the reflected amplitude by considering the case where $x = 0$, i.e. the beginning of our calculation domain. In this case, the electric field consists of the incident and single backscattered field, such that $\mathbf{E}(x = 0, \omega) = \mathbf{E}_0(\mathbf{r}, \omega) + r\mathbf{E}^*(\mathbf{r}, \omega)$, where r is the reflection coefficient. To find r, we multiply both sides of the equation by $\epsilon(\mathbf{r})\mathbf{E}(\mathbf{r}, \omega)$ and substitute in eqn 15, yielding:

$$r = i\frac{a\omega}{2v_g}\int_{cell} \mathbf{dr}\Delta\epsilon(\mathbf{r})\mathbf{E}(\mathbf{r}, \omega).\mathbf{E}(\mathbf{r}, \omega) \tag{16}$$

Based on this result, we can now extract the power reflection coefficient, using the well known formula:

$$\begin{aligned} \alpha_{back} &= R = r.r^* \\ \alpha_{back} &= \frac{(a\omega)^2}{4v_g^2}\left|\int_{unit\,cell} \mathbf{dr}\Delta\epsilon(\mathbf{r})\mathbf{E}(\mathbf{r}, \omega).\mathbf{E}(\mathbf{r}, \omega)\right|^2 \end{aligned} \tag{17}$$

If we examine eqn 17 closely we get a better understanding of the Physics involved in the scattering processes.

The first term we see is the set of constants in front of the integral. Here, several terms such as the lattice constant a and the frequency ω are self explanatory. The inverse group velocity term is present, as backscattering is dependent on the density of states in both the incident and backscattered mode [66], and the density of states is proportional to $n_g = \frac{1}{v_g}$. This term was generally seen as being the dominant term and, together with the disorder model chosen, led to the prediction that all backscattering loss would scale as n_g^2.

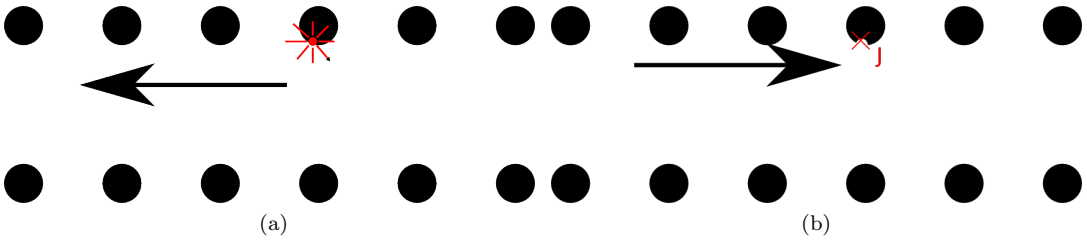

Figure 35: The mode exited by a dipole source (**a**) (in this case the backwards propagating mode $\mathbf{E}^*(\mathbf{r},\omega)$) is equivalent to the scalar product of the source emission, $\mathbf{J} = \Delta\epsilon(\mathbf{r})\,\mathbf{E}(\mathbf{r},\omega)$, with the reciprocal waveguide mode (**b**) (in this case $\mathbf{E}(\mathbf{r},\omega)$)

However, the integral in eqn 17 is actually the dominant and most important term. The following paragraph provides a more intuitive explanation of the processes involved. As described at the end of the last section, $\Delta\epsilon(\mathbf{r})\,\mathbf{E}(\mathbf{r},\omega)$ represents a dipole source, with an emission that is equivalent to the field scattered by the defect at $\mathbf{r}$. However, the total backscattered power is not only dependent on the amount of light scattered at the defect (i.e. emitted from our virtual source), but also on the coupling of scattered light into the backwards propagating mode. This coupling efficiency is proportional to the dot product of the scattered fields with the complex conjugate of the final mode profile [76], as shown in fig. 35. In this case, we are interested in coupling into the backwards propagation mode, given by $\mathbf{E}^*(\mathbf{r},\omega)$, and therefore our coupling is described by $\mathbf{E}(\mathbf{r},\omega).\mathbf{E}(\mathbf{r},\omega)$.

3.2.4 Disorder model

The last unknown in eqn 17 is the disorder model, $\Delta\epsilon(\mathbf{r})$. As shown earlier (fig. 16), several types of disorder can be present in a photonic crystal. In the past, different groups have chosen different disorder models for their calculations, see fig. 36.

Here, we will not implement a specific disorder model, corresponding to only one of the many types of disorder present in a photonic crystal. Instead, we will use the average properties of the fabrication disorder. In our calculation, the final result corresponds to the ensemble average of the propagation loss, instead of producing the loss for a single disorder realisation. Therefore, we only need to be concerned with $\langle\Delta\epsilon(\mathbf{r})\rangle$. We further stipulate that $\langle\Delta\epsilon(\mathbf{r})\rangle$ is zero everywhere except on the etched sidewalls, and we assume that $\langle\Delta\epsilon(\mathbf{r})\rangle$ is completely characterised by the difference in dielectric constant between the slab and hole materials ($|\Delta\epsilon| = \epsilon_s - \epsilon_h$), the rms size σ and the coherence length l_c. Both assumptions are reasonable upon closer inspection of other disorder models. Generally, the

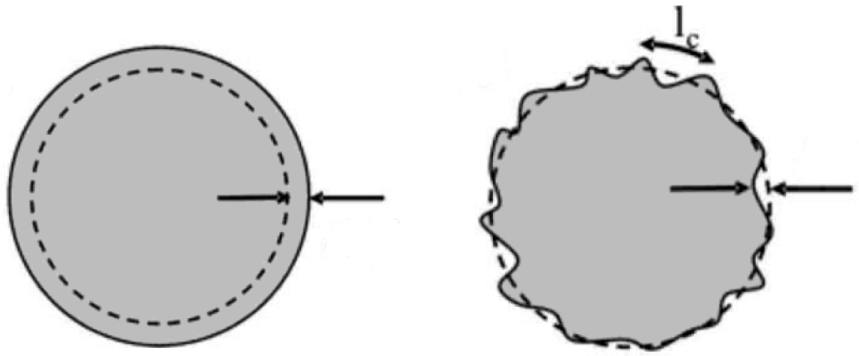

Figure 36: Sketches showing different disorder models, as used in previous publications [37, 52, 62, 66, 69, 70, 73, 77, 78] **a)** Radius disorder, with a single hole coherence length. **b)** Hole shape disorder, typical values used for the coherence length in this situation are $\sim 40\,\mathrm{nm}$. Reprinted with permission from [73]. © 2008 by the American Physical Society

top and bottom surfaces of the Si slab are polished during wafer fabrication, leading to very smooth surfaces. Therefore, these surfaces have negligible roughness compared to the disorder introduced during device fabrication. The second assumption is reasonable, since all possible disorder models have several points in common. As all roughness on the top and bottom surfaces of the dielectric slab is ignored, disorder can only be present on the surfaces of the photonic crystal holes.

Secondly, the disorder is modeled to have a given rms value σ and a correlation/coherence length l_c. Here, the correlation length is defined as the distance over which the disorder is influenced by neighbouring defects. The roughness correlation is important for backscattering, as roughness of the same sign leads to the same phase shift upon reflection. Light scattered from different positions within the PhC will interfere. If two disordered points are correlated, then the phase difference between light scattered from these points is always constant, leading to a constant interference pattern. However, if the two scatterers are further apart, and therefore uncorrelated, the phase difference between scattered light is random and therefore no clear interference pattern exists. These components of the backscattered light are added incoherently, i.e we neglect the phase of the fields present.

3.2.5 Modified Backscatter Calculation

We will make one additional modification to eqn 17, in order to achieve an efficient calculation of the propagation loss. We choose to express $\mathbf{E}(\mathbf{r},\omega)$ in terms of two orthogonal components, here $\mathbf{E_T}(\mathbf{r},\omega)$ and $\frac{1}{\epsilon}\mathbf{D_N}(\mathbf{r},\omega)$, where ϵ is the dielectric constant at position

$\mathbf{r}$, and $\mathbf{E_T}$ and $\mathbf{D_N}$ are the tangential and normal component of the electric field and displacement respectively. These components have been chosen, as they are continuous across a dielectric material interface, allowing for a simpler integration (and interpolation) across those interfaces.

Using our simplified disorder model and new expression for $\mathbf{E}(\mathbf{r},\omega)$, we can rewrite eqn 17:

$$\begin{aligned} \alpha_{back} &= c_2 n_g^2 \rho \\ \rho &= \sum \left| \int_{l_c} \mathbf{E_T}.\mathbf{E_T} + \frac{1}{\epsilon_1 \epsilon_2} \mathbf{D_N}.\mathbf{D_N} d\mathbf{r} \right|^2 \end{aligned} \tag{18}$$

where the summation is over all elements of length l_c that are present in a single unit cell. α_{back} represents the ensemble averaged backscattering, while the dependence of backscattering loss on the density of states is now included explicitly through the n_g^2 term. All other constants across the system have been included in c_2. Although $c_2 = k_2 \frac{(\Delta\epsilon)^2}{a} \left(\frac{\sigma}{\lambda}\right)^2$ depends on many parameters, such as the lattice constant, operating wavelength and materials chosen, it can be treated as a constant for most calculations. Since most groups tend to work in a given material system (constant $\Delta\epsilon$), a given wavelength regime (in our case around 1560 nm) and therefore use only a narrow range of lattice constants, c_2 only varies very little between different device designs. On the other hand, the rms value of the disorder cannot be measured directly and is generally used as a fitting parameter, before being kept constant across multiple calculations. Therefore, the error introduced by keeping c_2 constant is small compared to the variation in fabrication quality between two samples fabricated using the same recipe.

3.2.6 Out of plane scattering

Propagation loss is not only caused by backscattering, but also includes scattering into the air mode continuum (see fig. 37). This scattering process, involving a continuum of modes, is much harder to model directly and no analytical formula such as eqn 17 exist. In many cases, the effect of out of plane scattering is modeled through finite difference time domain calculations [37, 66] or by replacing the photonic crystal slab with a uniform dielectric slab, of suitable refractive index, and then calculating the Green's function for the scattering due to a defect on the top surface of this slab [72, 75]. While this Green's function can be

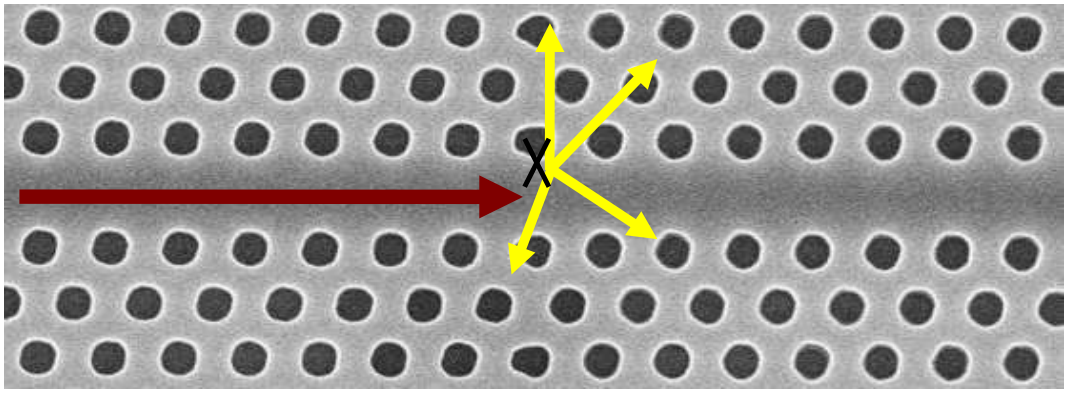

Figure 37: Sketch illustrating scattering into the air mode continuum (yellow) of the forward propagating waveguide mode (red), from a defect (black cross). Here the defect is a stitching error.

derived analytically, the resulting equation for the out of plane scattering can only be sloved numerically [75]. Here, I propose a simpler and more intuitive approach. The model again treats a scatterer as a dipole source and it is assumed that only a proportion of the scattered light can couple to the air-mode continuum. This proportion is taken to be independent of the scattering location in the photonic crystal slab and to be constant for different devices. As a consequence, we can now write the out of plane scattering component as:

$$\begin{aligned} \alpha_{out} &= c_1 n_g \gamma \\ \gamma &= \sum \left| \int_{l_c} \mathbf{E_T} + \frac{1}{\epsilon} \mathbf{D_N} d\mathbf{r} \right|^2 \end{aligned} \tag{19}$$

where γ describes the radiation of a free dipole source. The dependence of out of plane scattering on the density of states of the incident waveguide mode, included implicitly in previous calculation methods [67, 68], is again included explicitly through the n_g term. The proportion of the light that is coupled into the air mode continuum is absorbed as a factor into $c_1 = k_1 \frac{(\Delta\epsilon)^2}{a} \left(\frac{\sigma}{\lambda}\right)^2$. In this pair of equations (18 and 19), one of the reasons for including the group index dependence explicitly is that this model is designed for calculations using the MPB software package, where the fields are normalised independently for every value of the wavevector, k. Therefore the density of states is not included implicitly in this implementation. Similarly, the fields in MPB are unitless and therefore the constants $c_1$and c_2 include unit conversion factors, such that the resulting value for the propagation loss is in dB/cm.

3.3 Loss calculation and the effect of coherence length

We can now combine equations 18 & 19, yielding the final result of our derivation, i.e. the equation for the total propagation loss of a PhC waveguide given in dB/cm:

$$\alpha = c_1 n_g \gamma + c_2 n_g^2 \rho \tag{20}$$

where all variables have been described above.

From equations 18, 19 and 20, we can see that we have three unknowns. These unknowns are l_c, c_1 and c_2. c_1 and c_2 will be used as fabrication parameters; i.e. they will be determined experimentally, by fitting the calculated loss curve to measured data. Afterwards, when modeling new waveguide designs for fabrication using the same process (same E-beam system, RIE etc.), and for the same wavelength region/lattice constant, they will be kept constant.

The coherence length, which determines the limits of integration in eqns 18 & 19 and therefore the distance over which the phase of the scattered light is included in the calculation, is dependent on the disorder model used. Although different research groups have previously chosen disorder models with different coherence length values [66, 73, 74], the effect of changing the coherence length has never been studied sufficiently. W. Song et al. have previously investigated the effect of changing the coherence length, but only over a very narrow range, from 0 nm to 50 nm, and for W1 waveguides only [79].

3.3.1 Propagation loss for varying coherence length

To study this effect properly, several different photonic crystal waveguide designs were fabricated on the same chip and propagation loss was determined using the cutback measurement technique (see section 2.4.2). The theoretical propagation loss for all designs was calculated, using several different values for the coherence length. The resulting curves are fitted to the experimental data, to determine the values of c_1 and c_2, with the condition that these values have to be the same for all designs. In order to avoid the effect of stitching errors, the waveguides were fabricated in conjunction with the University of Glasgow, using a VISTEC VB6 E-beam system with 100 kV accelerating voltage and 1200 μm writefield. For the cutback measurement waveguides of 100 μm, 300 μm, 700 μm, 900 μm, 1500 μm and 2000 μm length were fabricated. The designs used included several dispersion engineered waveguides

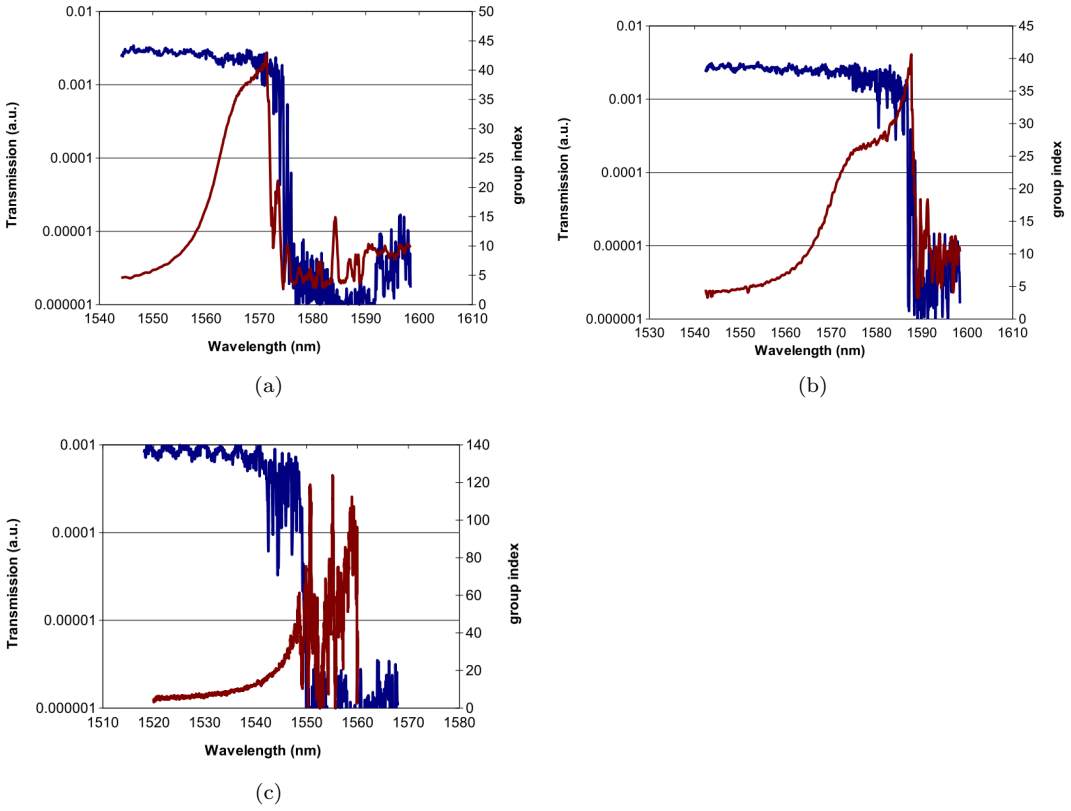

Figure 38: Sample transmission (blue) and group index (red) curves for dispersion engineered waveguides, **a)** and **b),** and a W1 waveguide, **c)**. The dispersion engineered waveguides were designed to have a low dispersion region around $n_g = 37$ (**a**) and $n_g = 27$ (**b**) respectively. The position of the transmission cutoff, after the flat band slow light region, indicates that the propagation loss should remain relatively low over the slow light region.

and a standard W1 waveguide. Some sample group index curves and transmission spectra are shown in fig. 38.

For the coherence length, four values, 1 nm, 40 nm, a single hole circumference and the complete unit cell, were used. The first value represents a point scatterer (i.e. every disordered point is independent of the next), the second (40 nm) was the value used by S. Hughes *et al.* [66]. This value was chosen by S. Hughes *et al.*, as it is identical to the coherence length of roughness on the sidewall of a photonic rib waveguide, as measured by atomic force microscopy. It gave a reasonable fit to the propagation loss of a W1 waveguide [37]. The third value represents the coherence length chosen by B. Wang *et al.* [73] and is most easily understood by imagining a change in hole radius, where all points on the hole sidewall are shifted either outwards or inwards. The fourth value would indicate that the scattering from different holes adds coherently and was included to have a more complete set of values, including both extremes of the range that the coherence length can take. In fig. 39 we can

see the effect of changing the coherence length on the calculated results, both for a W1 and for one of the dispersion engineered waveguides. The effect is the same for other dispersion engineered waveguides and therefore not shown here. We can observe that, for the W1 waveguide, several values for the coherence length give a reasonable fit. Furthermore, all values can give a good fit, as long as c_1 and c_2 are adjusted accordingly. This result goes a long way to explaining the confusion that arose over which disorder model (which in essence means coherence length) should be used for the propagation loss calculations. Additionally, it is easy to come to the conclusion that propagation loss scales as n_g^2, since we can see that the loss curve for the W1 (both calculated and measured) resembles a parabola.

However, for the dispersion engineered waveguides the situation is very different. First of all, we observe a significantly different dependence of propagation loss on group index. For the engineered waveguides, the loss curve initially scales linearly with group index before suddenly increasing rapidly (more details and an explanation of this are given in section 4.1). The point scatterer model can accurately simulate the linear loss region, but does not predict the rapid increase in propagation loss. The 40 nm coherence length model again gives a good fit to the linear loss region and predicts a rapid, but small, increase of the propagation loss at the correct group index value. This increase is far smaller than the experimentally observed change.

In contrast, both the single hole and complete unit cell coherence length models give a very nice fit to the measured data. They both accurately predict the linear dependence for low group index values and a rapid increase of the propagation loss, at the correct group index value. However, we can see that the unit cell model has a small dip in the propagation loss, just before the rapid increase that is not observed experimentally. Therefore, we conclude that a single hole coherence length gives the best agreement between measured and calculated propagation loss.

3.4 Conclusions

In reality this result poses more questions than it answers, such as:

- Why does propagation loss scale linearly with group index initially, before increasing rapidly?
- Why does the propagation loss increase rapidly at a given group index value, and what determines this group index value?

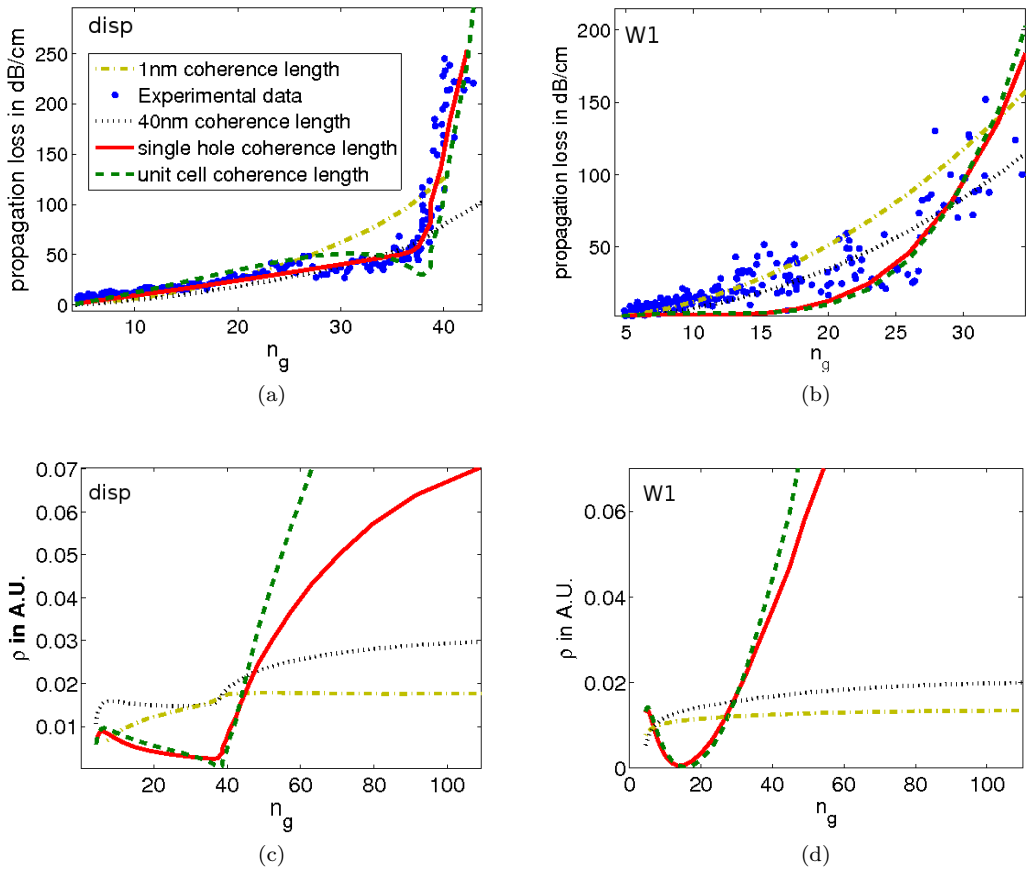

Figure 39: Graph showing measured propagation loss and ρ for a dispersion engineered, **a)** and **c)**, and a W1 waveguide **b)** and **d)**. Different colours correspond to different values of the coherence length. Blue circles represent the measured propagation loss, 1 nm coherence length is shown in yellow (dot-dashed line), 40 nm in black (dotted line), single hole coherence length in red (solid line) and the unit cell coherence length in green (dashed line). The assumption of a n_g^2 scaling of propagation loss arose from the parabola like shape of the 40 nm coherence length results for the W1 waveguide, however both the n_g^2 scaling and the 40 nm coherence length cannot explain the observed propagation loss for the dispersion engineered waveguides.

- Do all dispersion engineered waveguides have a similar loss behaviour?
- Can this linear dependence be extended to higher group index values?
- Can we calculate the propagation loss of other PhC based waveguides?

These questions will be discussed in the next chapter and, before proceeding to address them, a quick summary of the results so far is in order.

By using a variety of different waveguide designs and comparing the measured propagation loss of these devices, we have shown that a n_g^2 scaling of the propagation loss is not universal. Instead, some devices show an initial linear dependence on the group index, which is very promising for nonlinear applications, for example third harmonic generation (THG) [7, 20], where the nonlinear efficiency can now increase faster with group index than the propagation loss. Additionally, we have shown that only a single hole coherence length gives an accurate fit of the propagation loss to a wide range of waveguide designs. The ensemble average of the propagation loss can be calculated in the same step as the band-structure, using an ideal (i.e non-disordered) design, by making some minor adjustments to the equations involved. This calculation is efficient (a full 3D simulation on a desktop PC takes 3-4 hours) and the code required is available for free under the GPL license [80, 81].

Multiple scattering The model discussed here is based on a standard perturbation theory approach, and therefore should only be valid for the region where the scattered fields are small. However, if we consider the effect of multiple scattering, we can see that the range of our model can be extended, as long as we are only interested in the average properties of a design and not the exact properties of a single device. Several groups have shown, using fully vectorial methods, which are non-perturbative and include the effect of the scattered phase over the complete device length, that multiple scattering leads to a strong variation of the back-reflected and transmitted power over very narrow wavelength steps (see fig. 40) [52, 69, 70, 78], most notably when the sample length corresponds to the mean free path length. For this case, where the average backscattered power is 3 dB, S. Mazoyer *et al.* have shown, both theoretically [52] and experimentally [78], that the actual transmission ranges from 0 to 1 (normalized to the incident power). However, for these designs, our perturbative model still accurately predicts the average propagation loss and backscattering (i.e. 3 dB). Therefore, we can conclude that, as long as eqn 5 is used as our base definition of the propagation loss, the perturbative model presented here can be

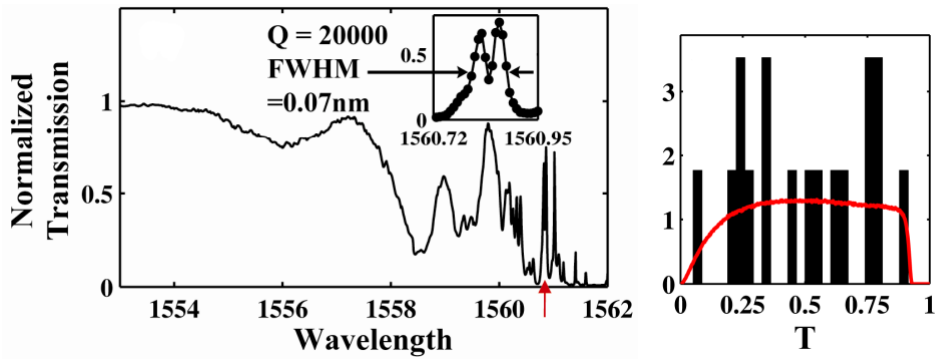

(a) (b)

Figure 40: a) Simulated transmission spectrum for a W1 waveguide. Multiple scattering leads to a strong variation in the transmission near the cut-off. The inset shows the formation of cavities due to random disorder. b) Histogram of actual transmission (black bars) for devices with $\langle T \rangle = 0.5$. The red line indicates the calculated probability density distribution. Figures taken from reference [78]

used to predict average device properties and behaviour. Indeed, it is better suited for the calculation of the average device properties, as a single calculation is sufficient, while the results of multiple calculations would need to be averaged, when using one of the coherent scattering methods mentioned above. This finding is also supported by Mazoyer *et al.* [52]. An intuitive description of the effect of multiple scattering supports these findings. Let us imagine the case of twice backscattered light. This light is now traveling in the same direction as the original wave, however it has picked up a phase shift compared to the incident beam at the same location. This phase shift is due to possible phase shifts upon scattering and due to the extra optical path traveled. Therefore, the two waves will interfere, with the phase shift determining if this leads to an increased or decreased optical intensity. On average, both results are equally likely and therefore the multiple scattering leads to fluctuations in the transmission curve, but the average transmission, and therefore propagation loss, is not affected, as shown in fig. 40 b). In the case of very high backscattering this interference can lead to the formation of disorder induced cavities, as shown in fig. 40 a), since the strength of scattering from each defect and the phase shift obtained over several scattering events are highly wavelength (and wavevector) dependent.

4 Loss engineering

"The important thing in science is not so much to obtain new facts, as to discover new ways of thinking about them"

William L. Bragg

As an analogue to the term "dispersion engineering", which describes the process of designing slow light waveguides with a low group velocity dispersion (see section 2.1.4), "loss engineering" describes waveguides designed to have a propagation loss curve that is different, and ideally lower, than that of a W1 waveguide. The possibility of this process was only discovered through the experiment described in section 3.3, where we showed that different photonic crystal waveguides have a significant variation in the dependence of propagation loss on group index. The processes involved in loss engineering are the same as described in section 2.1.4.

This chapter builds on the work of the previous one, where a new code for the calculation of propagation loss in photonic crystals was presented and the effect of the correlation length was clarified. Initially, I will give a more detailed discussion of the propagation loss in some of the devices discussed before. Specifically, I will address the relative importance of out-of-plane and backscattering losses, as well as the relative strength of the scattering originating from different rows.

Next, the question of which variable propagation loss fundamentally depends on will be clarified. In section 4.3, the knowledge gained in sections 4.1 & 4.2 will be combined to yield some design rules for low loss photonic crystal waveguides. The last sections of this chapter will discuss the advantages originating from loss engineered photonic crystal waveguides and present an extension of the calculation method to slotted photonic crystal waveguides.

4.1 Propagation loss in engineered photonic crystal waveguides.

A short examination of fig. 41 shows clearly that the propagation loss in dispersion engineered waveguides does not follow the n_g^2 scaling expected from the work of S. Hughes *et al.* [37, 66]. Additionally, it shows that the new loss calculation procedure outlined in section 3.3 reproduces the experimental results. At this point, we should remind ourselves of

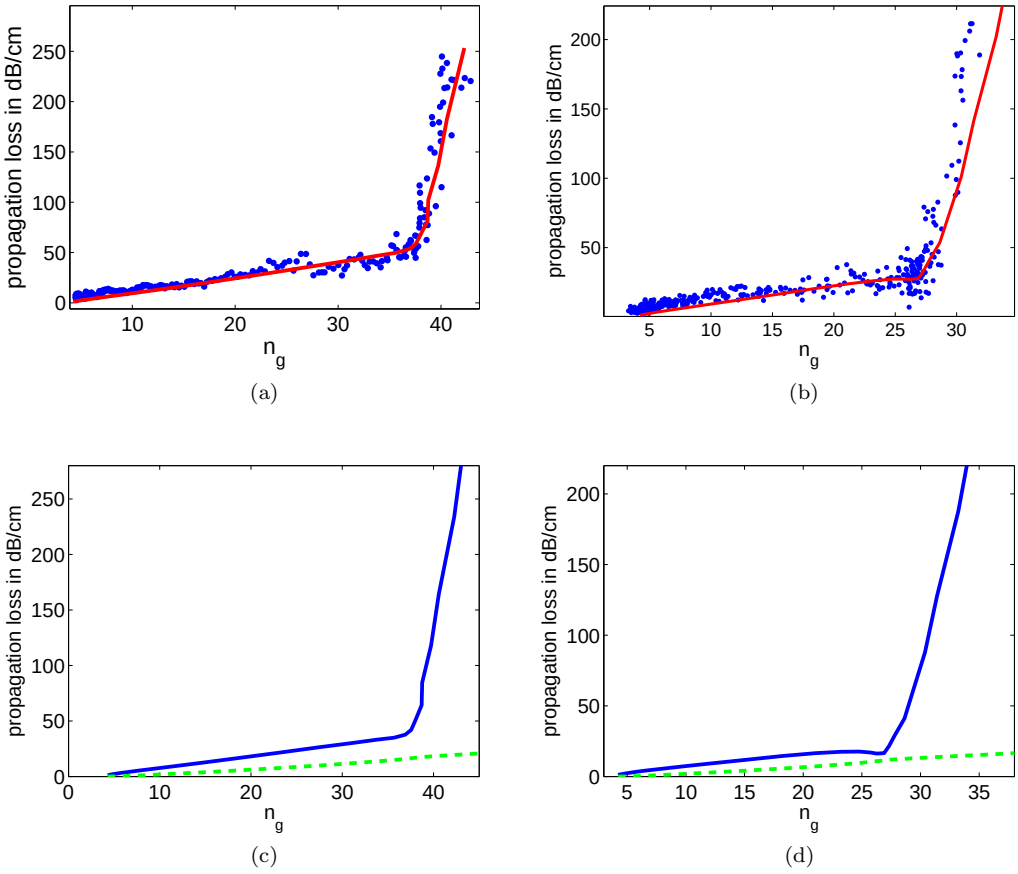

Figure 41: Experimental (blue) and theoretical (red) propagation loss of two engineered waveguides, plotted against group index. The waveguides were designed to have a low dispersion region around $n_g = 37$ **(a)** and $n_g = 27$ **(b)**. The same fabrication parameters were used for both calculations. **c)** and **d)** show the components of propagation loss due to out-of-plane (dashed green line green) and backscattering (solid blue line). In the fast light region, both provide a significant contribution to the total propagation loss, while the rapid increase in propagation loss is cause by a rapid increase in the backscattering component. The waveguides are the same as in fig. 38

equation 20, used to calculate the theoretical loss values:

$$\alpha = c_1 n_g \gamma + c_2 n_g^2 \rho$$

where α is the propagation loss in dB/cm, n_g is the group index, c_1 and c_2 are fabrication parameters and γ and ρ are the out-of-plane and back scatter coefficients respectively. Since both components of the propagation loss have a different dependence on the group index, an evaluation of the relative strength of these components is necessary, in order to develop rules for the design of low loss waveguides. Such a comparison is shown in fig. 41, where both components are plotted separately. We can see that initially both components have comparable contributions to the total propagation loss, while the rapid increase in propagation loss at $n_g = 37$ (27 respectively) is caused by a rapid increase in the backscattered light. The out-of-plane component does not change significantly at this point. Therefore, the complicated group index dependence of the propagation loss that we observe is due to a similar dependence of the backscattered loss, while the dependence of out-of-pane scattering is very similar to the simple, linear n_g dependence expected from literature [67, 68, 72]. Additionally, as shown in fig. 42, the reduced propagation loss of engineered waveguides, compared to a W1 waveguide, is caused by a suppression of backscattering compared to the W1 waveguide. Therefore, work on reducing the propagation loss in engineered waveguides should be focused on reduction and control of the backscatter component.

A comparison of the electric field intensity for an engineered waveguide and a standard W1 waveguide (fig. 43) shows a significant difference. In the slow light regime, the field of the dispersion engineered waveguide is spread out uniformly over the defect region and the first three rows of holes, while that of the W1 waveguide is still concentrated within the defect region. This result lends support to the idea that a difference in the overlap between the electric field and the photonic crystal holes, described mathematically through ρ, could be the origin of the difference in propagation loss between these waveguides. The most noteworthy point is that the field in the engineered waveguide is spread out over a much larger area than that of the W1. In order to examine the effects of these field distributions in more detail, fig. 44 shows ρ against n_g plotted for both devices as well as the component of ρ due to each row of the photonic crystal. Initially, the backscattering for both devices is dominated by the first row of holes, directly adjacent to the defect waveguide. Furthermore, this value is slightly smaller for the W1 waveguide leading to a slightly lower propagation loss

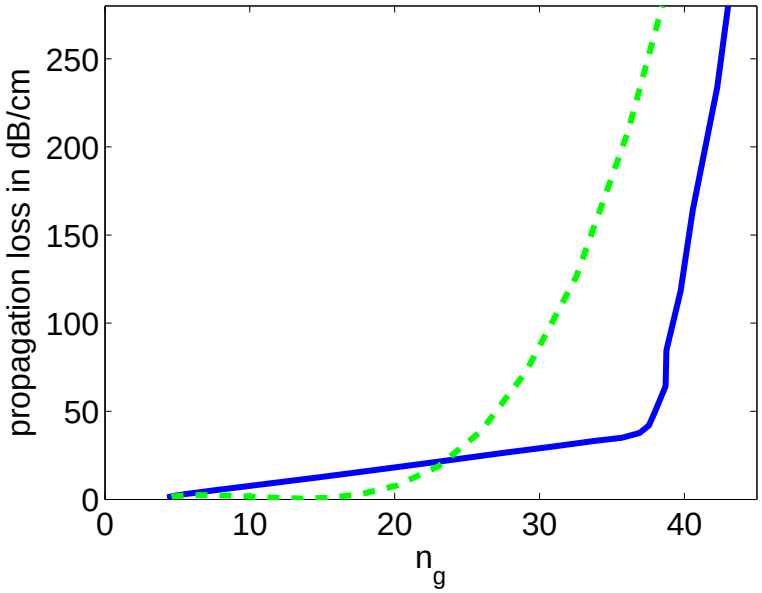

Figure 42: Graph showing backscattering loss for a W1 (dashed green line) and a dispersion engineered waveguide (solid blue line). The lower propagation loss for higher group indices of the engineered waveguide is due to the suppression of backscattering.

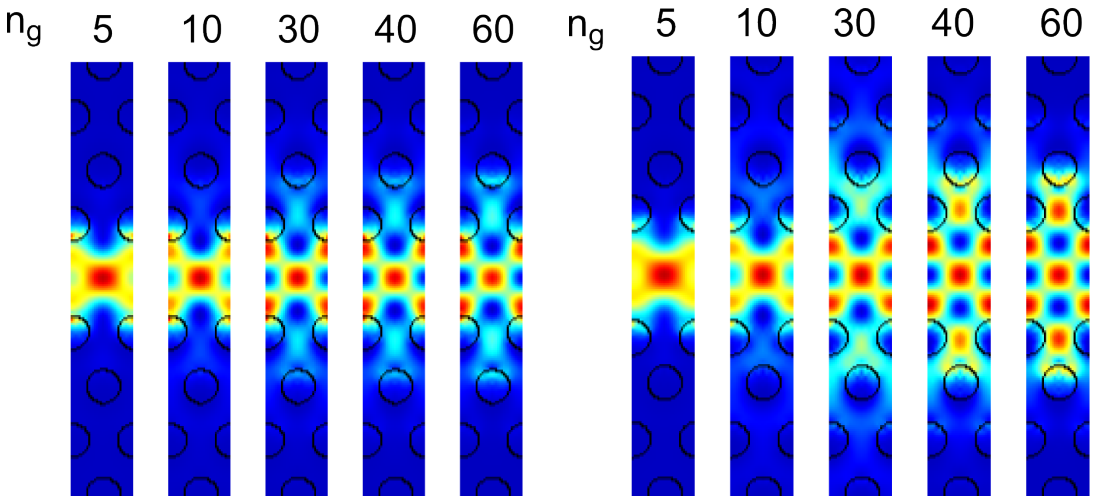

(a) W1 (b) dispersion engineered

Figure 43: Intensity distribution at different group index values for **a)** a W1 waveguide and **b)** the dispersion engineered waveguide. For the W1 waveguide, the field is always concentrated on the inside edge of the first row of holes and in the defect region. The field distribution for the dispersion engineered waveguide shows a much stronger group index dependence. A lower proportion of the field lies on the inside edge of the first row, while more is on the second row and between the holes of the first row. This more uniform field distribution leads to a slightly lower total scattering in the slow light region.

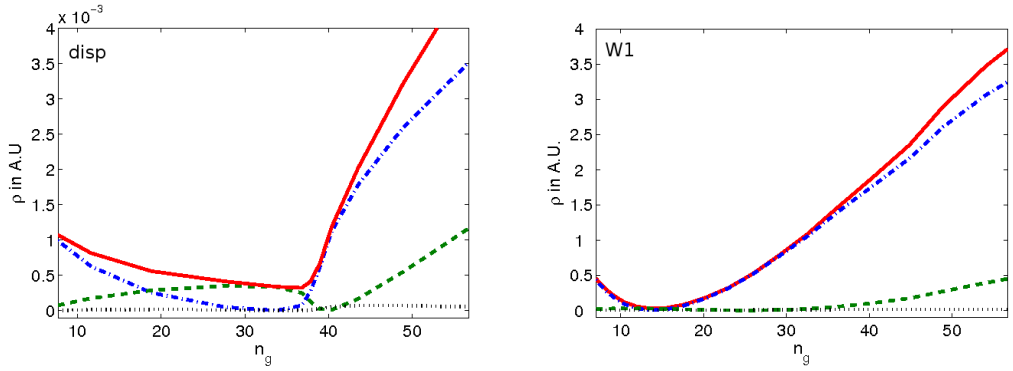

(a) (b)

Figure 44: Graphs showing ρ for different rows of holes. **a)** shows the engineered waveguide, while **b)** is for a W1 waveguide. The graphs include the total ρ (solid red line), the components from the first (blue dot-dashed line), second (green dashed line) and third row (black dotted line). For the W1 waveguide the value of ρ is initially lower, but increases for a lower group index than for the engineered waveguide. Also the W1 backscattering is always dominated by the first row, the second row never contributes a significant amount, in contrast to the engineered waveguide, where the second row has a significant contribution.

in the fast light regime, in good agreement with experimental data. However, as the group index is increased, the backscattering coefficient increases for the W1 waveguide, while it initially decreases for the engineered waveguide. Surprisingly, as the group index increases, the field of the engineered waveguide spreads out significantly and the backscattering of the 2nd row starts to dominate over that of the first row, an effect not observed for the W1 device, where the field distribution has only a weak group index dependence. While an interesting result in itself, it also provides us with two potential mechanisms for the reduction of propagation loss. If the minima in backscattering from both the first and second row would coincide on the same group index value, the resulting waveguide would have a significantly lower propagation loss. Alternatively, if the maximum in the backscattering from the second row can be reduced, the overall propagation loss will be reduced, too.

4.2 Propagation loss against wavevector

In order to make significant progress in our development of low loss waveguides, we need to once more consider a basic question on the nature of propagation loss. In the literature, propagation loss is generally presented as either a function of wavelength or of group index. While it is understandable to present propagation loss as a function of wavelength, the scalability of Maxwell's equations implies that wavelength cannot be a fundamental quantity for

optical processes. The presentation of loss as a function of group index is also understandable. After measuring both the propagation loss and group index as function of wavelength, it is easy to link these two to give the resulting loss vs group index curves. Additionally, loss is clearly dependent on the group index, as shown in eqn 20, and the operating group index is an important parameter in the design of photonic devices for optical delay and non-linear optics applications. However, this view can lead to a major misunderstanding, as it is now tempting to view γ and ρ as functions of the group index. This description also poses a serious problem, namely how to best describe the propagation loss of overengineered waveguides. These waveguides have a peak in the group index curve, followed by a flat region, leading to three wavelength values with the same group index, as shown in fig. 45. When plotted against group index, the propagation loss shows three different values for the same group index. This is not a spread caused by statistical variations, but represents an intrinsic difference, as each loss value corresponds to a different operating wavelength. Since a mathematical function has to be a 1:1 mapping, propagation loss cannot be viewed as a function of n_g. Furthermore, upon examination of a band structure diagram, we can see that the wavevector, and not the group index, is the fundamental quantity describing the system. Therefore, all variables in eqn 20 should be viewed as functions of the wavevector, k, such that:

$$\alpha(k) = c_1 * n_g(k) * \gamma(k) + c_2 * n_g^2(k) * \rho(k) \tag{21}$$

In this representation, the propagation loss of a photonic crystal waveguide, including over-engineered devices, shows a clear 1:1 mapping to the k-vector (fig. 45).

Treating propagation loss as a function of the wavevector has an additional advantage, allowing a better comparison of different engineered waveguides and providing important insight into the design of low loss waveguides. In the next section, I will use a case study, consisting of two dispersion engineered waveguides, both optimised for $n_g \approx 40$ (see fig. 46), to demonstrate the additional insight gained and to derive some rules for low loss waveguide design.

4.2.1 Propagation loss for different engineering methods

The two waveguides are based on different dispersion engineering methods. The first waveguide, device A, has the holes shifted perpendicular to the waveguide (lateral hole shift), while the second one, device B, is based on longitudinal hole shift (holes shifted along the

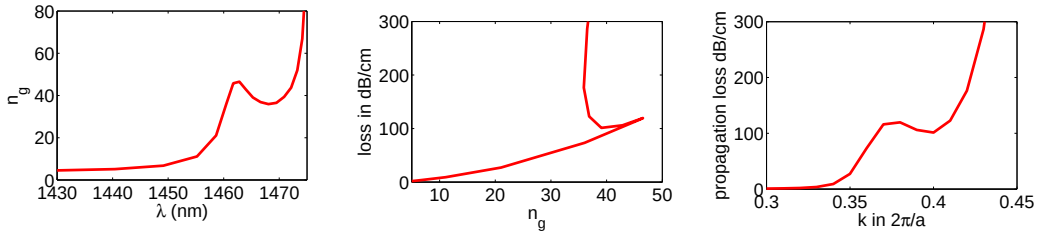

(a) (b) (c)

Figure 45: **a)** Group index curve for a "overengineered" waveguide. A waveguide is called overengineered when the group index curve shows a peak, followed by a flat region. Due to this peak, three wavelength values have the same group index. **b)** Propagation loss of this waveguide, plotted against group index. Light of a different wavelength, but with same group index, experiences significantly different propagation loss, disproving the notion that propagation loss is a function of group index. Instead, both propagation loss and group index are a function of the wavevector k. **c)** Propagation loss plotted against wavevector k. The 1:1 mapping necessary for a functional dependence is restored.

waveguide). As we can see, the propagation loss for device A initially scales linearly with group index, resulting in a lower loss in the flat band region than for device B, which has a parabolic loss curve. Examining the backscatter coefficient for different rows reveals several significant differences between the two waveguides. For device B, the second row contributes very little to the overall backscatter, an effect that, according to my previous discussion, should lead to a lower overall propagation loss. However, the minima in backscattering from the first and second row are further apart than for device A and the backscatter coefficient increases significantly earlier for device B. The combination of these two factors leads to a higher propagation loss in the slow light region. To understand the different backscatter distributions, fig. 48 shows the intensity distribution of both waveguides for $k = 0.38$, where the overall backscatter is equal. For device A, the field is spread out over the defect region and the first three rows of holes, while device B has a high field concentration in the defect region and on the first row only, consistent with our results for ρ. As the k-vector is increased to $k = 0.42$, the field distribution for both waveguides changes. For device A, the field spreads out further into the first and second row, with the highest field concentration in the silicon slab, away from any defects. For device B however, the concentration on the hole boundaries increases, leading to a sharper increase in backscattering and therefore overall propagation loss.

In fig. 49, we can see the overall backscatter coefficient of both devices and the group index curves plotted on the same axes. Due to the high scattering from the second row, device A has a slightly larger backscatter for low k-values, in the fast light region. However,

(a) device A (b) device B

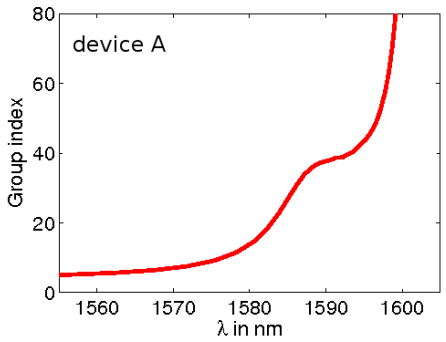

(c)

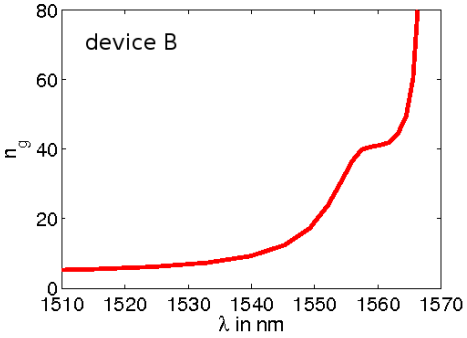

(d)

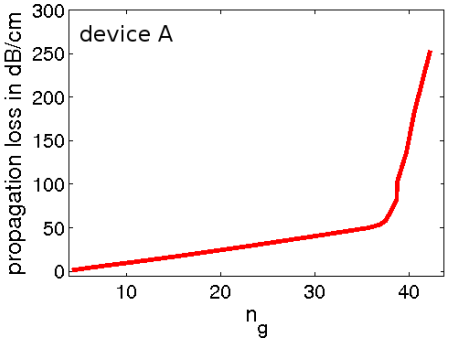

(e)

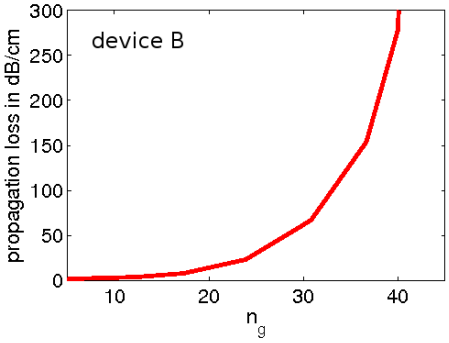

(f)

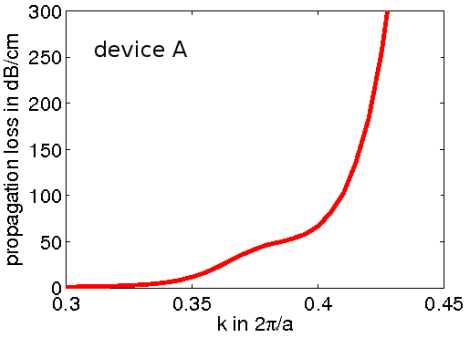

(g)

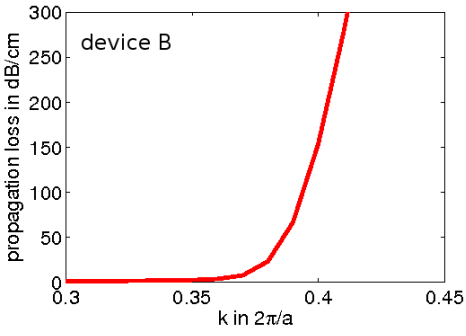

(h)

Figure 46: Graphs of group index (**c** and **d**) and propagation loss (**e**, **f**, **g** and **h**) for two different photonic crystal waveguides, used as a case study. Both devices are designed to have a low dispersion near $n_g = 40$. Device A (graphs **a**, **c, e** and **g**) was designed using the lateral (perpendicular to waveguide) hole shift method, while device B was designed using the longitudinal (along the waveguide) hole shift method. The group index curves alone are not sufficient to identify the waveguide better suited for operation in the slow light regime. From the propagation loss curves, when plotted against group index (**e** and **f**), we can see that device A has significantly lower propagation loss in the region of interest. Although loss is not a function of group index, according to the mathematical definition, these plots allow a quick identification of suitable devices. However when studying the underlying principles, propagation loss should be plotted against the wavevector, as shown in **g** and **h**.

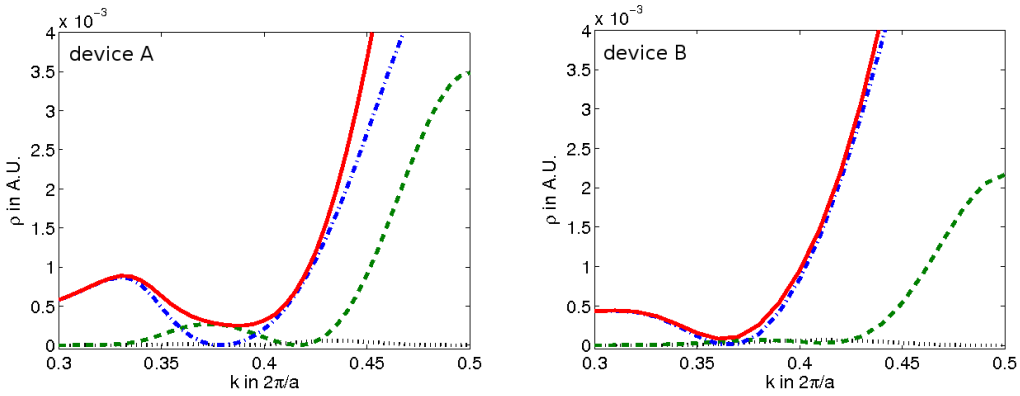

(a) (b)

Figure 47: Graphs showing the contribution to ρ from different rows, for **a)** device A and **b)** device B. The contributions shown are from the first row (blue dot-dashed line), the second row (green dashed line) and the third row (black dotted line). The sum of all contributions is shown as the solid red line. The second row has a much stronger contribution for device A, but the minima for both the first row and the summation are close to the bandedge for this device. Additionally, the minima of the first and second row are closer together for device A.

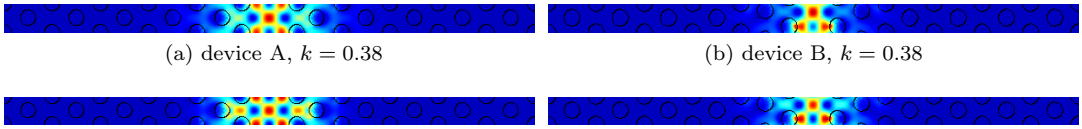

(a) device A, $k = 0.38$ (b) device B, $k = 0.38$

(c) device A, $k = 0.42$ (d) device B, $k = 0.42$

Figure 48: Images showing the energy distribution within the two waveguide designs, at different k-vectors. The field in the lateral hole shift device is spread out over the first three rows of holes, and a significant proportion of the field is contained between the first and second row, leading to an increase in the scattering from the second row. For device B however, a large proportion of the field is contained on the inside edge of the first row and very little spreads to the second row, explaining the lower backscatter from this row. However the more uniform energy distribution of device A shifts the minima in ρ closer to the bandedge.

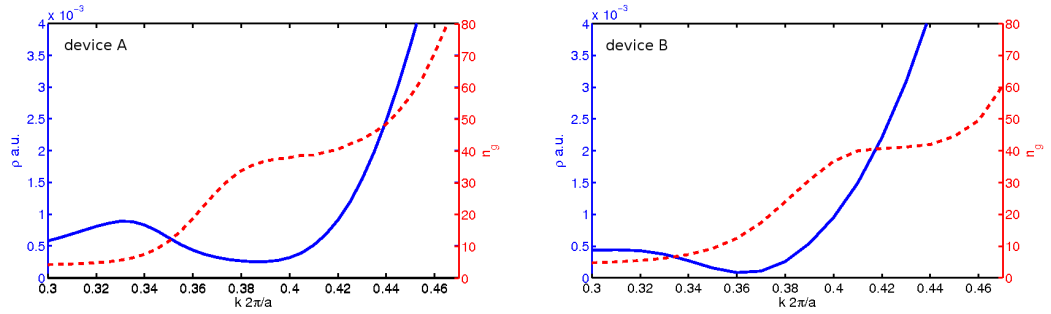

(a) (b)

Figure 49: Plot of ρ (solid blue line) and n_g (dashed red line) against k for **a)** device A and **b)** device B. Device B has lower backscatter initially, explaining the lower propagation loss in the fast light region. However, there is no overlap between the low dispersion region and the region where ρ is low (low backscatter region). Device A has a higher backscatter at the ρ minimum, but the backscatter is low for most of the low dispersion slow light region, leading to a lower slow light loss and therefore a suitable design for many slow light applications.

the increase in backscattering is closer to the bandedge, compared to device B, leading to an increased low loss bandwidth. Furthermore, the flat band slow light region for device A begins at lower k-values, leading to a large overlap of the low backscatter and low dispersion regions. Nearly all of the flat band slow light region shows low loss behaviour for device A, while device B has negligible overlap between the slow light and low backscatter regions, resulting in high propagation loss for the slow light region.

4.3 Design rules for low loss waveguides

We can now summarise the different criteria for low loss waveguides. First of all, the k-position of the minima in backscatter from the first and second row should be matched, as much as possible.

Secondly, the maximum in backscattering from the second row should be reduced, resulting in lower propagation loss, assuming that it does not increase the mismatch between the minima in backscattering from the first two rows.

And finally, the minima in backscattering and the flat band slow light region have to be matched, as an increased overlap reduces the propagation loss in the region of interest.

4.3.1 Matching the minima of different rows

It is easy to understand that a closer match of the minima of ρ, for the first and second row, will lead to lower overall backscatter (for this given k-value). Therefore the effect of different

engineering methods on this mismatch should be investigated. Fig. 50 shows the distance between the k-values of the two minima, for both lateral and longitudinal hole shifts. We notice that the behaviour is a lot more regular for the lateral hole shifted designs. Here, the second row minima is always at higher k-values than the first row minima. For the longitudinal hole shift method however, some designs do not show a clear dip in the second row backscatter, instead it increases monotonically and therefore the 2nd row minima is far away from the slow light region, while others have a second row minima in the slow light region, but with a larger mismatch. We can also conclude that as s_1 is increased, the mismatch between the two minima is increased, while increasing s_2 leads to a decreased mismatch for low s_1 values, and an increase for larger s_1 values. We can see that devices in the range of $s1 = 0.10a$ to $0.12a$ and $s2 > 0.04a$ provide the lowest mismatch between the minima. At this point, it is worth noting that values of s_1 and s_2 lying outside of this graph were not investigated, as they provide poor slow light performance, with either very low group index or GBP [12].

Furthermore, while the spacing between the minima is decreased slightly, as s_2 is increased (in the region of interest defined above), the absolute value of ρ for these minima is increased, as shown in fig. 50. Therefore an optimum operating point has to take both factors into account.

4.3.2 Reducing backscatter from second row

The strong backscattering from the second row of holes is a consequence of the engineering methods used to create the first loss engineered waveguides. By shifting the first row of holes away from the waveguide, and the second row towards it, the field between these holes is squeezed into a smaller space, as shown in fig. 51. The resulting increased overlap with the surface of the second row of holes leads to the increased backscatter. The contribution of the second row of holes can be reduced, by employing other engineering methods. However, these engineering methods have other problems associated with them. Reducing the waveguide width leads to a reduced mode volume in the defect region, forcing the field onto the hole in the first row and increasing the overall backscatter compared to lateral hole shifting [74], as shown in fig. 52. And, while the longitudinal hole shift reduces the backscattering from the second row, it reduces the overlap between the slow light and low backscatter regions, as shown in section 4.2. Therefore, a combination of the remaining two engineering methods,

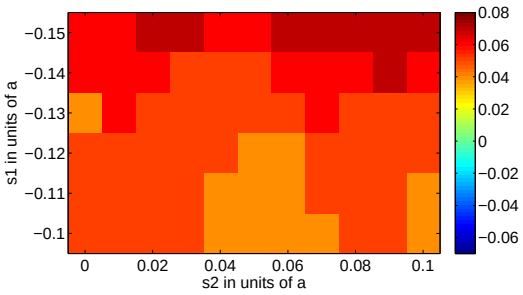

(a) Lateral hole shift

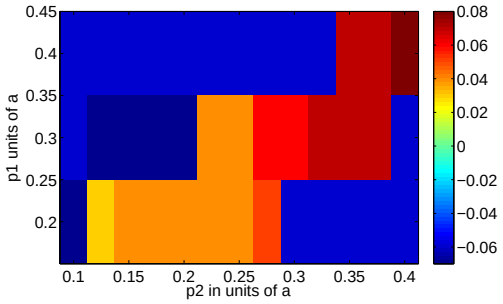

(b) Longitudinal hole shift

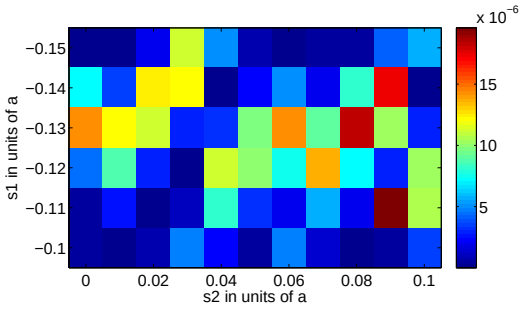

(c) Lateral hole shift

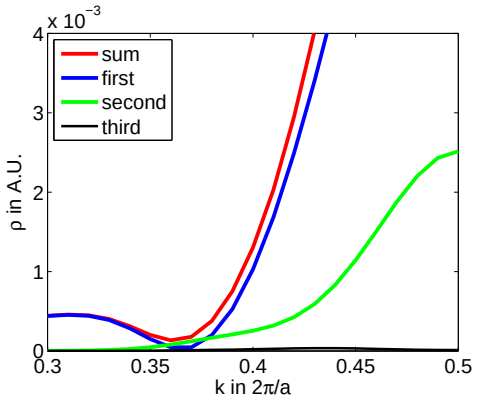

(d) Longitudinal hole shift

Figure 50: Plots of the spacing (Δk) of the minima in ρ of the first and second row for **a)** lateral and **b)** longitudinal hole shift. For the lateral hole shift, the minima spacing changes in a well behaved manner, as the holes are shifted. Generally a smaller s_1 shift brings the two minima closer together (the preferred situation). However, for the longitudinal hole shift method, a small change in the hole shift can lead to a major change in the spacing, making a systematic design of waveguides using this engineering method very difficult. **c)** Graph showing the value of ρ for the second row, at the minima for lateral hole shift engineered waveguides. The graph shows some fluctuations, related to the resolution of the calculation used, however a trend showing a slight increase for waveguides with a larger s_2 shift is recognisable. Furthermore, intermediate $s1$ values (-0.12 to -0.14) have slightly higher backscattering at this minimum, compared to larger, or smaller, shifts. **d)** Plot of the ρ contributions from different rows for a waveguide that was engineered using the longitudinal hole shift method. There is no minimum for the backscattering from the 2nd row, other than at $k = 0.3$. Therefore the backscattering from the second row does not decrease in the slow light region and this minimum cannot be used to offset the increase in backscattering from the first row.

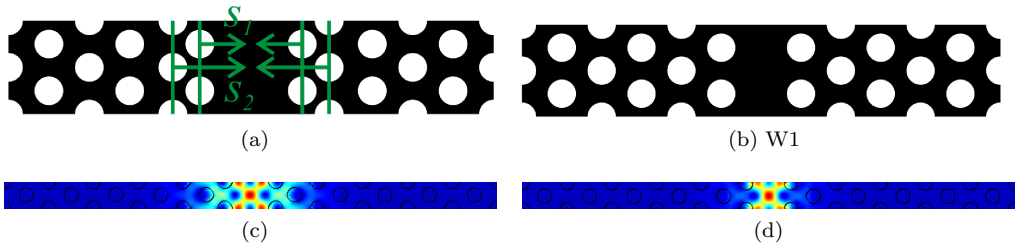

Figure 51: Sketch and field distribution for a lateral hole shift engineered waveguide, **a)** and **c)**, and a W1 waveguide, **b)** and **d)**. During the lateral hole shift engineering the first row is generally shifted away from the waveguide (s_1 is negative) and the second row is shifted towards the waveguide. Therefore the area between the hole is reduced and the field is squeezed onto the second row, leading to an increased backscatter from this row, compared to the standard W1 waveguide.

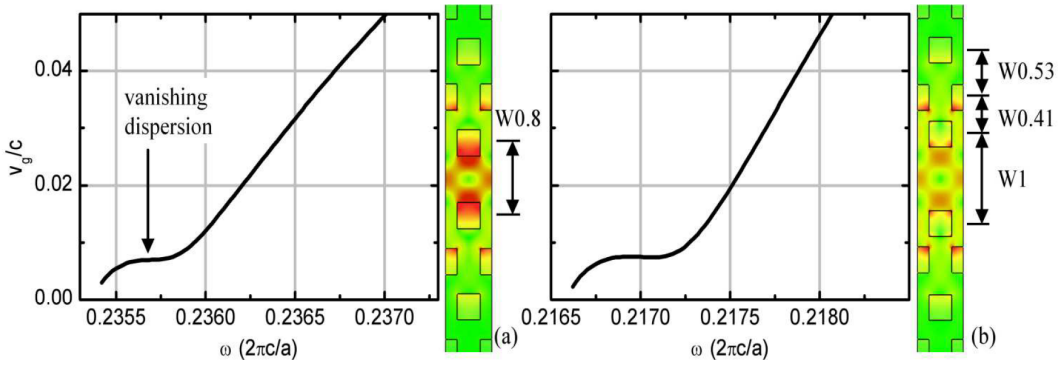

Figure 52: Group velocity curves and intensity distribution for **a)** width reduction and **b)** lateral hole shift engineered waveguides. Although both waveguides have a nearly identical group velocity curve, the W0.8 waveguide has a much higher field concentration on the inside of the first row of holes. This increased overlap leads to an increased propagation loss. Figures are from reference [74]

the lateral hole shift and radius variation, was investigated. Reducing the radius of holes in the second row leads to a reduction of the backscatter from this region, as shown in fig. 53, promising a significant reduction in the propagation loss. Values as low as 20 dB/ns have been predicted. This value is closer to the propagation loss in ring resonators based on SiON (10 dB/ns) [82] than ring resonators or other loss engineered photonic crystals in silicon (60 dB/ns and 35 dB/ns respectively) [13]. The downside of this engineering method is a reduction in the achievable group index, associated with the reduced radius of the second row.

Despite this strong reduction in group index and GBP, these waveguides show promise for use in stimulated Raman scattering, a process which has a n_g^2 dependence, in principle, and therefore is very sensitive to the slow light enhancement of the propagation loss [21]. If the propagation loss also scales with n_g^2, then the increased Raman scattering efficiency is cancelled out by the increased propagation loss. However, if the propagation loss has a weaker dependence on the group index, then slow light enhancement of stimulated Raman scattering is possible, as explained in more detail in section 4.5.2.

4.3.3 Increasing the overlap between the low loss and flat band slow light regions

The third criterion for a low loss waveguide is the overlap between the flat band slow light and the low loss regions, as demonstrated in the case study presented earlier (section 4.2). Upon comparison of a range of shifts, the lateral hole shift method provides a better overlap once again (fig. 54). Therefore we can conclude that the better performance presented during the case study was not a coincidence. An examination of fig. 54 reveals that a higher s_1 (until $s1 = -0.14a$) and a lower s_2 shift provide the best overlap of the low loss and flat band slow light regions. However, as before, we need to remember that this is not the only criterion that should be considered.

4.4 Alternative waveguide designs

In the previous paragraphs, the discussion focused on lateral and longitudinal hole shifts. However, this focus does not imply that other potential designs were not investigated. In this section, I will explain why other designs did not present an improvement in device performance and were not investigated in the same detail as the designs discussed above.

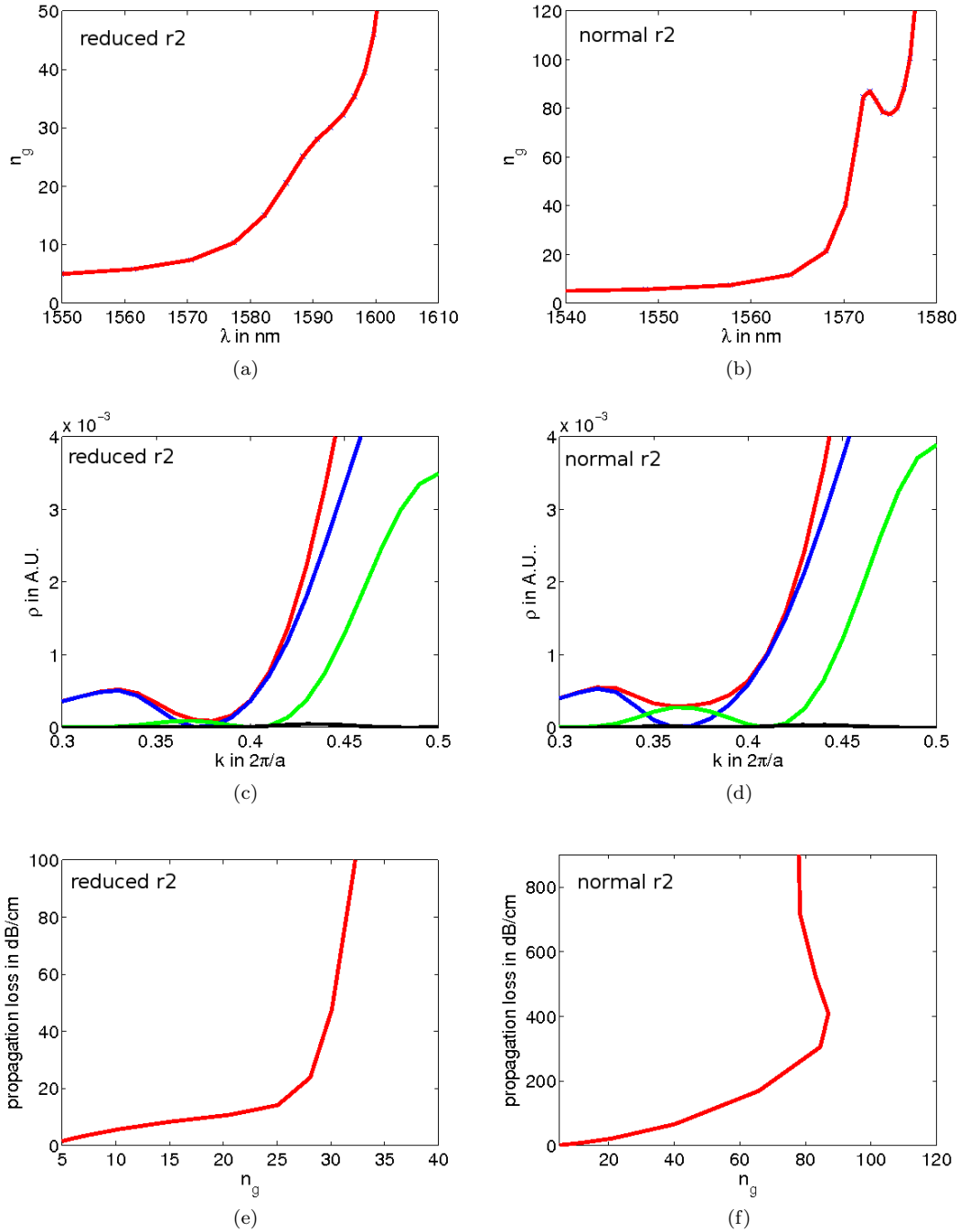

Figure 53: Graphs showing group index (**a** and **b**), ρ from different rows (**c** and **d**) and resulting propagation loss (**e** and **f**) for an engineered waveguide where the second row radius is reduced, from $0.285a$ to $0.24a$ (**a**, **c** and **e**) and the original engineered waveguide, i.e. same hole shifts, but all rows with equal radius (**b**, **d** and **f**). The reduction in the second row radius leads to a strong reduction in the scattering from the second row, and therefore the propagation loss. However it also results in a strong reduction of the achievable group index.

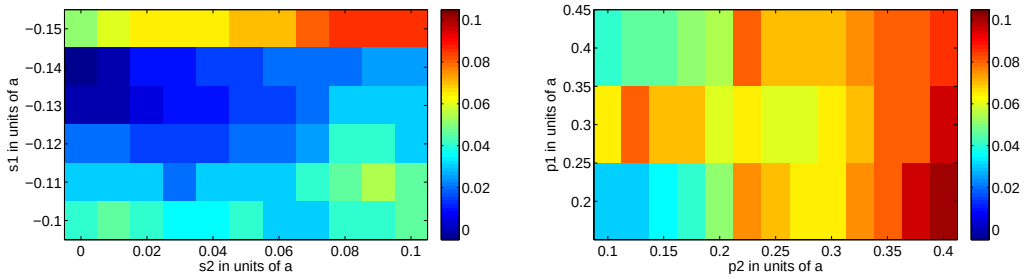

(a) (b)

Figure 54: Figures showing the mismatch (in k) between the backscatter minima and the design group index for **a)** lateral and **b)** longitudinal hole shift engineering. We can see that the lateral hole shift waveguides generally have a better overlap, resulting in lower propagation loss in the slow light region and explaining why many applications, utilising slow light enhancement, have been demonstrated in these devices.

Radius variation on its own was not considered in detail (the same lattice symmetries are present and previous publications have failed to provide GBP comparable to other engineering methods [12, 33, 35]). Instead, designs with different lattice symmetries, specifically asymmetric waveguides and square lattice based waveguides, were investigated.

Asymmetric waveguides, which have an $a/2$ shift between the holes on either side of the waveguide, as shown in fig. 55, were investigated, since previous work had shown a strong reduction in out of plane loss for devices operated above the light line [83]. The reduced propagation loss was attributed to destructive interference of the leakage component of the modes originating from different sides of the waveguides. The asymmetric structure of these waveguides leads to a hybridization of the odd and even waveguide modes, leading to potentially higher coupling loss at interfaces. However, the work on these devices, although spanning a large parameter range, including variations of the waveguide width, failed to identify any design with a suitable slow light region. As shown in fig. 55, the waveguide modes disappear into the bulk photonic crystal modes, instead of forming the anticrossing typical for normal, symmetric, waveguides. Therefore the basic requirement for dispersion engineering is not fulfilled. Additionally, the region of the mode within the bandgap is multimodal. For every wavelength value, there are two k-components that are supported, one of which lies above the light line, leading to increased out coupling (although these PhCs have a lower loss above the light line than normal PhCs, it is still an additional loss component and therefore should be avoided).

During previous work, F. Leng *et al.* [84] have demonstrated dispersion engineering

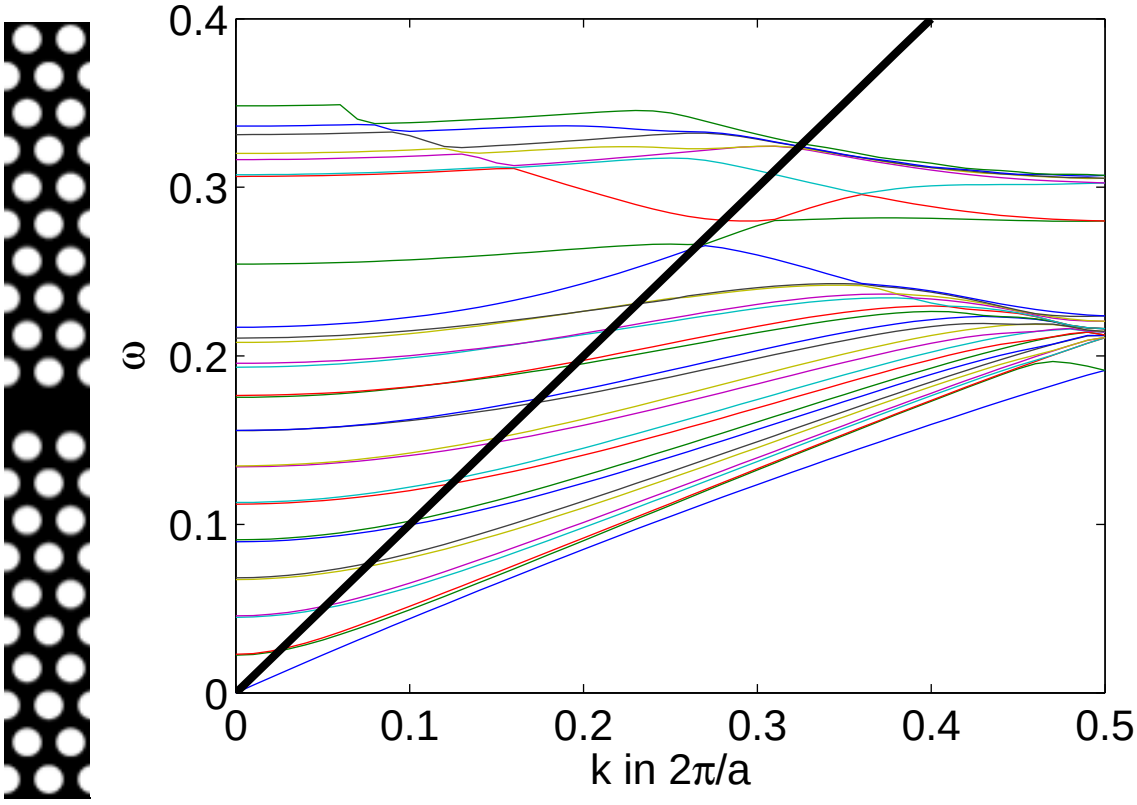

(a) (b)

Figure 55: **a)** Sketch and **b)** typical bandstructure of a type B waveguide, where one side of the PhC cladding is shifted by $\frac{a}{2}$ along the waveguide. The light line is shown as a thick black line in the bandstructure diagram. From the bandstructure we can see that there is no single mode slow light region for this type of waveguide.

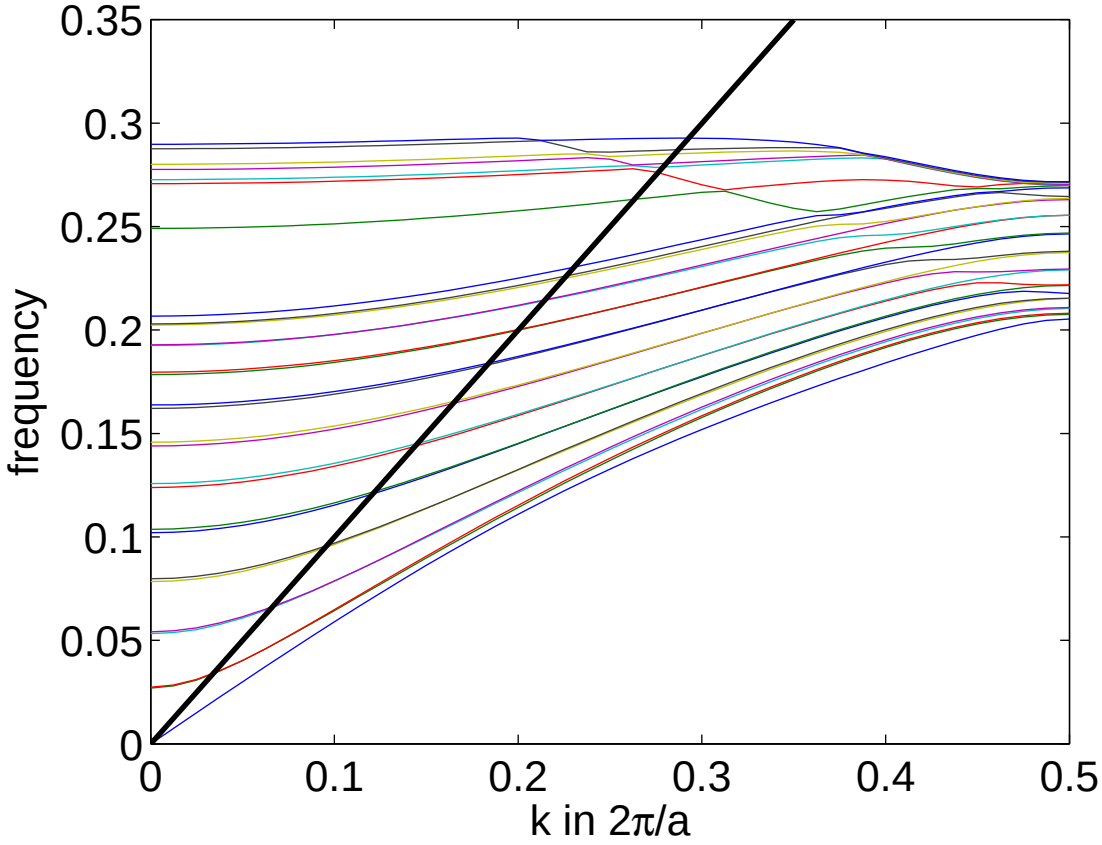

Figure 56: Typical bandstructure of a square lattice, air holes in silicon, PhC waveguide. It is clear that no band gap exists and therefore light confinement in the defect region is not achievable.

through a stretched lattice photonic crystal. However during this project, I discovered that small variations in the lattice do not lead to any significant variation in the waveguide properties, other than a wavelength shift, as utilised for the mode conversion interfaces (section 2.4.1). However, it inspired the investigation of square lattice photonic crystals as a potential candidate for low loss waveguides. Unfortunately, the reduced bandgap associated with the changed symmetry of the PhC cladding is not sufficient to create single mode slow light waveguides. As shown in fig. 56, waveguide modes could be created, but single mode operation could not be achieved. For each wavelength a bulk mode (resulting in high coupling through the photonic crystal cladding) or components of a guided mode above the light line were present, preventing intrinsically lossless waveguide designs.

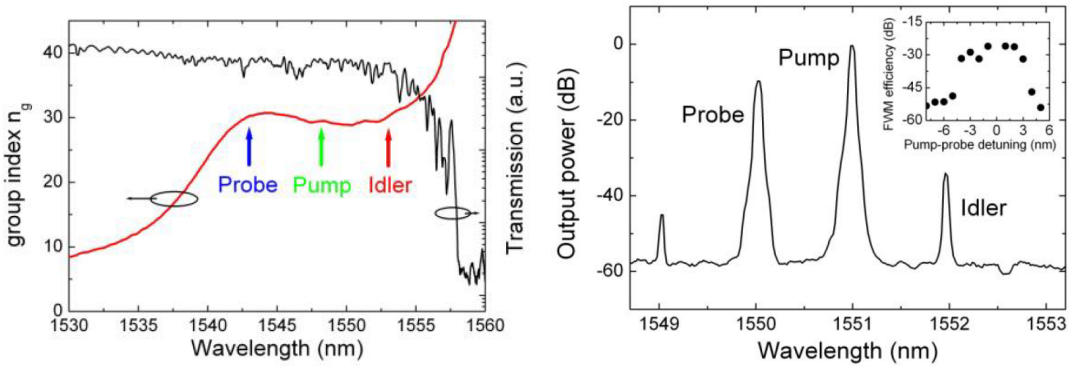

(a) (b)

Figure 57: **a)** Group index and transmission curve of a dispersion, and loss, engineered waveguide, used for FWM. **b)** FWM signal obtained in this waveguide. Due to the large slow light bandwidth all three wavelength (pump, signal and idler) are slowed down and phase matching is preserved. Figures taken from reference [9]

4.5 Advice for low loss waveguides

In this section, I will provide a short summary of the design rules and, through a combination of these rules, present advice for the design of two different types of waveguides.

We have seen that the different design rules can all have significant impact on the final device performance and, unfortunately, the change of key design parameters can have diverse and countervailing effects. For example, shifting the first row further away from the defect region leads to a better overlap of the low backscatter region with the slow light region, while at the same time increasing the spacing between backscattering minima (and the value of these minima), increasing the total backscatter in this region. Therefore, there is no best photonic crystal, or "one fits all", waveguide. Instead, the waveguide design needs to be adapted for the application at hand. In this section, waveguides for four wave mixing and Raman scattering will be presented.

4.5.1 Slow light waveguides for four wave mixing

Four wave mixing (FWM) is a popular candidate for demonstrations of slow light enhancement in silicon, due to the predicted S^4 scaling, where the slow down factor $S = \frac{n_g}{n_{phase}} \approx \frac{n_g}{3}$. The FWM intensity is dependent on the intensity of the signal, idler and pump photons. Since photons at all three wavelengths can be slowed down using a dispersion engineered waveguide (see fig. 57) and two pump photons are involved, the FWM efficiency (η) scales

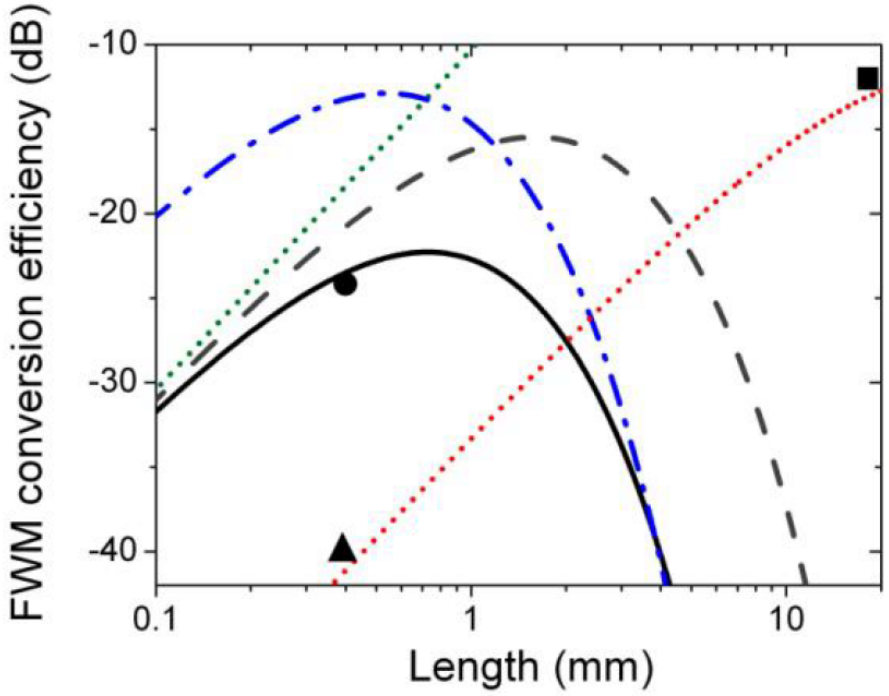

Figure 58: Graph showing FWM efficiency against sample length for different structures. The black dot, circle and square correspond to experimental reported values. The red dotted curve is a photonic nanowire [85], while all other curves represent PhC waveguides. The solid black curve is for the waveguide from fig. 57. This waveguide had roughly twice the disorder of the waveguides discussed in this and the previous chapter, mainly due to a larger number of stitching errors. The black dashed curve is for a waveguide with the same group index curve, but the roughness assumed for the loss engineering calculations. The green dotted curve is for this waveguide in the absence of propagation loss, while the blue (dot-dash) curve is for a waveguide optimised for operation at $n_g = 60$. The strong decay of FWM efficiency with device length, after the optimal point is passed, shows the importance of low loss waveguides. The comparison with a nanowire shows that slow light enhancement in PhC allows for a order of magnitude reduction of the device footprint. Figure taken from reference [9]

as S^4 [8, 9, 85]:

$$\eta = S^4 \gamma^2 \overline{P}_{pump}^2 L^2 e^{-\alpha L} \psi \tag{22}$$

where the nonlinear parameter $\gamma = 2\pi n_{2\text{eff}} / (\lambda A_{\text{eff}})$ contains the effective nonlinear index ($n_{2\text{eff}}$) and effective mode area (A_{eff}). $\overline{P} = P(0) * \left(1 - e^{-\alpha L}\right) / \alpha L$ is the average pump power, α is the propagation loss, L the device length and ψ the phase factor, in accordance with eqn 1 from reference [9]. It follows from eqn 22 that propagation loss has a fundamental impact on the FWM efficiency. First of all, an increase of propagation loss with group index leads to a reduced average pump power. However, the propagation loss also limits the usable device length, as shown in fig. 58. As the device length is increased, both signal

and pump power are reduced due to propagation loss. Initially, the high pump power leads to a faster generation of signal photons through FWM than are lost through out of plane or backscattering. However, as the device length is increased further, the pump power is depleted through the propagation loss, reducing the signal generation rate until it is exceeded by the signal propagation loss. Any further propagation through the PhC waveguide leads to a reduction of the signal power and therefore FWM efficiency. A photonic crystal waveguide for FWM should have a high group index, to maximise the S^4 scaling. Furthermore, it requires a wide bandwidth, as pump, signal and idler wavelength should be slowed down. And last but not least, a good overlap of the low loss and low dispersion regions is necessary, to increase the usable device length. This combination is best achieved for waveguides with a small shift of the first row ($s_1 = -0.1a$) and a medium shift of the second row ($s_2 = 0.03 - 0.06a$). The resulting waveguides can have $n_g = 60$ with 5 nm bandwidth ($GBP = 0.2$) and 130 dB/cm propagation loss, assuming the same fabrication quality as in section 3.3.

Due to the strong dependence of the FWM efficiency on the slow down factor, the group index is the key parameter for waveguide design and good results an be achieved in the presence of high propagation loss (130 dB/cm).

4.5.2 Slow light waveguides for stimulated Raman scattering

Stimulated Raman Scattering (SRS) is of interest to the photonics community, since it is a potential mechanism for the generation of light in silicon. Successful Raman amplification, net gain and lasing have been demonstrated in silicon waveguides [86, 87, 88]. Raman scattering in silicon is of high interest, due to the high Raman gain ($g = 20\,\mathbf{cm/GW}$) [21]. Early work on Raman scattering in photonic crystal waveguides predicted a strong slow light enhancement of SRS [6]. However, a more thorough study, assessing the impact of propagation loss on Raman scattering was needed. This study, conducted by I. Rey *et al.* [21], showed the importance of application specific waveguide design.

The Raman gain in PhC waveguides is affected by several parameters, including the group index of both the pump and signal beams. Therefore, the first question is if the pump photons, signal photons or both should be slowed down. A design that slows down both the pump and signal is not easily realisable, due to the large pump-signal detuning (15.6 THz). Slowing the signal down does not lead to a change in the gain threshold, it simply reduces the

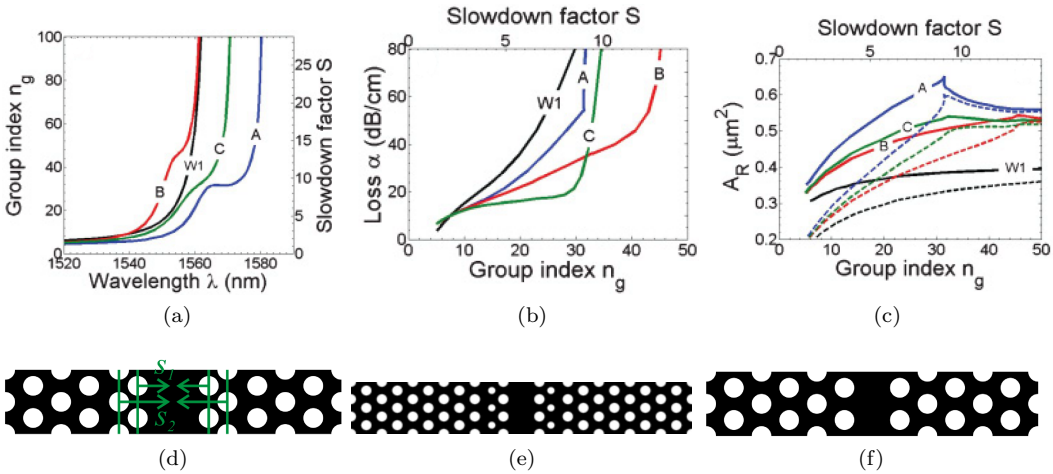

Figure 59: Graphs showing **d)** group index, **b)** propagation loss and **c)** effective Raman area for different photonic crystal waveguides. Device A is engineered using the lateral hole shift method (**d**), while devices B and C are engineered using a combination of lateral hole shift with a reduction of the second row radius (**e**). The standard W1 waveguide is shown in **f)**. The Raman area should be as small as possible, since a smaller mode volume leads to higher intensities inside the waveguide. In **c)** the solid lines are for waveguides aligned along the [110] crystal plane, while dashed lines are for waveguides along the [100] direction. Reprinted with permission from [21]. © 2011 by the American Physical Society

optical length necessary for the maximum gain, while slowing the pump down can result in a shift of the threshold power for the transition from net loss to net gain. Other parameters affecting SRS are the effective mode area and the propagation loss at both pump and signal wavelength.

Here, I will use the examples from reference [21]. In this theoretical study, the signal was slowed down, while the pump wavelength was in a fast light mode, due to the sources available for subsequent experimental work. While slowing down the signal is the worst option for SRS, as it only leads to a linear enhancement of the gain, it is also the easiest to implement using PhC waveguides. Fig. 59, shows the group index and propagation loss of different waveguide designs, which were calculated using the code developed in chapter 3.3, and the effective area, calculated using eqn. 9 from [21].

The designs presented here are a standard W1 waveguide, a lateral hole shift device (A) and waveguides based on lateral hole shift combined with a reduction of the second row radius, to reduce propagation loss further (B and C). As before, the reduction in the second row radius leads to worse slow light performance (in this case a reduced GBP), but a significant reduction in propagation loss. While the W1 waveguide has the best effective area, in good agreement with the mode shapes shown in section 4.1, devices B and C have

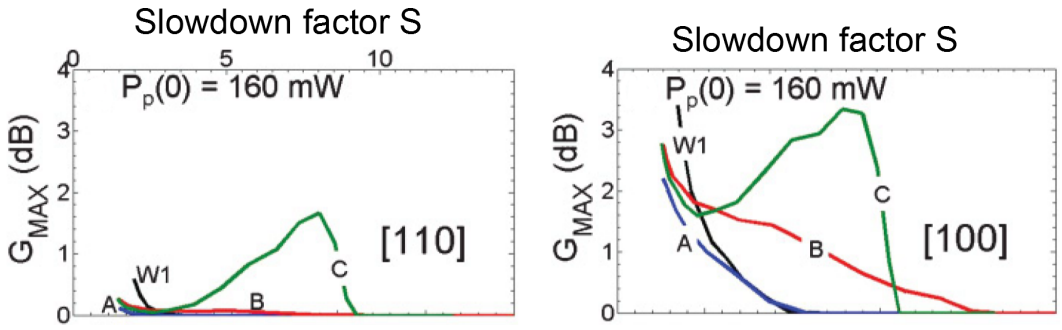

(a) (b)

Figure 60: Graphs showing theoretical Raman gain for the PhC waveguides discussed for different lattice orientations. The curve for each device at its optimum length is shown, with typical values in the range of $5 - 7$ mm. This compares favorable with the highest reported Raman gain, 3.7 dB in a 4.8 cm long rib waveguide and at much higher pump power (748 mW) [88]. Figures taken from reference [21].

significantly larger effective areas.

However, when examining the predicted Raman gain for these devices, at different waveguide orientations (fig. 60), device C performs best, due to the significantly slower increase of propagation loss with group index, demonstrating the importance of loss engineering for nonlinear optics applications.

While the group index was the key parameter that needed to be optimised for FWM (section 4.5.1), the situation is different for SRS. As shown here, the weak group index dependence of the Raman signal means that the propagation loss is the key parameter that needs to be optimised, as a sub linear scaling of propagation loss with group index is required for slow light enhanced SRS.

4.6 Propagation loss in slotted photonic crystal waveguides

In this chapter I have shown that significant progress has been made in the understanding of propagation loss in PhC waveguides, based on the calculation method presented in section 3.3. Furthermore, this improved understanding allows the design of application specific waveguides. However, our calculation method can also be extended to other photonic crystal based waveguide structures.

As an example, slotted photonic crystal waveguides [89, 90, 91] (see fig. 61) are of particular interest. Slotted waveguides, both wire and PhC based, are of interest in photonics, as they lead to high spatial field confinement in the air gap. The tight confinement results in high field intensities in the gap material, making slotted waveguides a suitable candidate for

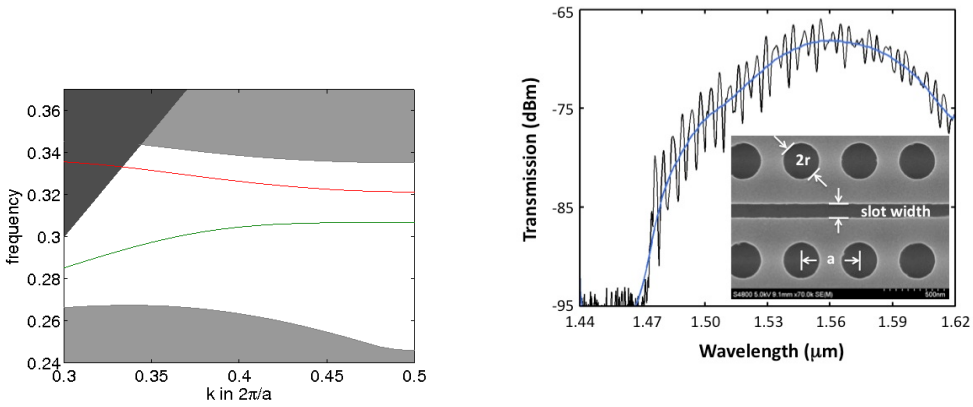

(a) (b)

Figure 61: **a)** Bandstructure diagram of a slotted PhC (see inset in **b)**). The mode with high field intensity inside the waveguide slot is shown in green. **b)** Transmission spectrum of the slot waveguide mode and SEM image showing the waveguide slot and first row of holes. Graph **b)** courtesy of Dr. Di Falco.

optical sensing applications [92]. Again, photonic crystals can introduce further enhancement of light-mater interactions, through the slow light effect. Optical sensing [24], and electro-optic switching [93], using slotted PhC structures have already been demonstrated. However, to date, no investigation of propagation loss in slotted PhC waveguides has been presented.

Since our model is generic, it can be adapted to calculating the propagation loss in these structures. However, several assumptions have to be made.

- Our first assumption is that the disorder of the photonic crystal slot has the same rms value as that of the PhC cladding. This assumption is reasonable, as the slot dimensions (typically $100 - 200\,\text{nm}$) are comparable to the diameter of a photonic crystal hole. Therefore, the slot fabrication requires the same high resolution lithography and the resulting etch quality should be comparable to standard photonic crystals.

- A second assumption, concerning the coherence length of slot disorder, has to be made. This assumption is necessary due to a lack of experimental data. No measurements of propagation loss against group index are available, only measurements of propagation loss against slot width, excluding the possibility of a comprehensive study comparable to the one for PhC waveguides. Here, I assume that the slot sidewalls are similar to photonic wire sidewalls, justifying a $40 - 50\,\text{nm}$ coherence length (the coherence length

for the disorder on photonic crystal holes is still taken to be the hole circumference).

As with standard photonic crystal waveguides, a comprehensive study of propagation loss as a function of group index and waveguide design would be necessary to determine the correct calculation parameters.

With these assumptions, we can now express propagation loss in slotted photonic crystals as:

$$\begin{aligned} \alpha &= c_1 n_g \gamma + c_2 n_g^2 \rho \\ \gamma &= \gamma_{\text{holes}} + \gamma_{\text{slot}} \\ \rho &= \rho_{\text{holes}} + \rho_{\text{slot}} \end{aligned} \tag{23}$$

where c_1 and c_2 have the same values as used during the design of standard PhC waveguides. When comparing the calculated and measured propagation loss of slotted waveguides, we get good qualitative, if not necessarily quantitative agreement. Fig. 62 clearly shows that the propagation loss is dependent on the slot width, with a reduction in propagation loss for a slot width of around $125-145\,\text{nm}$, compared to narrower slots. The calculated data shows a similar behaviour for these width values, however it also shows that the curve of propagation loss against slot width is only locally flat, with even better loss values achievable for wider slots. In the slow light regime, this locally flat region is transformed into a local minimum, with a second minimum existing around 200 nm slot width. Here I would like to note that a larger slot also leads to a reduced group index in the fast light region (as the proportion of the mode in the air gap increases, the group index decreases). Furthermore, a wider slot has a lower field intensity inside the slot, implying that the lowest loss waveguide is not necessarily the best waveguide for applications. Additional work is needed to improve the quantitative agreement between the calculated and measured results. In particular, a measured group index curve should be used to check that parameters, especially hole diameter and slab height, of the fabricated structure match those of the simulated designs. Both of these values have an impact on the group index and propagation loss, and therefore need to be determined before a quantitative agreement can be reached. Furthermore, as already stated above, a comprehensive study, including measurements at different group indices, would allow an investigation of different values for the slot disorder coherence length, which is again expected to have significant impact on the group index scaling of propagation loss.

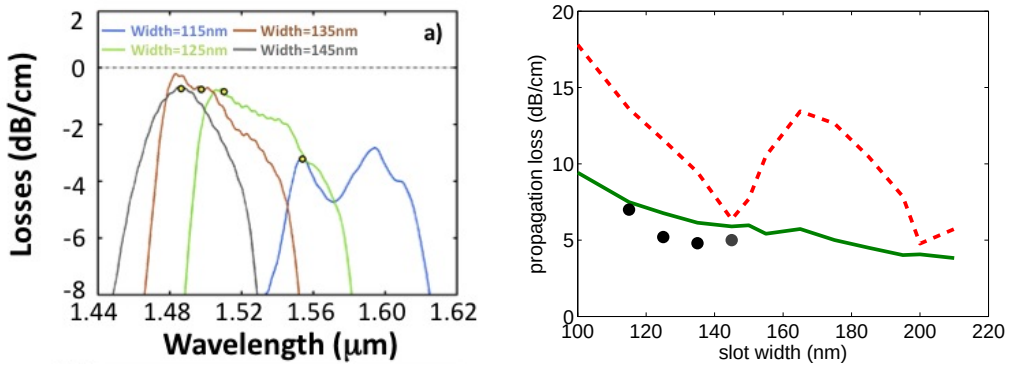

(a) (b)

Figure 62: **a)** Measured propagation loss against wavelength for slotted PhC waveguides of varying slot width. The loss for a narrow slot (115 nm) is significantly higher than for slightly wider slot widths. In this graph the loss value is the difference between a slotted PhC and the access waveguide. The typical propagation loss for access waveguides is around $4-6$ dB/cm, giving a total propagation loss around $5-7$ dB/cm **b)** Theoretical loss against slot width, in the slow (red dashes) and fast light (green) regime. No fitting parameters were used during this calculation. The black dots correspond to the circles in **a)**. The theoretical curves confirm that the propagation loss for 115 nm is significantly worse than for the other values. In the fast light regime the other experimental devices have similar propagation loss, in qualitative agreement with the experimental results. The theoretical data shows that there will be optimal values of the slot width in the slow light region, as far as the reduction of propagation loss is concerned. Graph **a)** courtesy of Dr. Di Falco

4.7 Conclusions

In this chapter, we have seen that waveguide design can have a big impact on the propagation loss in photonic crystals. Several rules for the design of low loss waveguides, and engineering methods to satisfy these rules, have been presented. Unfortunately, the engineering methods available have countervailing effects, i.e. they improve the device according to one rule, such as reducing overall backscatter, but make it worse according to a second rule, for example through a reduced overlap of the slow light and low loss regions. Therefore a balancing act is need during waveguide design, and the optimum device depends on the specific requirements of each application. This balancing act was demonstrated for the examples of SRS and FWM. Although both are nonlinear processes, they require very different devices. For FWM the device bandwidth, both for low loss and slow light, as well as a high group index are key, while the focus for SRS is on extremely low loss devices.

5 Improved fabrication methods

"Disorder: please, get in line!"

Andrea Melloni

5.1 Shot shifting

As already mentioned during the discussion of PhC fabrication in section 2.2, the finite resolution of the stage movements during electron beam lithography can lead to so called stitching errors, located at the writefield edges. These errors, which are typically on the scale of $10 - 20\,\mathrm{nm}$, but can be significantly larger (see fig. 63), are much larger than other types of disorder present, leading to significant propagation loss. A single stitching error carries a $0.07 - 0.1\,\mathrm{dB}$ penalty in transmission in the fast light region, resulting in $7 - 10\,\mathrm{dB/cm}$ propagation loss, assuming a waveguide written using $100\,\mu\mathrm{m}$ writefields. As for all other types of disorder, the optical scattering from stitching errors is enhanced further by the

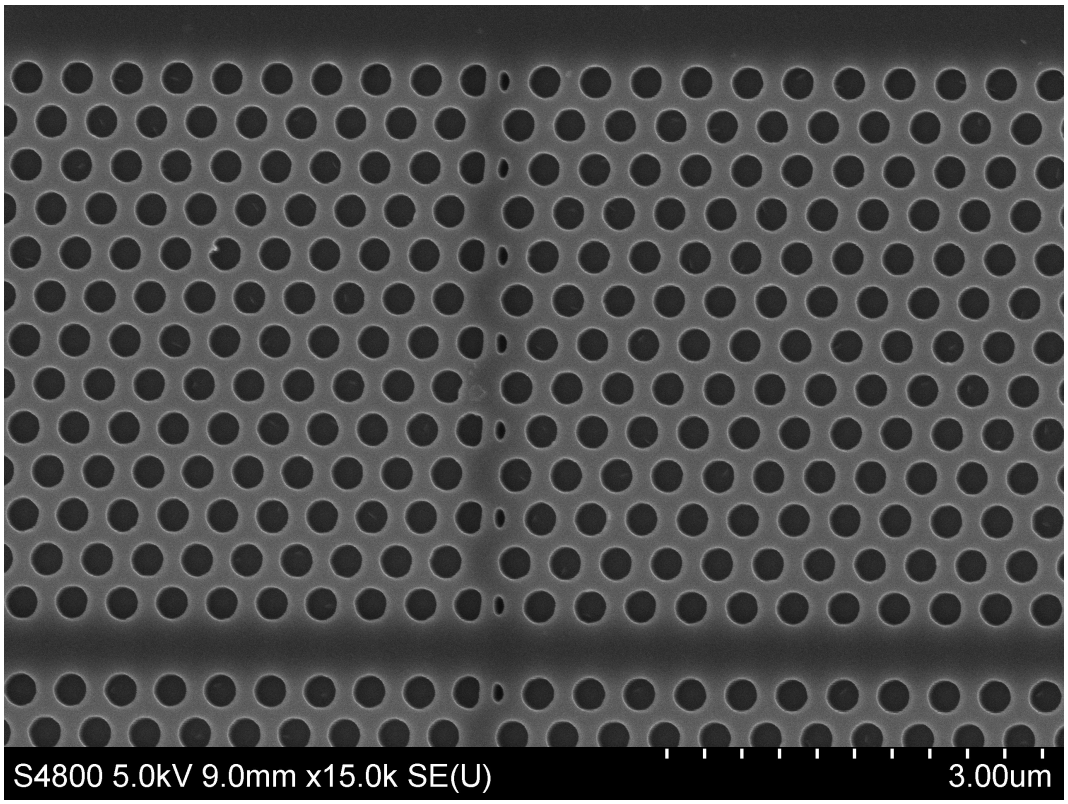

Figure 63: SEM images of a larger than usual stitching error. It is obvious that such a stitching error, and the resulting hole deformation, affects the optical properties of a PhC waveguide.

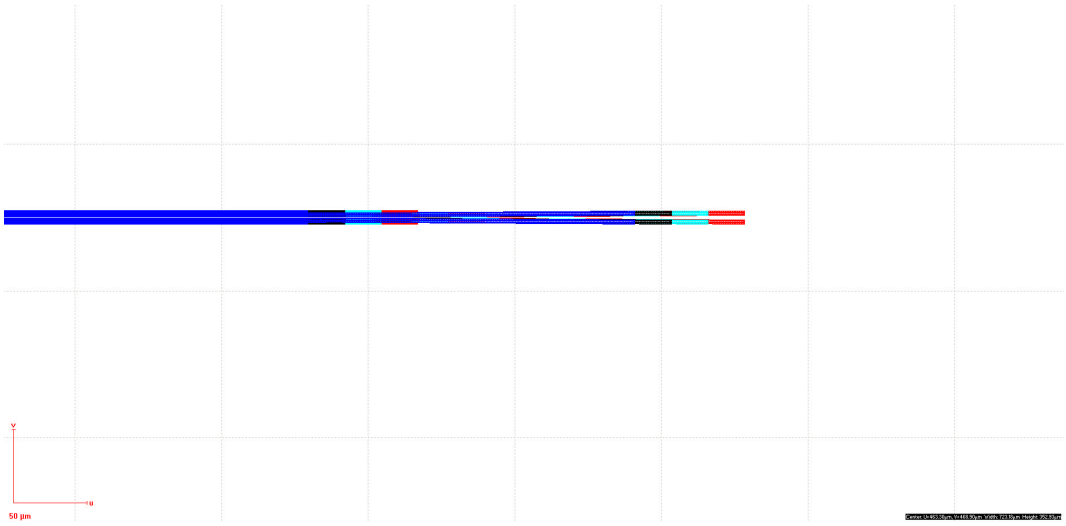

Figure 64: Image from a design pattern for a shot shifted waveguide. The pattern is repeated on 4 different layers (blue, black, light blue and red). On each layer the pattern is shifted $25\mu m$ to the right, appropriate for a $100\mu m$ writefield (grid shown as dotted lines). During e-beam exposure each layer will be treated as a separate object (giving it new writefields) and the starting coordinates will be shifted by $25\mu m$ to the left, to compensate the shift in the design file. The scale bar correspond to 50 μm

slow light effect, effectively prohibiting the fabrication of long slow light waveguides using electron beam writers with small writefields. The concept of shot shifting was invented to overcome this problem. Shot shifting was first investigated by Pagnotta et al. [45, 94], with the main focus lying on photonic wires. The basic principle of shot shifting is very simple, as shown in fig. 64. During this process, the design pattern is modified, such that it now consist of X copies of the original structure, each written with $1/X$ of the original exposure dose. These elements are then shifted by $100/X$ μm in the design file and the starting coordinates of each layer are shifted by the same amount, in the opposite direction, during electron beam exposure. Therefore, during the electron beam exposure all elements will be written at identical locations on the sample, but the writefield boundaries will be shifted, resulting in a reduction of the stitching error.

5.1.1 Exposure time

This shot shifting procedure involves a repeat exposure of the design pattern, although with a constant overall dose. We now need to consider the effect of this process on the total exposure time, as a large increase in exposure time would render shot shifting unusable for sample fabrication.

When calculating the exposure time of a pattern during electron beam lithography, several different factors need to be considered. These factors are called stage time, dwell time and settling time.

The stage time is the time taken to physically move the stage from one writefield to the next, and is fixed at 5 s in the RAITH system used during my project. The dwell time is the actual time that the resist is exposed. Therefore, it depends on the exposure dose of the pattern, as well as the current delivered in the electron beam. The settling time is the time that the beam is allowed to stabilise when unblanking, after moving from one object in the pattern to the next.

During shot shifting, the overall dwell time does not change, as each repeat element is only written with a fraction of the dose, and the total exposure dose for each object in the pattern is unchanged. However, both the total stage and settling time will increase, as each object will be addressed X times and the number of stage movements increases by the same factor of X. Therefore, shot shifting is always slower than a normal electron beam exposure. However, this effect is significantly different for photonic crystals and wires. A photonic wire consists of a few large objects that are exposed. Therefore, the dwell time is the main component of the exposure time, and the settling time is very small. The resultant increase in write time is low and justified by the improved fabrication quality. A PhC however consists of many small objects. Therefore, the settling time is the major factor determining the overall exposure time and shot shifting leads to an increased write time, as shown in table 2. The total write time could be reduced, by reducing the settling time. However, a small settling time, < 1 ms, can lead to hole shape distortions, particularly the so called "Pacman" effect, as shown in fig. 65.

5.1.2 Circular shot shifting

The Pacman effect occurs because a short settling time can lead to a reduced exposure dose for the starting point of the exposure of each object. Therefore, the concept of circular shot shifting was established. By rotating the circles in each layer, the starting point should be at different positions and the Pacman effect should average out. This effect should allow a reduction of the settling time, without any significant hole shape distortion, keeping the overall exposure time similar to a non shot shifted sample.

As the averaging of the Pacman effect could lead to a change in the fabricated hole

1mm long W1:		Times (mins: secs)		
Position (um)	Layer	Dwell	Settling	Total
X,Y	1	2:13	10:16	15:33
			No shot-shift:	**15:33**
X,Y	1	1:07	10:16	14:29
X-50,Y	2	1:07	10:16	14:29
			2 level shot-shift:	**28:58**
X,Y	1	0:33	10:16	14:04
X-25,Y	2	0:33	10:16	14:04
X-50,Y	3	0:33	10:16	14:04
X-75,Y	4	0:33	10:16	14:04
			4 level shot-shift:	**56:16**

Table 2: Total exposure time for a photonic crystal waveguide of different shot shifting levels. The exposure time increases significantly with each extra shot shifting level, as the settling time and not dwell time is the dominant component. Therefore standard shot shifting leads to an impractically large writing time penalty for PhC waveguides.

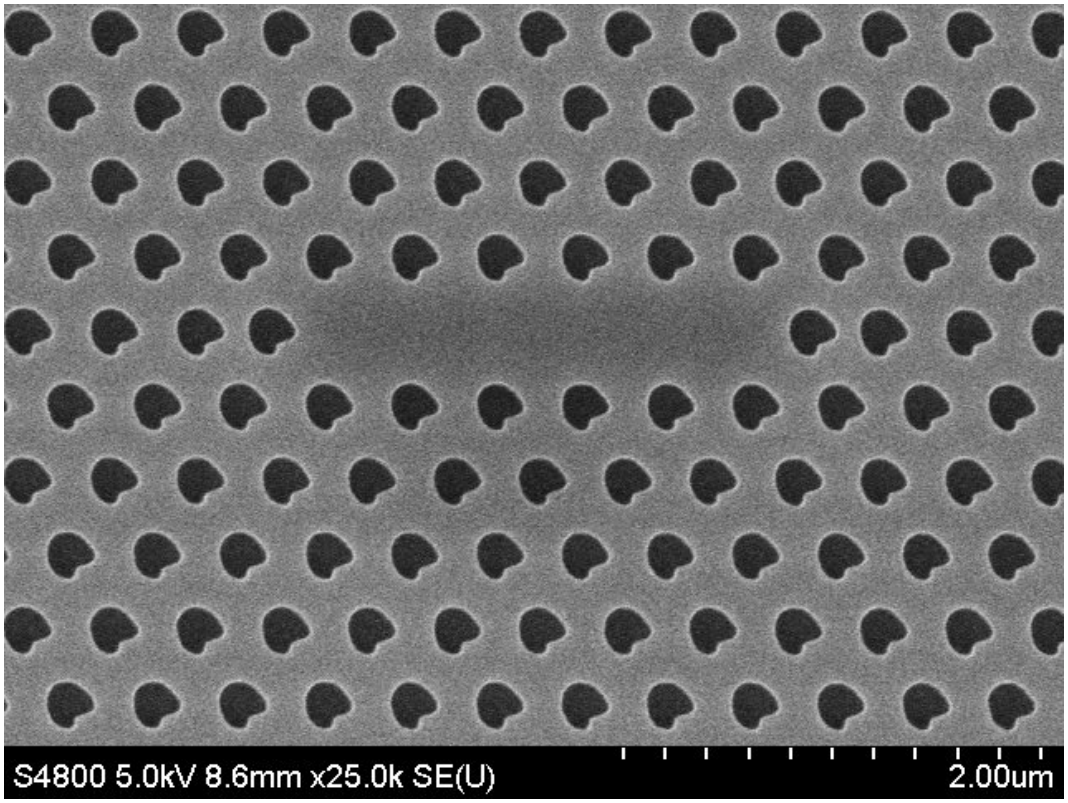

Figure 65: SEM image of a PhC cavity written with too low a settling time. The low settling time leads to a systematic distortion in the hole shape, known as the Pacman effect.

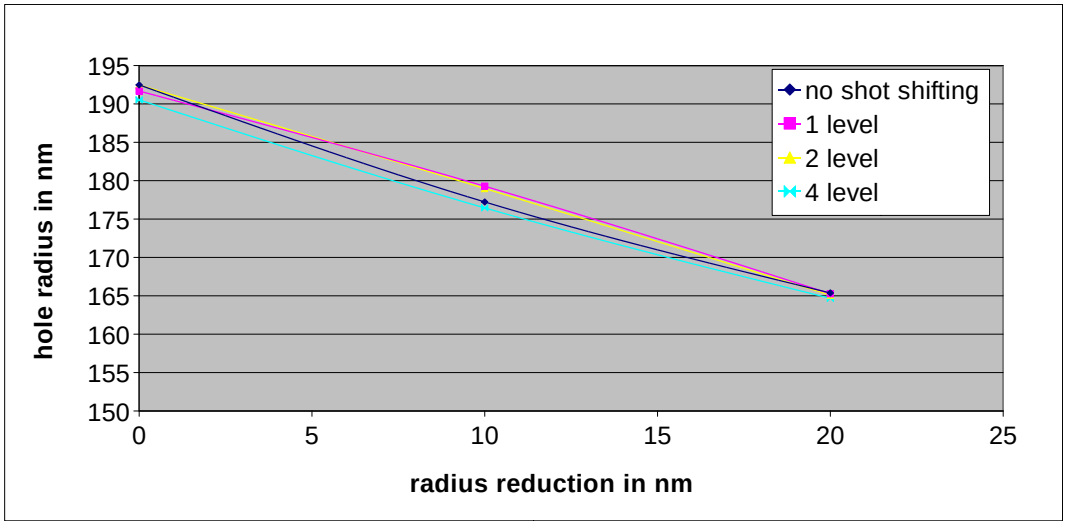

Figure 66: Measured hole radius for different shot shifting levels. The graph shows that the shot shifting has no significant effect on the hole radius and previous design routines can still be used.

radius, when compared to non shifted samples, initial calibration structures were fabricated and their hole size was measured. No significant difference in hole diameter was observed for holes with different shot shifting levels and no change to the fabrication procedure was necessary, as shown in fig. 66.

Following on from this initial test, further tests, on single writefields, aimed at investigating the hole shape, were conducted. During these tests, square and triangular lattice PhCs (no waveguides) were fabricated and imaged using a scanning electron microscope. As small differences in hole quality are not easily observable by eye, an automated analysis process, scripted for ImageJ [95], was developed:

- The SEM image is opened.
- Noise is removed to improve image quality
- A threshold of the brightness is used to create a mask image of the original
- Data, such as diameter, circularity and centre position is saved for each hole
- The original image is scanned again, this time replacing each hole with a best fit ellipse. An ellipse instead of a circle is used here, to account for possible drift during the SEM imaging process.
- The two images are subtracted from each other, leaving only those areas that are

present in a single image, i.e. the difference between the actual and the ideal hole shape.

- This defect area is recorded.

Images taken at different steps of this procedure are shown in fig. 67. The process is repeat on several SEM images for each set of shot shifting parameters, providing statistical information on the hole quality. The resulting data, shown in fig. 68, shows a reduction in defects for shot shifted holes, proving the principle of circular shot shifting and providing base parameters for further studies on shot shifted PhC.

5.1.3 Shot shifted PhC

After the initial promising results, shot shifted PhC waveguides and wire waveguides were fabricated. The shot shifting on wires successfully removed stitching errors, as shown in fig. 69. However, the fabricated photonic crystal waveguides showed significant hole shape distortion, see fig. 70, making optical measurement unfeasible. Unexpectedly, the change in hole shape observed for shot shifted waveguides was present for all settling times investigated and changed significantly along the same waveguide, with changes occurring at the writefield boundaries. Two possible sources for this distortion were identified. The first is the drift of the e-beam lithography system over time. Writing a single PhC waveguide of 1 mm takes around 15 min (fig. 2). As many waveguides are written in a single sample, the drift can lead to significant misalignment between the stage and the coordinate system by the time the second layer of a waveguide is exposed. While this explanation would lead to changes in the hole shape, it cannot explain the significant differences along a single waveguide. After all, the time difference between different layers is constant for each waveguide and the drift should not lead to abrupt changes, as it is a gradual process.

However, the second explanation can explain the abrupt changes and strong hole shape distortion. After correspondence with RAITH [96], it emerged that the stage movement to a new writefield is relative. I.e. instead of moving the stage to the coordinates of the new writefield, it is moved by $X\,\mu$m, where X is the writefield size. Therefore the stitching errors are additive. For example, if two subsequent stitching errors are 15 nm in the same direction, the third writefield will be shifted by 30 nm from the ideal position. Upon writing the second layer, the stage returns to the (ideal) starting coordinates. It is now imaginable that the stitching errors of the second run again add up to around 30nm, but this time in

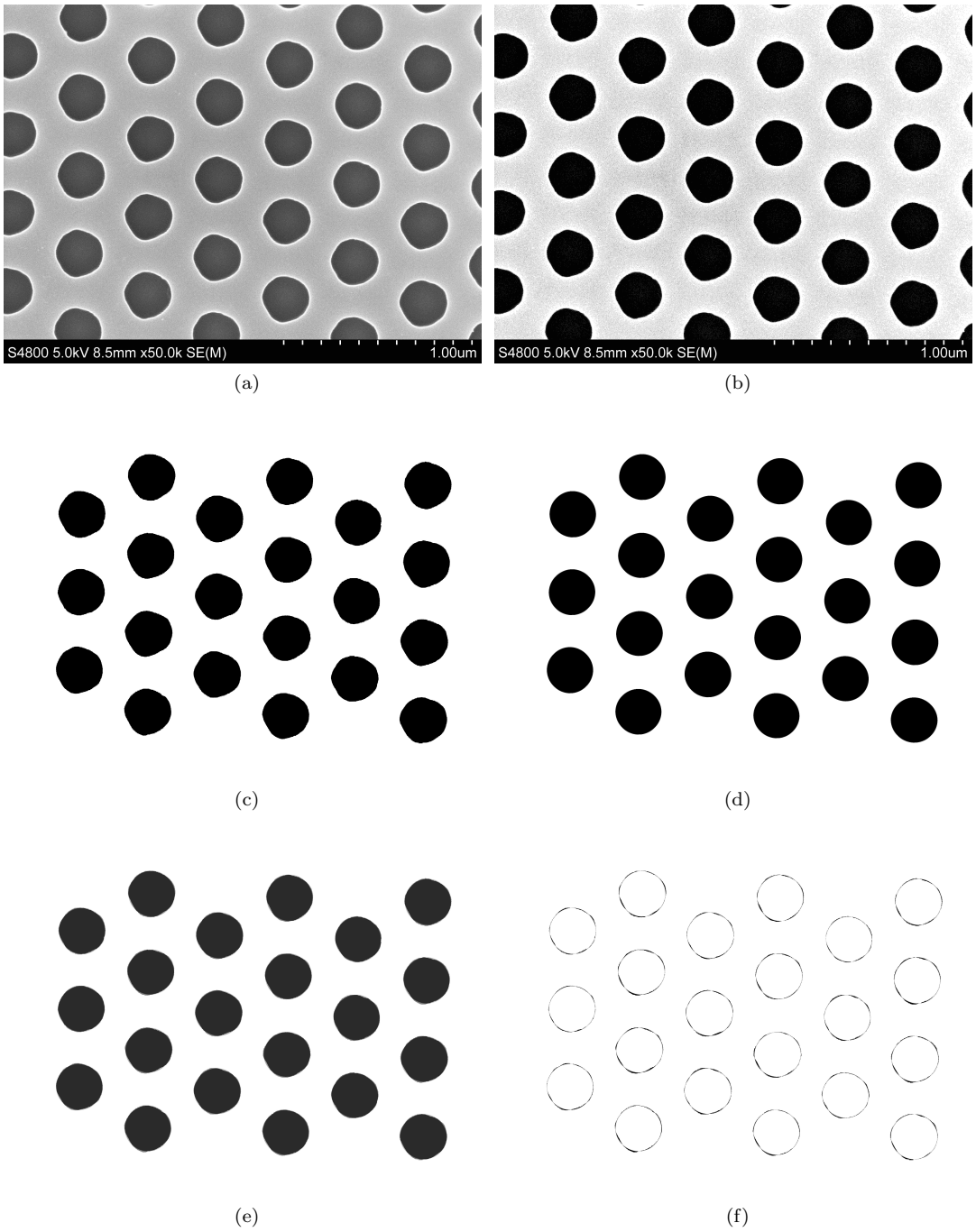

Figure 67: Images taken during the hole quality analysis. **a)** The original SEM image. **b)** A black and white image created from the SEM image, showing outliers (white points inside the hole area and dark points in between, due to noise on the SEM image. **c)** The actual hole area only, all other elements (including outliers) have been removed. **d)** Elliptical fit to the hole area. **e)** Addition of the two previous images (areas present in both pictures are black, while areas present in only one image (the deviations from the idea hole shape) are grey. **f)** Final image, only the areas present in a single image are retained, showing the deviation between the fabricated and ideal hole shape.

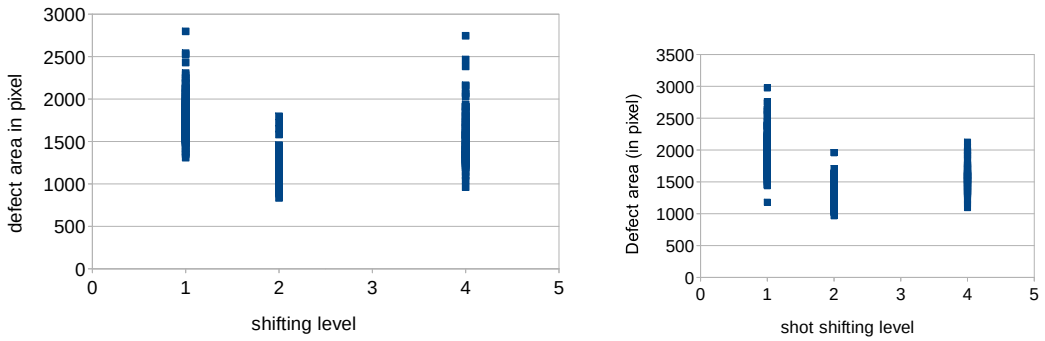

(a) (b)

Figure 68: Graphs showing the defect area for different shot shifting situations. In **a)** the total exposure time is constant, i.e. the shifted structures were written with half and a quarter of the original settling time respectively. **b)** Constant settling time across all structures. In this situation the shot shifted structures have a larger total exposure time. In both cases, the 2 level shot shifting shows a significant reduction in the hole disorder compared to a standard write (1 level only). 4 level shot shifting does not offer any further improvement. The large disorder for the 4 level shot shifting in **a)** is attributed to a very small settling time, which is not fully compensated by the shot shifting.

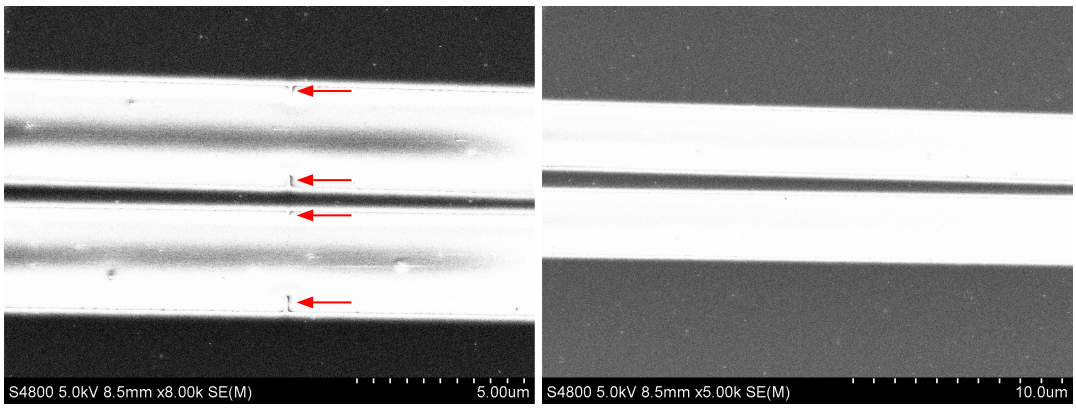

(a) (b)

Figure 69: **a)** SEM image of the taper region, with small stitching error, as indicated by the red arrows. **b)** SEM image of the same position on a different, shot shifted taper on the same sample. No stitching error is visible in this case.

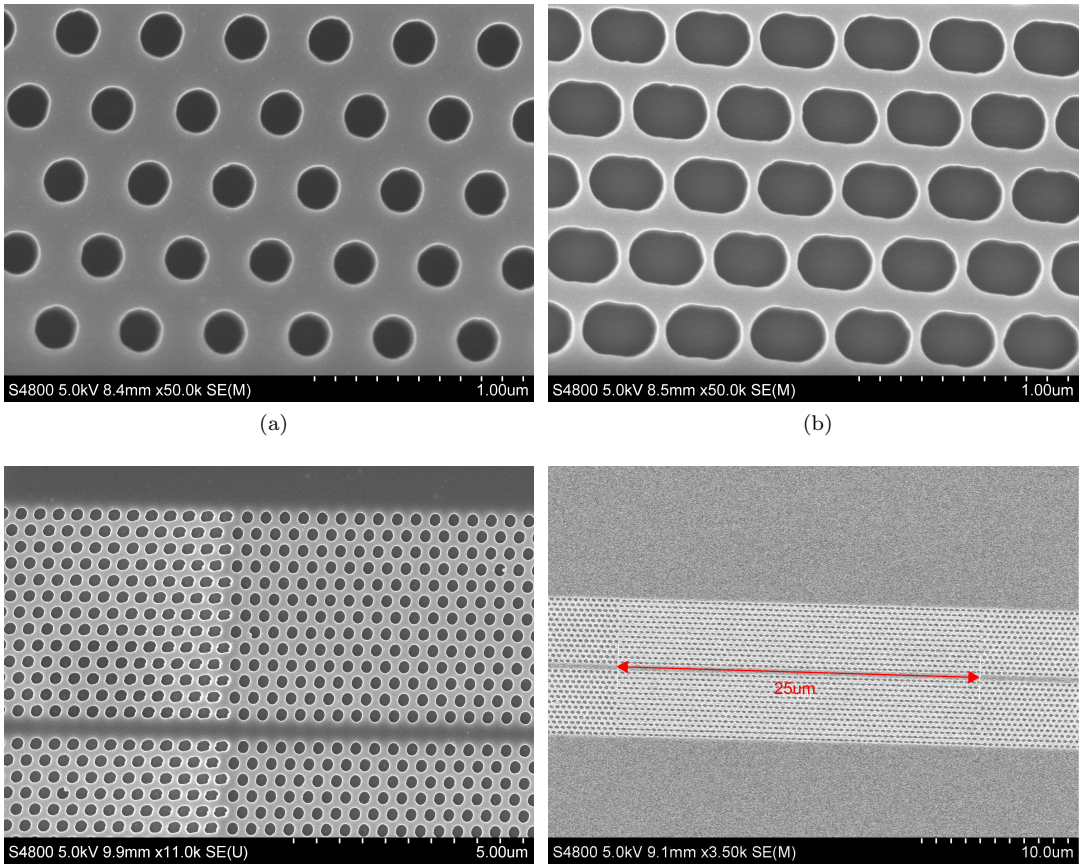

(a) (b)

(c) (d)

Figure 70: SEM images of PhC waveguides. **a)** Non shot shifted PhC, showing nice circular holes. **b)** 2 level shot shifting on the same sample, with same total exposure dose, showing a clear elongation of the holes along the waveguide. **c)** A rapid change in hole shape for a 2 level shot shifted sample. This change occurs at the interface between 2 WF (for one of the shot shifting levels). **d)** 4 level shot shifting sample, showing that the hole shape changes in intervals identical to the shot shifting shift. I.e. for every combination of writefields (from different levels), the cumulative stitching error changes, resulting in a different variation of the hole shape, making these devices unsuitable for applications.

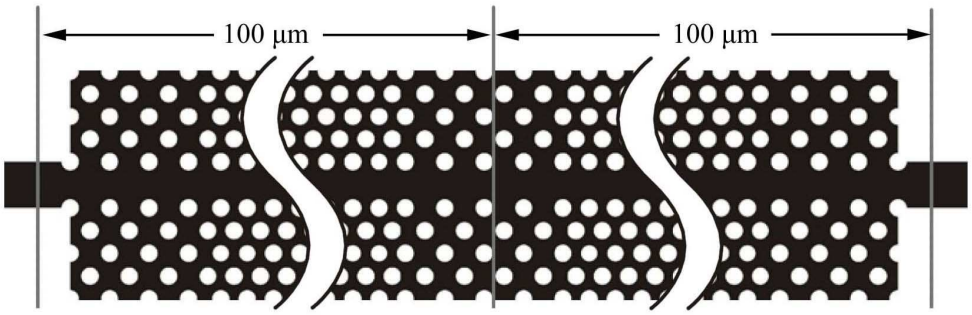

Figure 71: Sketch showing the slow-fast-slow light region around the stitching error [97]. The fast light ($n_g = 5$) region is based on the mode conversion interface used to couple light into, and out of, the PhC. The stitching error (vertical line) is placed between PhC holes, to reduce its impact even further.

the opposite direction. Therefore the overall misalignment between the two layers is now 60 nm, a significant proportion of the typical hole diameter ($200 - 280$ nm). This explanation also correctly predicts that the effect should be worse the more repeat layers are written for each waveguide and can cope with the strong differences between adjacent writefields.

Both explanations predict that the shot shifting of wires is not affected, as there are no small features present that would be affected by a misalignment on this level.

5.1.4 Coupling elements

As the available control mechanisms of the e-beam system do not allow a successful implementation of shot shifting for PhC waveguides, an alternative solution was investigated. Initially, this solution consisted of short photonic wire section, coupled to the PhC waveguide through standard mode conversion interfaces. The design was subsequently simplified by J. Li, who realised that the wire section was not necessary. Instead, the two fast light sections of the mode conversion interface are merged into a single fast light section, as shown in fig. 71. In this section, the lattice period is stretched compared to the normal waveguide regions. If the period is stretched by a suitable distance, the writefield boundary can be placed between holes. Therefore stitching errors only lead to a change in the lattice period, and not the hole shape. Furthermore, as the group index of the fast light region is constant across the operating wavelength band, the scattering from stitching errors is not amplified by the the slow light effect, leading to significant reductions in the slow light propagation loss, as shown in fig. 73.

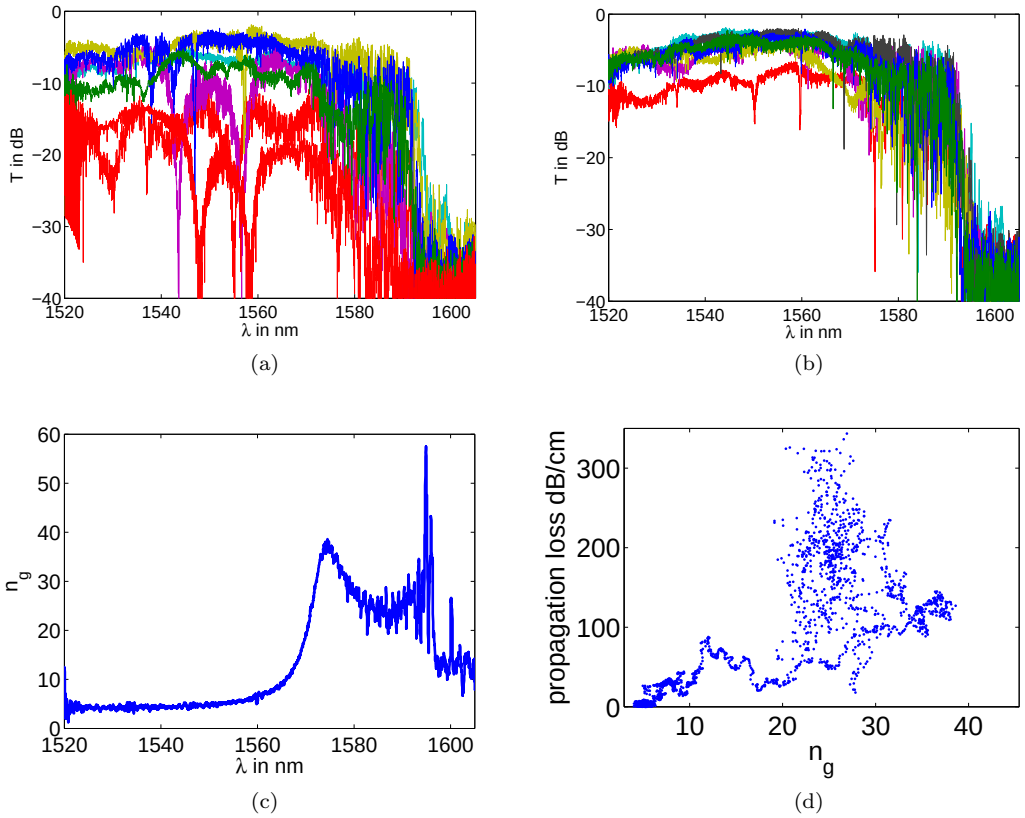

Figure 72: **a)** Transmission through various overengineered PhC waveguides without sfs interfaces. **b)** Same waveguide design, this time with sfs interfaces. All waveguides in **a)** and **b)** span two writefields. For waveguides with sfs couplers, the stitching error was placed between air holes, which is not possible in the standard lattice, leading to better transmission with lower dips due to the stitching errors. **c)** Measured group index curve for this waveguide design. **d)** Loss measurement for the waveguides with sfs interfaces. The large spread of data points in the high loss region is due to multiple scattering, as explained in section 3.4.

Figs. 72 & 73 show data for two different sets of slow light waveguides, both containing copies fabricated with and without the slow-fast-slow (sfs) interfaces described above. The first (fig. 72) is an example of a overengineered waveguide. On this sample large stitching errors were present, leading to significant distortions of the transmission spectra of the standard PhC. These dips, resembling cavity resonances, are not as pronounced in the devices containing sfs interfaces. As the stitching error is now placed between holes, its effect is reduced significantly, leading to smoother transmission and slow light curves. This improvement allowed a successful loss measurement, using very short waveguides ($30 - 400\,\mu$m long), for the devices with interfaces. This represents the first ever propagation loss measurement on overengineered waveguides.

J. Li measured a different engineered waveguide design (fig. 73), optimised to have a large slow light and low loss bandwidth at $n_g = 60$, making it suitable for FWM experiments (the topic of Dr. Li's research). The measured propagation loss for the waveguides with sfs regions was compared to theoretical predictions. The results show good agreement between the calculated and measured propagation loss, without the use of fitting parameters, i.e. assuming the same roughness as in section 4, where a different e-beam lithography system, with higher acceleration voltage (100 kV vs 30 kV) and a larger writefield (1200 μm vs 100 μm) was used. The blue circles in fig. 73 show the propagation loss of waveguides without the sfs regions, red dots represent the measured propagation loss for waveguides with sfs regions, and the solid black line is the calculated propagation loss. This graph reveals several interesting points about the impact of sfs regions on the propagation loss. The shape of the curve described by the blue circles shows very good agreement with the calculated curve, although the measured propagation loss is generally a factor of 2 higher than the calculated values. As the calculated data includes one stitching error every 1200 μm and the measured blue circles one every 100 μm, the total scattering from these stitching errors will be significantly higher. In the fast light region, this accounts for about $6 - 9$ dB/cm (over half of the measured propagation loss). This additional propagation loss is amplified further throughout the complete operating regime. For devices with sfs couplers, the propagation loss in the fast light region is higher than for both the standard waveguides and simulated waveguides, while the propagation loss in the slow light region is reduced significantly. In the fast light region, the difference in propagation loss caused by a stitching error in a sfs region compared to a normal waveguide is very small. On the other hand, the sfs region includes two additional interfaces between PhC with slightly different lattices (per writefield), leading to an increase in the total propagation loss. However, as shown in section 2.4.1, the transmission of the slow-fast mode interfaces is nearly group index independent. Therefore, in the slow light region, the propagation loss caused by each PhC lattice interface is the same as in the fast light region. As the stitching error is still contained in the fast light region, the total scattering loss of each sfs region is independent of the group index, leading to a significant reduction in the total propagation loss in the slow light region. This reduction is larger compared to devices fabricated with a 100 μm writefield (measured), than compared to devices with a 1200 μm writefield (simulated). This measurement is a remarkable result, not only because it allows the fabrication of low loss PhC waveguides spanning multiple

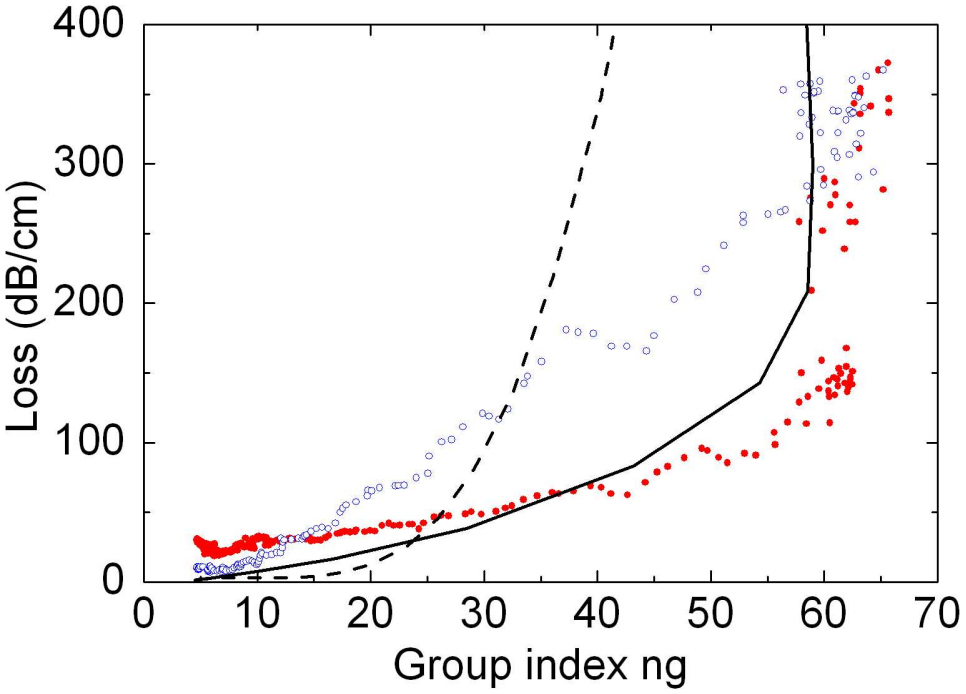

Figure 73: Graph showing experimental and theoretical propagation loss vs group index for loss engineered waveguides [97]. Blue circles are for waveguides without sfs interfaces. Red dots for the same waveguide design, but with sfs interfaces. The solid black line represents the predicted propagation loss for this design, with no fitting parameters. Black dashed line is for a W1 waveguide. A comparison of the experimental data shows that the introduction of sfs interfaces reduces the propagation loss by more than 150 dB/cm in the slow light region. Similarly a comparison with the W1 waveguide reveals an order of magnitude reduction in propagation loss due to loss engineering.

writefields, but also as it is the first time that the propagation loss of a PhC waveguide was accurately predicted. The black curve in fig. 73 is from data calculated before the sample fabrication, and the discrepancy between the two curves can be explained by the group index independent loss of the sfs interfaces.

5.2 Reducing surface roughness

The surface roughness, on etched sidewalls, is expected to be a major contributor to the extrinsic scattering, leading to propagation loss. Therefore, the fabrication of photonic crystals with lower sidewall roughness should lead to a reduction in propagation loss. Furthermore, such a study should also provide important information on the relative importance of the different disorder types present inside a photonic crystal. During the initial reduction in PhC waveguide loss, from the years 2000-2007, the reduction in surface roughness was achieved through improved etch recipes and better e-beam lithography. However, since these fabrication techniques have now matured, further reduction of propagation loss through better etch recipes is not easily feasible. Instead, alternative post-processing methods are of interest. Here, we have a wish list of properties that should be satisfied by such processes, to simplify integration into the current fabrication flow. Any post-processing step for the reduction of surface roughness in silicon PhC should have:

- a high efficiency;
- CMOS compatibility;
- repeatability and high yield;
- chemical and mechanical stability of treated samples.

If the above conditions are satisfied, other components of the process flow do not have to be adjusted, allowing easy integration of the new process into the fabrication flow. In this thesis, I present three post processing methods that I have investigated. These methods are a silicon annealing, a hydrogen plasma polishing/smoothing procedure and a controlled oxidation method.

5.2.1 Silicon Annealing

If silicon is heated to high temperatures, $> 1000°C$, in an oxygen free atmosphere, the silicon atoms regain limited mobility [98]. As the atoms on the surface can now move, they

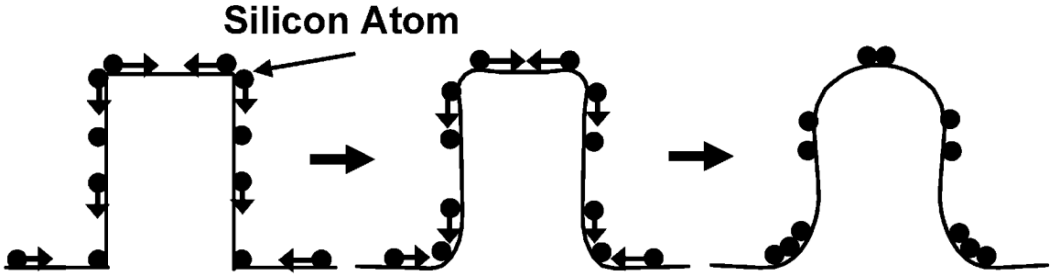

(a)

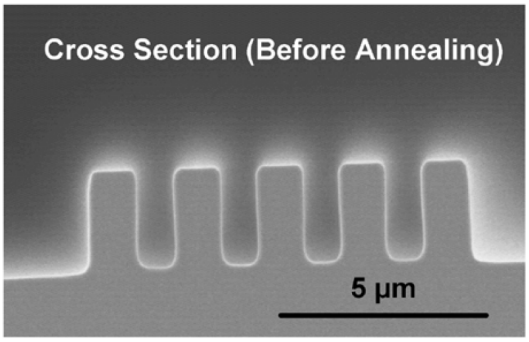

(b)

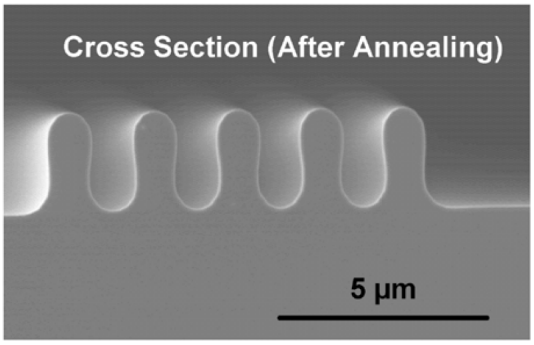

(c)

Figure 74: a) Sketch of silicon reflow. When heated in an inert atmosphere, the silicon atoms become mobile and rearrange such that the surface energy is minimised, thereby rounding of corners and reducing surface roughness. b) and c) are SEM images of grating lines in bulk silicon before (b) and after annealing in a hydrogen atmosphere (1100°C and 10 torr for 5 min) Figures taken from reference [98] © 2006 IEEE

will rearrange, reducing the surface tension at the silicon/gas interface, see fig. 74. Such a re-flow leads to rounded edges, and should lead to a reduction of the surface roughness on etched sidewalls. In the past, this process had been demonstrated for photonic wires, using both H_2 and Ar at low pressures [98, 99, 100]. In this section, I will present the work undertaken on studying annealed photonic crystal waveguides. During my project, all annealing was undertaken in a Carbolite furnace, as shown in fig. 75. In this set-up, the sample is placed inside a quartz tube, which has the chosen gas flowing through it. The furnace is then heated to the operating temperature, with the sample outside of the furnace. Once the furnace temperature has stabilised, the furnace is moved along the tube, such that the sample is positioned in the centre of the furnace. After the annealing time is over, the furnace is shifted back to its heating/cooling position and turned off. Once the temperature of the sample has dropped sufficiently, to avoid oxidation upon contact with air, the quartz tube is opened and the sample removed from the tube. The gas outflow from the quartz tube is connected to a bubbler, to avoid reverse flow of the ambient atmosphere.

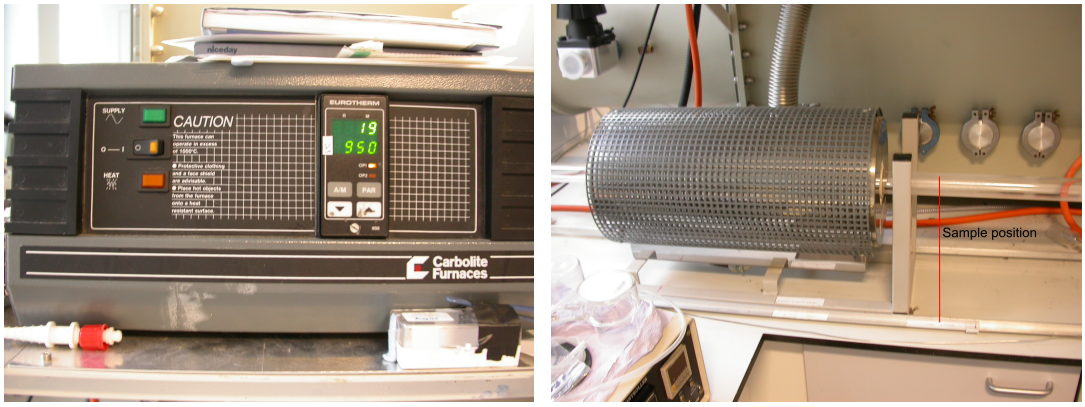

(a) (b)

Figure 75: Photos showing a) the furnace control unit and b) the furnace itself. In this picture the furnace is shown in its heating/cooling position and the red line indicates the sample position. During annealing the furnace is shifted to the right, such that the sample is in the centre of the furnace.

Hydrogen annealing As the first demonstration of annealed silicon structures used a hydrogen atmosphere, a similar atmosphere was chosen as a starting point. As the gas was heated to over 1000°C, a mixture of hydrogen and argon was used instead of pure hydrogen, as a safety measure. Furthermore, before heating the furnace, the quartz tube was flushed with nitrogen, to avoid the formation of a hydrogen/oxygen mixture. The same safety precaution was taken before opening the quartz tube, after the annealing procedure. The inclusion of argon in addition to hydrogen should not affect the annealing process significantly, as annealing in an argon atmosphere has been demonstrated [100]. Initially, a run with different hydrogen annealing times was conducted and the results were assessed using SEM images, to find suitable process parameters before taking optical measurements of treated samples. However, the annealed samples did not show any reduction in surface roughness. Instead, the growth of nanowires was observed, as shown in fig. 76. As the origin of these nanowires was not at first understood, an energy-dispersive X-ray spectroscoy (EDX) measurement was taken, to investigate the chemical composition of the nanowires. This measurement revealed the presence of Si, O, and C. As these samples were still supported by the buried oxide, and every sample will acquire a degree of contamination (including C), the presence of all these materials is to be expected on such a sample and therefore very little information about the nanowires could be gathered from this experiment. Hydrogen cannot be detected by EDX, due to its low atomic weight, and therefore the presence of hydrogen in the nanowires cannot be excluded. Additionally, further investigation revealed

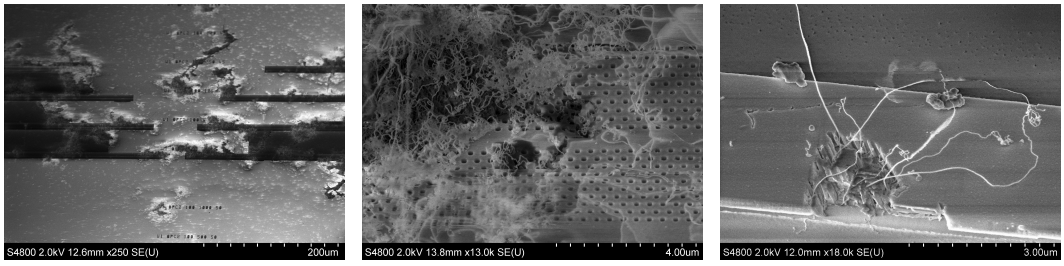

(a) (b) (c)

Figure 76: SEM images of nanowires formed during H_2 annealing. **a)** A wide area view of a sample shows the extensive damage, which was recognisable using the naked eye. **b)** A zoomed in view a PhC on the sample from a, showing that optical transmission through this sample is not possible due to the damage sustained. Sample was annealed at 1150°C for 2 hours in a hydrogen flow. **c)** SEM image of a sample annealed in static hydrogen. Nanowires are still formed, however much more slowly than in a moving atmosphere.

a clear dependence of the nanowire formation on both annealing time and hydrogen flow conditions. Annealing for shorter times, or in a static hydrogen atmosphere, led to fewer nanowires forming. Therefore, we can assume that the presence of hydrogen is crucial to this process. A literature search revealed that Si nanowires can be grown through chemical vapour deposition of SiH_4 with a Au catalyst [101, 102]. Furthermore, in this process, the nanowire diameter is determined by the size of the Au catalyst nanoparticles [101], see fig. 77. The nanowires formed during our annealing were only a few nm in diameter, indicating that very small gold particles must be present on the samples.

Nitrogen annealing As the nanowire formation during the hydrogen annealing process is suspected to be due to the presence of both Au and H_2, annealing of silicon in a nitrogen atmosphere was investigated. In contrast to the hydrogen annealing, where times between $15 - 120$ min were used, much longer annealing times were required for the nitrogen atmosphere. After 15-18 hours, at 1150°C, a significant smoothing of etched features was observed, as shown in fig. 78. From fig. 78 d), we can see that after annealing, the PhC has a significantly smaller hole diameter than before treatment. Therefore, a calibration of the design and fabrication process might be required, as this reduction in hole diameter is expected to lead to a significant change in the dispersion, and group index, curve of the PhC. However, even the change from hydrogen to nitrogen did not completely eliminate the presence of nanowires, although the growth rate was significantly lower (see fig. 79).

At this point, we should consider the possible sources of Au nanoparticles. Au diffuses easily into silicon and is therefore not a CMOS compatible metal. As SOITEC, the supplier of

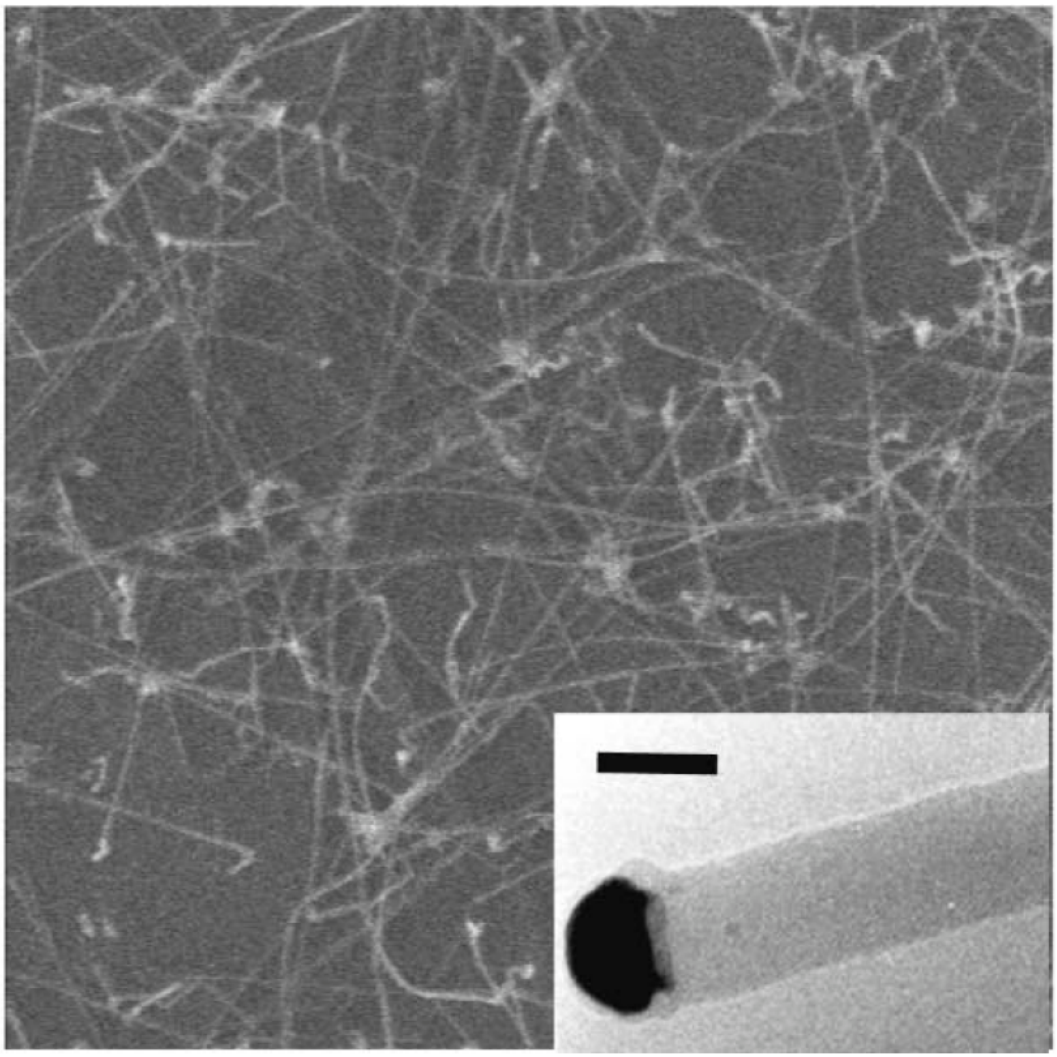

Figure 77: SEM image showing Si nanowires grown on Au nanoparticles, through CVD. The inset shows that the diameter of the Si nanowire is dependent on the size of the Au nanoparticle (show in black). The scale bar in the inset is 20 nm. Figure taken from reference [101]

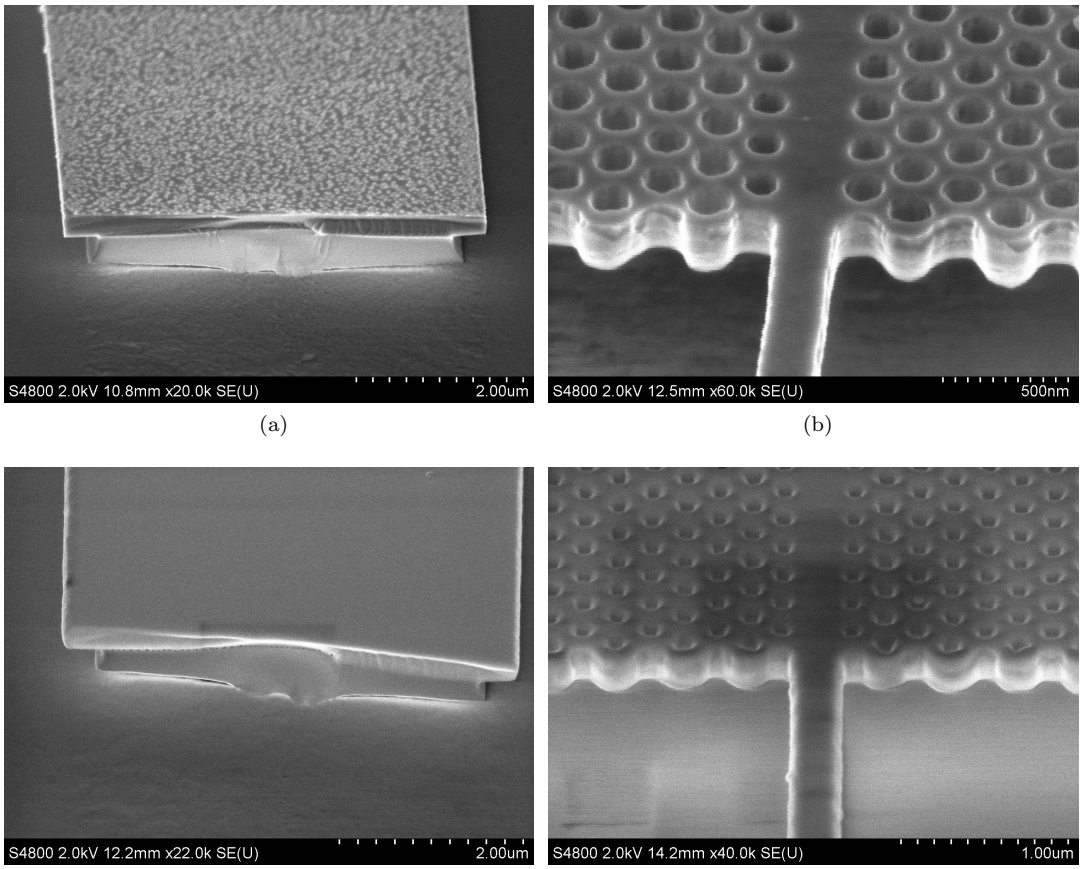

Figure 78: SEM images showing **a)** an access waveguide and **b)** a PhC before annealing in N_2. **c)** and **d)** show the same waveguide and PhC after annealing in nitrogen, for 17 hours at 1150°C. A clear smoothing of all corners, and reduction in sidewall roughness is observed, demonstrating that a hydrogen free atmosphere can achieve the conditions necessary for silicon reflow.

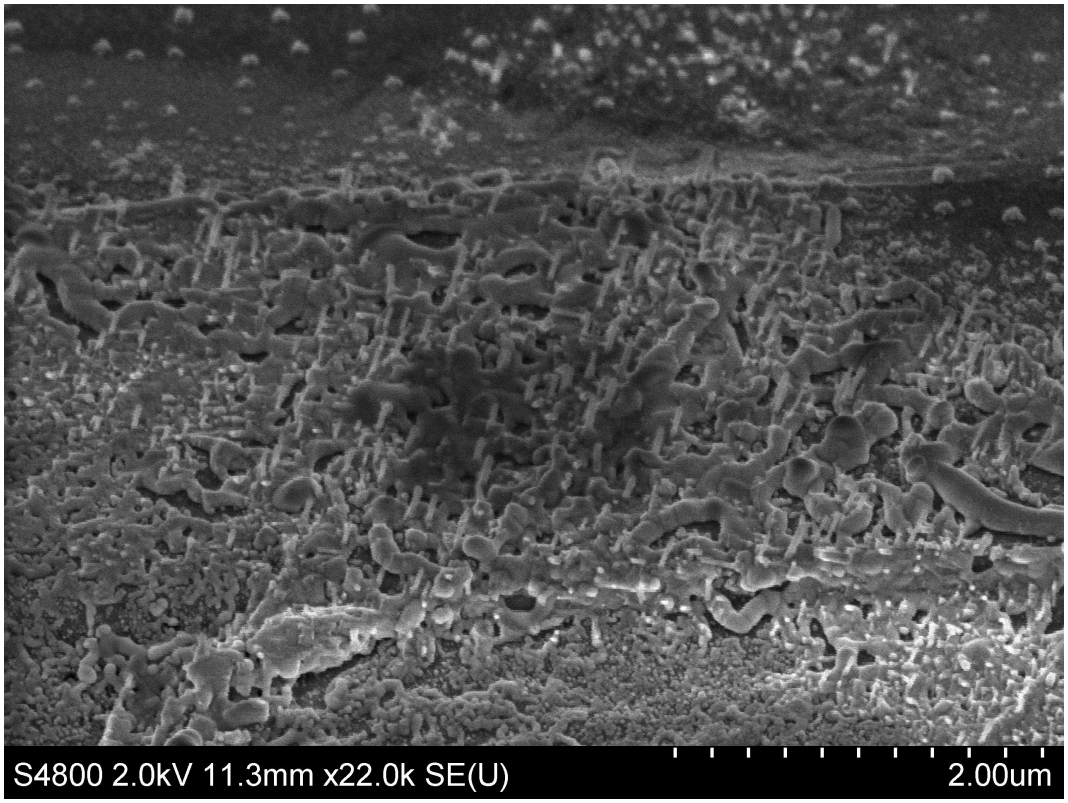

Figure 79: SEM image of nanowires formed during annealing in a N_2 atmosphere. The severely reduced length, and the lower occurrence, of nanowires formed during annealing in nitrogen indicates a suppression of the nanowire growth, compared to annealing in hydrogen. Sample was annealed at 1100°C for 15 hours.

our wafers, is supplying large quantities of wafers to the CMOS industry, the possibility of Au being present in the silicon wafers, as supplied by SOITEC, is very remote. This conclusion is supported by the fact that nanowire growth was observed for samples fabricated from different silicon wafers, which were supplied over a period of several years. Therefore, the Au contamination must be introduced during subsequent sample processing steps. Here, the potential sources could be contaminated tweezers, beakers, contaminants in the quartz tube or other processing equipment, such as the RIE. Before, and while, the annealing experiments were conducted, the quartz tube was also used for the annealing of metal contacts, opening the possibility of contamination being introduced during this step. Furthermore, Au liftoff could have been performed in the same beakers that were later used for cleaning of annealing samples. To eliminate these source of contamination, new equipment was used for subsequent annealing steps. This equipment included a new quartz tube, sample holder, tweezers and beakers. As shown in fig. 80, the old tube shows significant discolouration compared to the new tube, indicating that it was contaminated during previous processes.

Samples annealed with the new equipment did show a further reduction in nanowire formation, however other defects, especially cracks in the Si layer, were still present in these samples, as shown in fig. 81. Furthermore, no repeatable process conditions, leading to a similar annealing effect for repeat experiments, could be found. As it stands, the annealing process shows promise, however the high defect formation and low repeatability leads to a very small yield, eliminating it from the possible fabrication steps that could be used for low loss waveguide fabrication.

The low repeatability is most likely due to the low process control. In general, annealing processes are conducted in a rapid thermal annealer (RTA), offering precise control over the temperature and gas pressure, as well as stable annealing conditions over the complete process time. In the set-up used for this work, this level of control is not present. It is not possible to guarantee a steady gas flow over a 15 hour period, using only a pin valve (no mass flow meter is present in the set-up), nor can the pressure in this set-up be reduced below atmospheric level. Therefore, a more precise control over the fabrication conditions is required to successfully use the smoothing of etched sidewalls due to silicon annealing.

Figure 80: Photograph showing the old (top) and new (bottom) furnace tube. The image shows the region where the sample is placed during annealing. The old tube is significantly dirtier than the new tube, providing a possible source of contaminants during the annealing process.

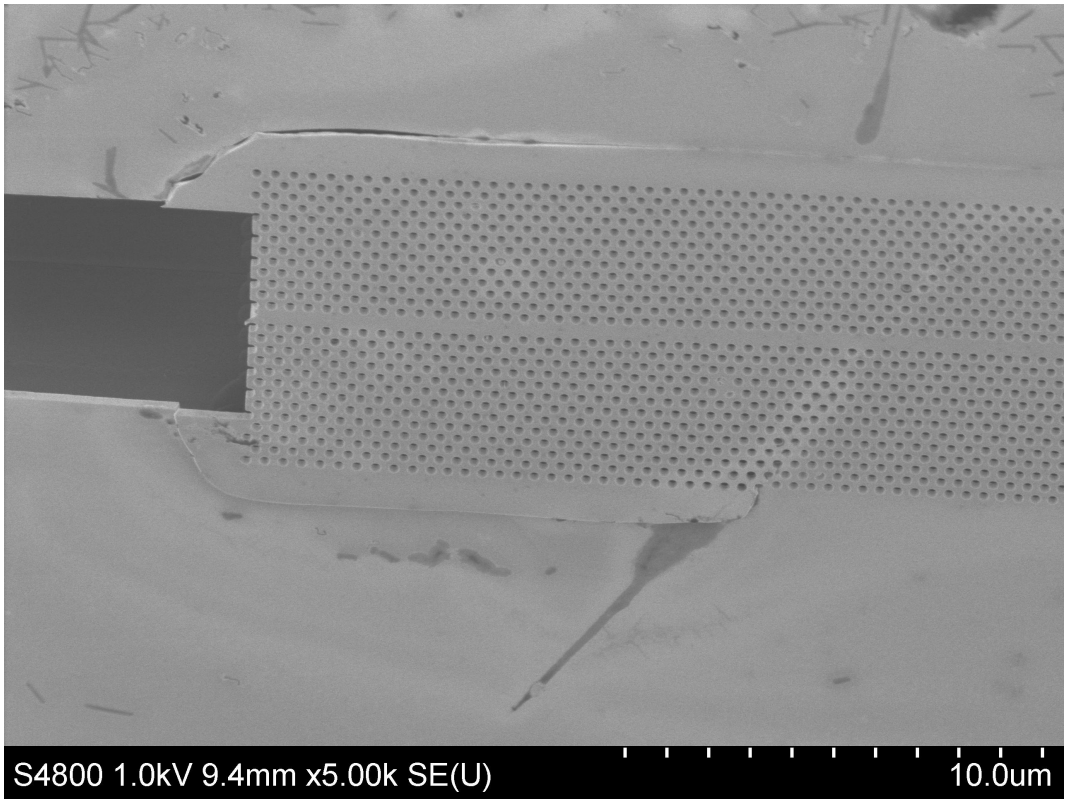

Figure 81: SEM image showing a PhC after annealing in nitrogen. The access waveguide has collapsed and the PhC membrane itself is breaking off from the sample.

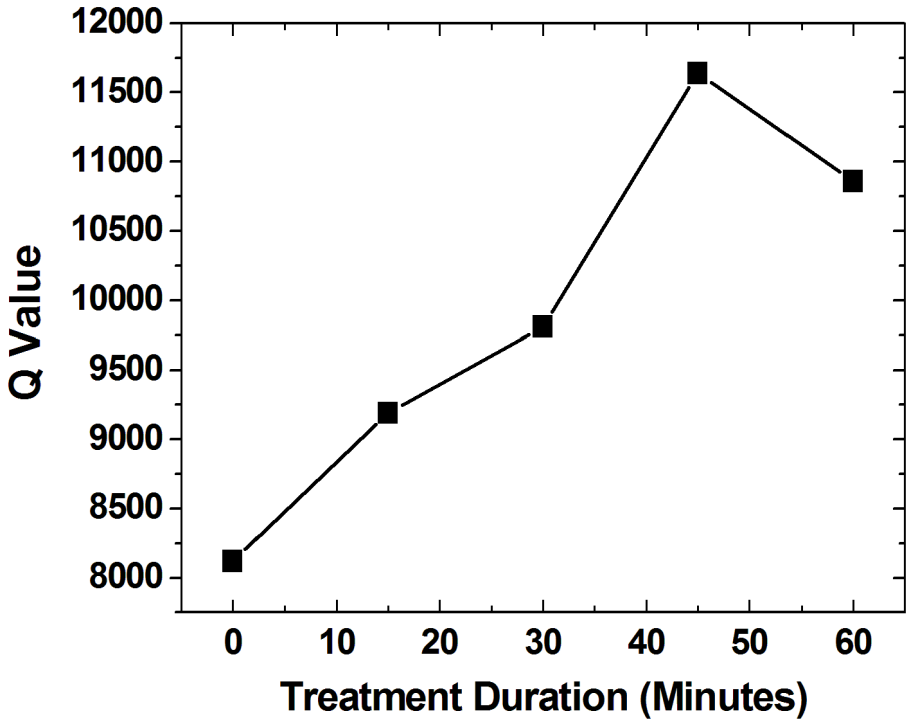

Figure 82: Graph showing cavity Q-factor against H_2 plasma treatment time for PhC cavities. The increased Q-factor is attributed to a reduction in sidewall roughness during the plasma treatment. Graph courtesy of A. Shakoor.

5.2.2 Hydrogen plasma smoothing

As the annealing methods discussed in the previous section did not lead to repeatable fabrication processes, alternative methods for the roughness reduction were investigated. The first method is the treatment of photonic crystal waveguides in a hydrogen plasma. It was first observed by A. Shakoor that the quality factor of PhC cavities can be increased, through an exposure to a hydrogen plasma, as shown in fig. 82. As the Q-factor of a cavity is inversely linked to the light leaking from it, an increased cavity Q-factor should lead to a reduced propagation loss, for waveguides treated in a similar fashion.

For photonic crystal cavities, the hydrogen plasma treatment is the last step in the process flow, however this same process order is not possible for PhC waveguides. Due to the increased membrane area, PhC waveguides are not as mechanically stable, resulting in collapse and subsequent removal of the waveguide area during hydrogen plasma exposure, as shown in fig. 83. Therefore, PhC waveguide samples have to be exposed to the hydrogen

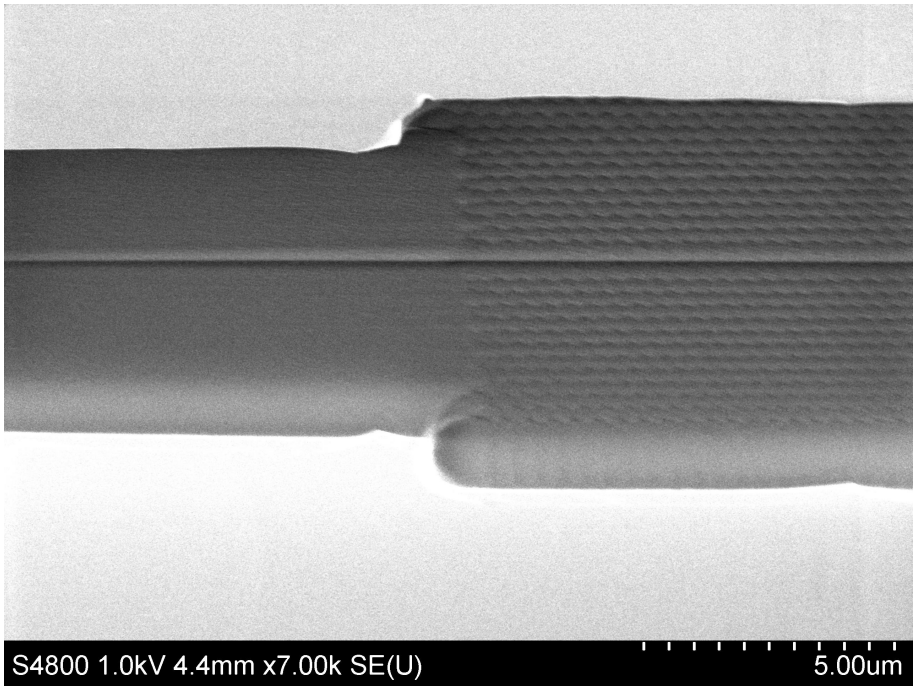

Figure 83: SEM image of a PhC sample after H_2 plasma treatment. The PhC membrane is not very mechanically stable. Therefore it collapsed during the plasma treatment and has moved away from the sample, most likely when flooding the RIE chamber with N_2. Therefore plasma treatment of PhC samples is only possible before the HF etch of the buried oxide.

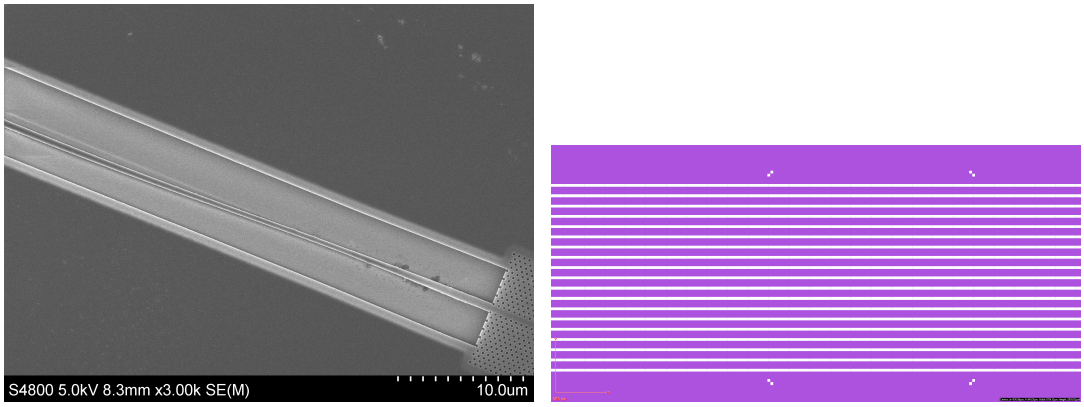

(a) (b)

Figure 84: **a)** SEM image of a H_2 plasma treated waveguide after HF etching. The etch mask lifted off from the sample, leading to a complete underetch of the access waveguide taper and a mechanically unstable sample. The sample was only etched for 10min instead of the usual $15 - 20$ min to avoid a complete collapse of the access waveguide. **b)** Outline of the mask used for selective H_2 treatment. Only the $40\,\mu$m wide strips (shown in white), at $100\,\mu$m intervals, are exposed to the plasma. The green region is protected by a polymer resist. The resulting sample has enough untreated silicon between waveguides to ensure adhesion of the polymer mask used during the HF etch.

plasma before the HF underetch. However, the resists used as mask during the HF etch step do not bond to the surface of the hydrogen plasma treated silicon. Instead, if inserted into the HF solution, the resist layer lifts off and the access waveguide is underetched, making it mechanically unstable, as shown in fig. 84. However, this problem can be resolved by using a polymer mask to treat the waveguide regions only, protecting the bulk silicon between them (see fig. 84). Therefore, after plasma treatment, the resist still adheres to the untreated silicon between waveguides, allowing for a well defined HF underetch using the standard process recipe. Furthermore, a similar polymer mask can be used to protect selected areas, such as metal contacts or doped regions, during hydrogen plasma treatment.

Initial measurements on plasma treated waveguides were very promising, resulting in a strong reduction of propagation loss for photonic wires, and a shift in the operating region for photonic crystal waveguides, as shown in fig. 85. On these samples, no polymer mask was used for the plasma treatment and therefore it was not possible to completely isolate the PhC waveguides from the underlying oxide, leading to a reduction of the group index that could be observed. The shift in the operating region of the photonic crystal is due to the removal of silicon during the plasma treatment, leading to an increase in the hole radius and an associated shift of the group index curve to shorter wavelength. This shift was confirmed through measurements on dispersion engineered waveguides, where the treated waveguides

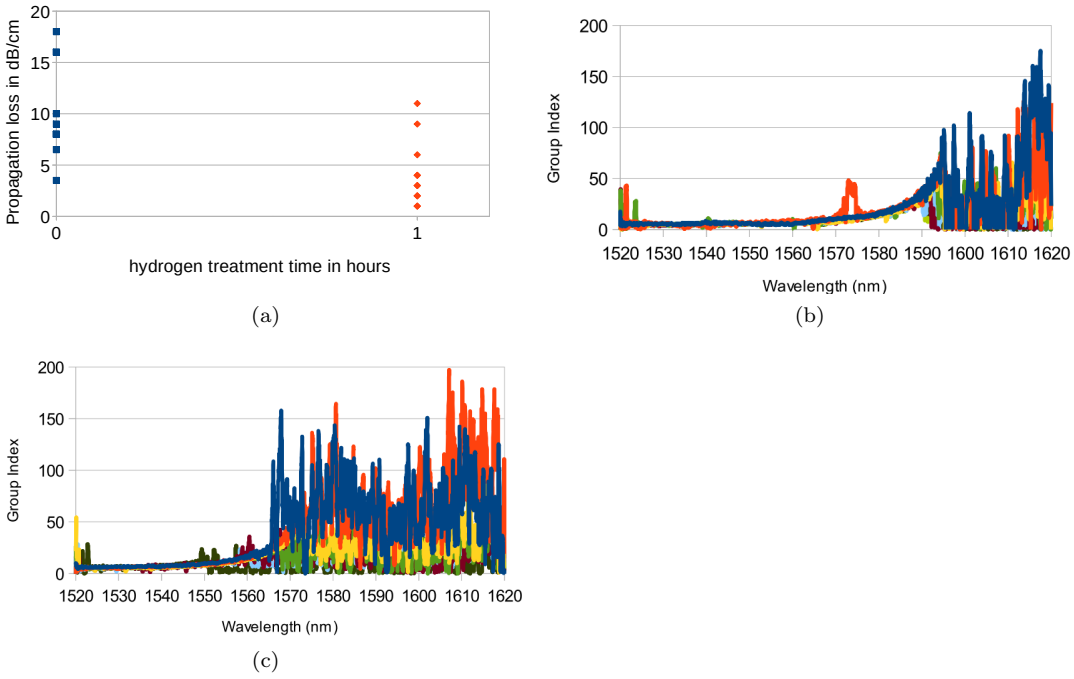

Figure 85: Graphs showing initial measurements on H_2 plasma treated samples. a) Photonic wire propagation loss before (blue squares) and after (red diamonds) plasma treatment. b) Slow light curve of W1 waveguides treated for 45 min. c) Slow light curve of W1 waveguides, from the same sample as b), treated for 90 min.

also showed signs of overengineering, consistent with theoretical calculations for an increase in hole diameter (assuming other parameters remain constant), as shown in fig. 86.

On the same sample, the photonic wire loss was measured, showing unexpected behaviour. As shown in fig. 86, the loss for different treatment times shows an initial decrease with treatment time, before then increasing again, in good agreement with results on PhC cavities (fig. 82). However, the untreated sample has the lowest propagation loss. The slow light data for the PhC waveguides on this sample also shows a dependence on the treatment time, consistent with previous results, except for the 10 min treatment time. The curve for this sample is expected to lie between the untreated and 30 min exposure curves, however it does not. This indicates that the hydrogen treatment has removed more silicon from the holes than expected, and more than for the next sample (longer exposure). However, more importantly, the propagation loss for this sample was not improved through hydrogen treatment. Instead, this and other measurements show a clear trend. After hydrogen treatment, the propagation loss of wide waveguides is around $4 - 8$ dB/cm, independent of the initial wire loss. Therefore, wires with high initial roughness are improved, while high quality pho-

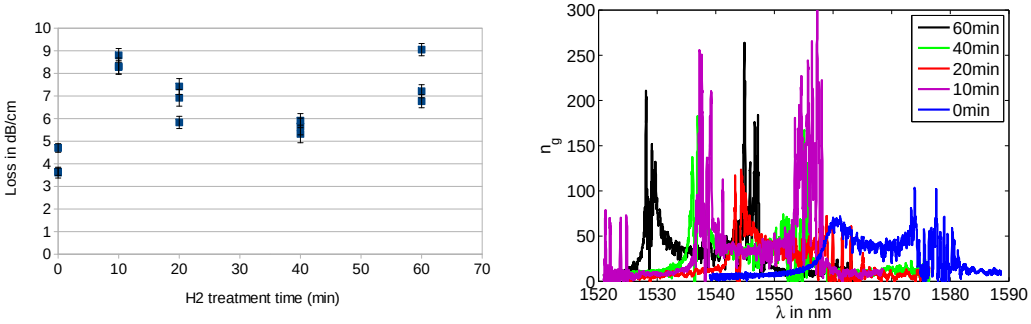

(a) (b)

Figure 86: **a)** Graph showing propagation loss for different H_2 plasma treatment times. While the results for the treated waveguides are in agreement with the behaviour observed for cavity Q-factors (fig. 82), the untreated waveguides exhibit the lowest propagation loss, contradicting the cavity results. **b)** Graph showing the group index curve for Hydrogen treated waveguides. All waveguides had an identical design. The shift to lower wavelength and increase in the peak group index is consistent with a increase in the hole radius of these waveguides.

tonic wires end up worse then before. While this result sounds very strange initially, it can be understood when considering other effects of the hydrogen treatment.

Strong photo and electro luminescence, over wide wavelength regions, has been observed in hydrogen plasma treated cavities. A structure showing emission at a certain wavelength regions will also absorb in the same wavelength region. Therefore, the hydrogen treated silicon can be expected to absorb some of the light propagating through it. For waveguides that initially have a low surface roughness, the increased loss through absorption will outweigh any improvement of the silicon/air interface. However, for waveguides with initially high surface roughness, and therefore high propagation loss, the reduction of propagation loss through a smoother silicon/air interface outweighs the absorption introduced during the plasma treatment, resulting in lower propagation loss. However, through good control of the lithography and etching conditions high quality waveguides can already be fabricated and a process that carries the risk of significantly increasing propagation loss should not be introduced into the fabrication flow.

However, during this experiment an additional effect was observed. The regions treated with the hydrogen plasma area clearly visible under an optical microscope, through a change in colour. At this point it is not clear if this change is due to a change in the silicon thickness or the refractive index. However, the exposed areas showed waveguiding behaviour and a propagation loss measurement was possible, as shown in fig. 87. After initial measurements of the waveguide propagation loss, the sample was heated to 450°C for 1 hour, as A. Shakoor

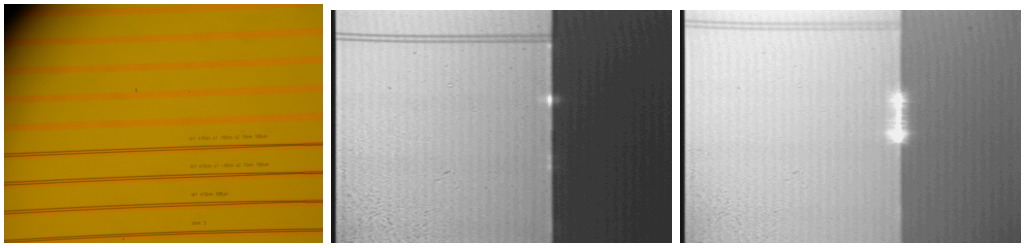

(a) (b) (c)

H_2 treatment time	Propagation loss in	Standard Deviation	Standard error
40 min	13.5 dB/cm	2.6 dB/cm	0.36 dB/cm
60 min	14.6 dB/cm	5.4 dB/cm	0.86 dB/cm

(d)

Figure 87: **a)** Optical microscope image showing the colour difference between hydrogen treated (orange) and untreated (green) areas. **b)** IR camera image of light being guided through a hydrogen treated region. **c)** Light confined between two hydrogen treated regions. The hydrogen treated regions are $30 - 40\,\mu$m wide and at $100\,\mu$m intervals. **d)** Table showing propagation loss through the hydrogen treated areas for two different samples. 3 "waveguides" were measured for each sample.

previously showed that this process removes hydrogen trapped in the silicon layer. Subsequently, the plasma treated regions were still visible under the optical microscope, but now no optical measurement was possible, indicating that the waveguiding effect is most likely due to a combination of both a refractive index change (due to the inclusion of hydrogen) and a slight reduction in thickness.

5.2.3 Surface oxidation

The final method for the reduction of surface roughness that was investigated is a controlled oxidation of silicon. During this step, any surface roughness remains on the outside of the oxide layer, leading to a smooth silicon/oxide interface. The thin oxide layer can then be removed through a short (> 30 s) HF etch. The oxidation is performed at around 900°C. After the HF etch, the silicon layer is significantly thinner than before, and the hole diameter is increased, as shown in fig. 88. As during the hydrogen treatment step, the increased hole diameter (and reduced slab thickness) leads to a blue shift of the PhC operating wavelength. After oxidation, and the subsequent HF etch, the propagation loss of the access waveguides had increased, as shown in fig. 89. This initially seems to contradict the theory that the oxidation procedure reduces the sidewall roughness. While this is a possibility, it is unlikely as the SEM images of the oxidised samples show smooth sidewalls. An alternative description is that the sample facet, or other parts of the waveguides, sustained damage

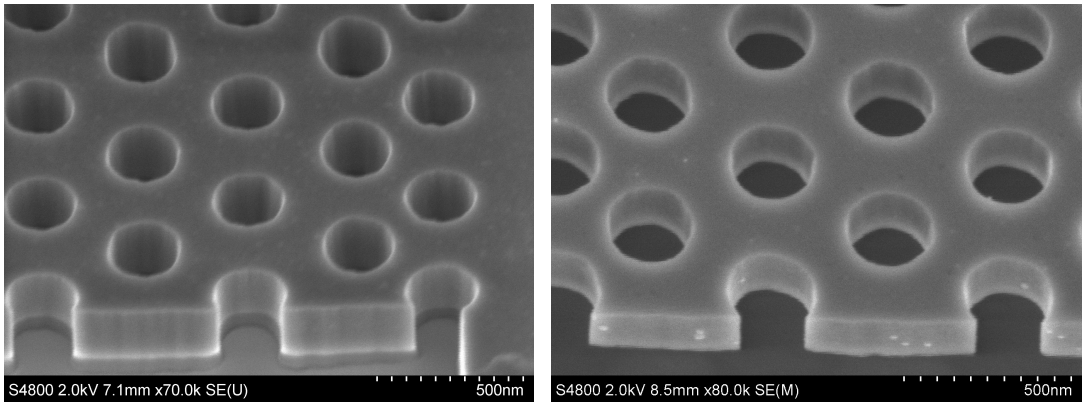

(a) (b)

Figure 88: SEM images of the same PhC **a)** before and **b)** after oxidation (10 min) and HF etch. The oxidised sample has a larger air hole diameter and a thinner silicon slab. These changes will have to be compensated for in the design and fabrication process, to achieve the desired slow light properties.

during the additional processing steps. Normally, the cleave of the optical facets is the last step in the fabrication process, to avoid contamination or damage of this region. However, the effectiveness of the oxidation procedure can best be evaluated by measuring the same waveguides before and after the process. This required a cleave before the first measurement, and therefore the facets were exposed to potential damage/contaminants during the oxidation and HF procedure. This theory is supported by the fact that transmission could be achieved through fewer devices than before the oxidation, and the coupled power was generally lower, indicating lower quality facets.

5.3 Conclusion

In this Chapter, I have presented several methods for the reduction of surface roughness and stitching errors during PhC fabrication. The reduction of surface roughness through post processing steps is in principle possible, however, the precise process control required is difficult to achieve. Each of the processes presented has some advantages and disadvantages. Annealing the sample in either hydrogen or nitrogen requires the least additional process steps, however the high temperatures required place restrictions on the CMOS compatibility of this process. Furthermore, the end result is very sensitive to sample contamination and the required control over process parameters could not be achieved with the available equipment. Hydrogen plasma treatment promised a fully CMOS compatible method, however it involves an additional lithography step, increasing fabrication time and cost, and only results in, at

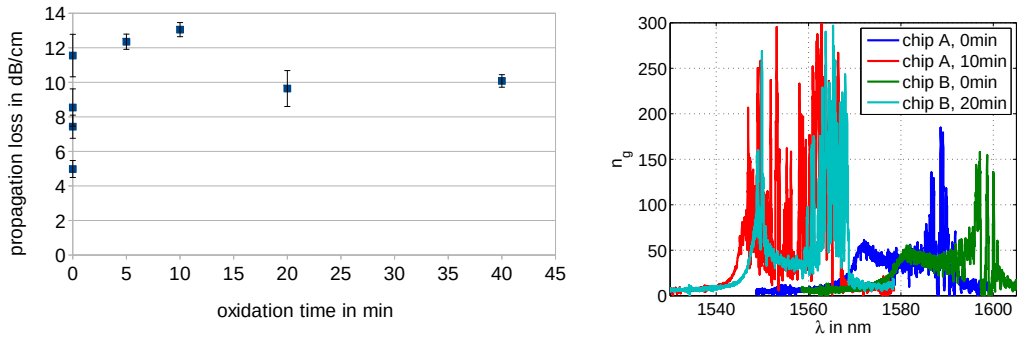

(a) (b)

Figure 89: a) Access waveguide propagation loss for different oxidation times. There are 4 different values at $t = 0$, as four different samples were measured. These samples were measured again after treatment and the propagation loss had increased for all waveguides. b) Group index curves for two samples. For both samples the increase of hole radius, and thinning of the Si slab, lead to a blue shift (25 nm and 31 nm for chips A and B respectively) and increased peak group index, as was observed for the H_2 treatment (fig. 86).

best, medium quality waveguides. The controlled oxidation of the surfaces and subsequent removal of the oxide layer has the most potential and has been investigated most in the past. However, within the time frame of this project, no definitive results were achieved, as it is not clear if the changes in the access waveguide propagation loss were due to mechanical damage or changes in the optical properties, and therefore further work is required.

Shot shifting, successfully demonstrated for photonic wires, was shown to be unsuitable for PhC fabrication, due to the internal control systems of the e-beam writer used, and the large drift present during the required exposure time. However, slow-fast-slow mode conversion interfaces were developed, which avoid the slow light enhancement of the stitching error losses, significantly reducing the propagation loss in the slow light regime.

6 Conclusion

"Habe nun, ach! Philosphie,

Juristerey und Medicin,

Und leider auch Theologie!

Durchaus studirt, mit heißem Bemühn.

Da steh' ich nun, ich armer Thor!

Und bin so klug als wie zuvor"

Faust, 354 ff- Johann W. von Goethe

6.1 Results

In this thesis, I have shown the results achieved during my PhD project and their impact on slow light applications. The first, and most important, results of this work were on the theoretical understanding of propagation loss in photonic crystal waveguides.

1. Through a combined theoretical and experimental study, the importance of the coherence length parameter in the calculation of PhC propagation loss was studied in detail. This study showed that the coherence length has a much stronger effect on the propagation loss curve than previously expected. A single hole coherence length was shown to yield the best agreement between experimental and theoretical propagation loss. Through this result, the previously existing misconceptions, and disagreements, over the scaling of propagation loss in slow light PhC waveguides were resolved.

2. Based on the above result, an efficient method for the calculation of ensemble averaged properties of PhC waveguides was developed, and our implementation was made available for free, under the GPL license. This implementation requires only a single calculation of the electro-magnetic fields in an ideal, non-disordered structure. Through appropriate assumptions on the average properties of fabrication disorder, the propagation loss can be calculated from these fields. The assumptions are that roughness is only present on etched surfaces and that, on average, it is completely described by a rms value (σ), the coherence length (l_c) and the difference in dielectric constant between the hole and slab material, $\Delta\epsilon$.

3. It was shown, both experimentally and theoretically, that photonic crystal design has a major impact on the propagation loss. While previous studies have shown that the waveguide width has an impact on propagation loss, my work represents the first study during which small changes in hole position and/or radius were used to achieve a reduction in propagation loss. Additionally, a comparison of different waveguide designs showed that the group index is not the key parameter that determines propagation loss. While the loss is clearly dependent on the group index, one also needs to take the mode field distribution into account, which can dominate over the group index scaling.

4. The calculation method was adapted for the calculation of propagation loss in slotted PhC waveguides. Here, the coherence length of the disorder inside the slot was assumed to be equal to that on a photonic wire sidewall (around 40 nm). An initial study of the dependence of propagation loss on slot width showed qualitative agreement between measured and simulated data.

5. Theoretical and experimental data on overengineered waveguides shows that multiple wavelength values can have the same group index, but with varying propagation loss. Therefore, the concept of propagation loss as a function of group index, according to the mathematical definition of a function, has been shown to be flawed. A representation of propagation loss against group index is very useful when choosing a waveguide design for a specific application. However, during device design, and when investigating fundamental effects in photonic crystal waveguides, both the propagation loss and group index should be viewed as a function of the wavevector k. This approach showed us the importance of an increased overlap, in k-space, between the low backscatter and low dispersion regions.

6. Through a combination of the results stated above and a study of the spatial dependence of backscattering within a photonic crystal waveguide, design rules for low loss waveguides were derived. These rules are:

   (a) The minima in backscattering from the first and second row should be as close together as possible.

   (b) The maximum in scattering from the second row should be reduced, without leading to an increased distance between the backscattering minima.

(c) The low dispersion and low backscattering regions of the bandstructure must overlap (in k-space), to achieve a reduction of propagation loss at the optimum operating point for a PhC waveguide based device.

7. Using the above design rules, PhC waveguides can be designed for different applications. Here, it is crucial to remember that most applications not only require a low propagation loss, but place demands on other parameters, too. As these demands vary between different applications, no "best" waveguide or "one fits all" solution exists. Instead, different devices should be designed for each application. It was shown that carefully designed loss engineered waveguides offer significant improvements for SRS and FWM applications.

8. The first loss engineered waveguides were used to demonstrated the lowest loss per unit time in a nanophotonic silicon circuit. For an accurate comparison, ring resonator (RR) and PhC based delay lines were fabricated and measured, using the same platforms. The PhC based delay lines showed a propagation loss of 35 dB/ns, compared to 60 dB/ns for RR based structures. Further improvement in the propagation loss has been predicted, with some theoretical calculations showing a propagation loss around 20 dB/ns in silicon PhC, approaching values otherwise only achieved in low refractive index contrast systems.

9. A study of different post processing methods showed that a further reduction in the roughness of etched surfaces is possible. However, the process control required for reliable, high yield processing could not be achieved.

10. The use of slow-fast-slow sections, similar to the mode conversion coupling interfaces, avoids the slow light enhancement of light scattering from stitching errors. This result allowed propagation loss measurements using very small writefields and, when combined with the design rules presented above, lead to low propagation loss, 130dB/cm, at $n_g = 60$. Here, the slow-fast-slow interfaces reduced propagation loss by around 150 dB/cm, while loss engineering resulted in a reduction of the propagation loss by an order of magnitude, compared to a standard W1 waveguide.

From the above list, we can see that while some progress was made in the improvement of photonic crystal fabrication, the biggest reduction of propagation loss is due to appropriate waveguide design. The design based approach is much more reliable than any of the post

processing steps investigated here, providing us with a promising new approach for the design and fabrication of application-specific low loss waveguides.

6.2 Further work

While significant progress has been made on the reduction of propagation loss, the end is not yet in sight. Several points investigated during this project can be improved further, through additional research.

On the design of photonic crystal waveguides, research focused on the demands of individual applications is needed. As shown theoretically for FWM (by J. Li) and Raman scattering (by I. H. Rey), as well as experimentally for FWM (by J. Li), identifying the impact of different parameters, such as group index, propagation loss, mode area etc., on a process efficiency is crucial. Studies as those by J. Li and I. H. Rey should be repeated, for other nonlinear processes. Once the impact of each parameter has been understood properly, a PhC waveguide with suitable performance parameters can be designed.

Although the combination of different engineering parameters, such as a lateral shift of holes and a reduction of the second row radius, has been investigated, further work on this topic is justified. Due to the large number of available parameters, many parameter combinations are imaginable and could potentially lead to further reductions in propagation loss.

During this project, work was focused on PhCs in a silicon membrane. However, PhCs in a variety of other material systems have been demonstrated. These systems include oxide clad PhC (where the PhC is covered by an oxide layer), III/V semiconductors and novel materials, such as chalcogenide glasses. The concept of loss engineering can easily be applied to all these systems, combining the advantages of low loss designs with favourable material properties.

Propagation loss in slotted waveguides is still poorly understood. For initial calculations, it was assumed that the disorder on the slot has the same σ value, but a different coherence length as the disorder on the PhC holes. A comprehensive study, including measurements of propagation loss at different group indices, for different slot widths and different PhC designs is need, to clarify the free parameters. The relative importance, and size, of the disorder on the slot and holes has not been explored properly. The value of propagation loss for different group indices is needed, to investigate the effect of coherence length on the slot

roughness, as was done for normal waveguides in chapter 3. Once these parameters have been clarified, the development of loss engineered slotted waveguides can begin, bringing the advantages of low propagation loss to these exciting devices and new applications.

Some of the post processing methods, aimed at reducing the surface roughness, also warrant further investigation. Annealing of silicon in an oxygen free atmosphere showed promising results, with significant rounding of waveguide edges and reduction in the surface roughness visible on some devices. However, high quality annealing equipment is required, and the impact of different atmospheres, both different gas composition as well as pressure, needs to be investigated. The impact of the changed shape of the PhC slab and holes on the group index, and ρ, curves should be investigated and design procedures adapted accordingly.

The oxidisation of silicon, and subsequent removal of the oxide layer should also be investigated further. Here, the repeatability of the process must be investigated and the effect of using ambient air vs different oxygen concentrations should be investigated. Additionally, the impact of the gas pressure is still unknown. Once again the PhC design process must be adapted, as the oxidation process thins the PhC membrane and increases hole diameter.

6.3 Summary

At the beginning of this thesis, I stated that slow light waveguides, based on PhCs, have the potential to be a key component of integrated photonic circuits. Furthermore, propagation loss was stated to be the limiting factor for such slow light waveguides. However, as we saw in chapter 4, no "best" or "one fits all" PhC waveguide exists and application-specific waveguide designs are required instead. In the same fashion slow light waveguides are no "one fits all" solution either. During circuit design, a critical assessment of the requirement for each individual component is necessary. Only then can a suitable device be fabricated.

For all integrated circuits, and devices within, a trade off between different operating parameters, such as the final footprint, required input power, operating efficiency (e.g. achievable delay or a nonlinear efficiency) as well as the output power is required. Depending on the relative importance of these parameters different devices, such as cavities, photonic nanowires or slow light waveguides, should be used.

Considering, for example, the case of FWM already discussed in section 4.5.1, if compactness is a key parameter, then coupled cavities are best, but if the overall efficiency for

the given input power should be maximised, then a long photonic nanowire will give the best result. However, if both a small footprint and a reasonable bandwidth are required, then a slow light PhC waveguide, operated at the highest n_g possible with the necessary bandwidth, should be used, to maximise the reduction in footprint.

From the results presented in this thesis, and the discussion above, we can see that propagation loss in photonic crystal waveguides can be reduced sufficiently, to enable applications based on slow light photonic crystal waveguides. Therefore, we can expect loss and dispersion engineered waveguides to take their place in the integrated photonics toolkit and to be used for a range of applications.

References

[1] T.F.Krauss, "Why do we need slow light?," *Nature Photonics*, vol. 2, p. 448, 2006.

[2] T.Baba, "Slow light in photonic crystals," *Nature Photonics*, vol. 2, p. 465, 2008.

[3] D. M. Beggs, T. P. White, L. O'Faolain, and T. F. Krauss, "Ultracompact and low-power optical switch based on silicon photonic crystals," *Opt. Lett.*, vol. 33, p. 147, Jan 2007.

[4] T.Baba, T.Kawasaki, H.Sasaki, J.Adachi, and D.Mori, "Large delay-bandwidth product and tuning of slow light pulse in photonic crystal coupled waveguide," *Optics Express*, vol. 16, p. 9245, 2008.

[5] M.Notomi, E.Kuramochi, and T.Tanabe, "Large-scale arrays of ultrahigh-q coupled nanocavities," *Nature Photonics*, vol. 2, p. 741, 2008.

[6] J. F. McMillan, X. Yang, N. C. Panoiu, R. M. Osgood, and C. W. Wong, "Enhanced stimulated raman scattering in slow-light photonic crystal waveguides," *Opt. Lett.*, vol. 31, pp. 1235–1237, May 2006.

[7] B. Corcoran, C. Monat, C. Grillet, D. J. Moss, B. J. Eggleton, T. P. White, L. O'Faolaine, and T. F. Krauss, "Green light emission in silicon through slow-light enhanced third-harmonic generation in photonic-crystal waveguides," *Nature Photonics*, vol. 3, p. 206, 2009.

[8] C. Monat, M. Ebnali-Heidari, C. Grillet, B. Corcoran, B. J. Eggleton, T. P. White, L. O'Faolain, J. Li, and T. F. Krauss, "Four-wave mixing in slow light engineered silicon photonic crystal waveguides," *Opt. Express*, vol. 18, pp. 22915–22927, Oct 2010.

[9] J. Li, L. O'Faolain, I. H. Rey, and T. F. Krauss, "Four-wave mixing in photonic crystal waveguides: slow light enhancement and limitations," *Opt. Express*, vol. 19, pp. 4458–4463, Feb 2011.

[10] B. Little, J. Foresi, G. Steinmeyer, E. Thoen, S. Chu, H. Haus, E. Ippen, L. Kimerling, and W. Greene, "Ultra-compact si-sio2 microring resonator optical channel dropping filters," *Photonics Technology Letters, IEEE*, vol. 10, pp. 549 –551, apr 1998.

[11] Y. Akahane, T. Asano, B.-S. Song, and S. Noda, "High-q photonic nanocavity in a two-dimensional photonic crystal," *Nature*, p. 944, 2003.

[12] J. Li, T. P. White, L. O'Faolain, A. Gomez-Iglesias, and T. F. Krauss, "Systematic design of flat band slow light in photonic crystal waveguides," *Optics Express*, vol. 16, pp. 6227–6232, 2008.

[13] A. Melloni, A. Canciamilla, C. Ferrari, F. Morichetti, L. O'Faolain, T. F. Krauss, R. D. L. Rue, A. Samarelli, and M. Sorel, "Tunable delay lines in silicon photonics: Coupled resonators and photonic crystals, a comaprison," *IEEE Photonics Journal*, vol. 2, p. 181, 2010.

[14] D. M. Beggs, I. H. Rey, T. Kampfrath, N. Rotenberg, L. Kuipers, , and T. F. Krauss, "Ultrafast tunablen optical delay line based on indirect photonic transitions," *submitted to Phys. Rev. Lett.*

[15] J.Adachi, N.Ishikura, H.Sasaki, , and T.Baba, "Wide range tuning of slow light pulse in soi photonic crystal coupled waveguide via folded chirping," *Journal of Selected Topics in Quantum Electronics*, vol. 16, p. 192, 2010.

[16] T.F.Krauss, "Slow light in photonic crystal waveguides," *J. Phys. D: Appl. Phys.*, vol. 40, p. 2666, 2007.

[17] L. O'Faolain, D. M. Beggs, T. P. White, T. Kampfrath, K. Kuipers, and T. F. Krauss, "Compact optical switches and modulators based on dispersion engineered photonic crystals," *IEEE Photonics Journal*, vol. 2, p. 404, 2010.

[18] T. Tanabe, M. Notomi, A. Shinya, S. Mitsugi, and E. Kuramochi, "All-optical switch using photonic crystal nanocavity." website, March 2012.

[19] C. Monat, B. Corcoran, M. Ebnali-Heidari, C. Grillet, B. J. Eggleton, T. P. White, L. O'Faolain, and T. F. Krauss, "Slow light enhancement of nonlinear effects in silicon engineered photonic crystal waveguides," *Opt. Express*, vol. 17, pp. 2944–2953, Feb 2009.

[20] C. Monat, M. de Sterke, and B. J. Eggleton, "Slow light enhanced nonlinear optics in periodic structures," *Journal of Optics*, vol. 12, p. 104003, 2010.

[21] I. H. Rey, Y. Lefevre, S. A. Schulz, N. Vermeulen, and T. F. Krauss, "Scaling of raman amplification in realistic slow-light photonic crystal waveguides," *Phys. Rev. B*, vol. 84, p. 035306, Jul 2011.

[22] M. Notomi, T. Tanabe, A. Shinya, E. Kuramochi, H. Taniyama, S. Mitsugi, and M. Morita, "Nonlinear and adiabatic control of high-q photonic crystal nanocavities," *Optics Express*, vol. 15, p. 17458, 2007.

[23] T. Tanabe, K. Nishiguchi, E. Kuramochi, and M. Notomi, "Low power and fast electro-optic silicon modulator with lateral p-i-n embedded photonic crystal nanocavity," *Opt. Express*, vol. 17, pp. 22505–22513, Dec 2009.

[24] M. Scullion, A. D. Falco, and T. Krauss, "Slotted photonic crystal cavities with integrated microfuidics for biosensing applications," *Biosensors and Bioelectronics*, vol. 27, pp. 101–105, 2011.

[25] F. M. Andrea Melloni, "The long march of slow photonics," *Nature Photonics*, vol. 3, p. 119, 2009.

[26] E. Yablonovitch, "Inhibited spontaneous emission in solid-state physics and electronics," *Physical Review Letters*, vol. 58, p. 2059, 1987.

[27] S. John, "Strong localization of photons in certain disordered dielectric superlattices," *Physical Review Letters*, vol. 58, p. 2486, 1987.

[28] T. F. Krauss, R. M. D. L. Rue, and S. Brand, "Two-dimensional photonic-bandgap structures operating at near-infrared wavelengths," *Nature*, vol. 383, p. 699, 1996.

[29] J. D. Joannopolous, S. G. Johnson, J. N. Winn, and R. D. Meade, *Photonic crystals: Molding the flow of light.* princeton university press, 2nd ed., 2008.

[30] M. Notomi, K. Yamada, A. Shinya, J. Takahashi, C. Takahashi, and I. Yokohama, "Extremely large group-velocity dispersion of line-defect waveguides in photonic crystal slabs," *Phys. Rev. Lett.*, vol. 87, p. 253902, Nov 2001.

[31] M. Loncar, D. Nedeljkovic, T. Doll, J. Vuckovic, and A. S. et al., "Waveguiding in planar photonic crystals," *Applied Physics Letters*, vol. 77, p. 1937, 2000.

[32] S. Olivier, M. Rattier, H. Benisty, C. Weisbuch, C. J. M. Smith, R. M. D. L. Rue, T. F. Krauss, U. Oesterle, and R. Houdre, "Mini-stopbands of a noe-dimensional system:

The channel waveguide in a two-dimensional photonic crystal," *Phys. Rev. B*, vol. 63, p. 113311, 2001.

[33] S. A. Schulz, L. O'Faolain, D. M. Beggs, T. P. White, A. Melloni, and T. F. Krauss, "Dispersion engineered slow light in photonic crystals: a comparison," *Journal of Optics*, vol. 12, p. 104004, 2010.

[34] A.Y.Petrov and M.Eich, "Zero dispersion at small group velocities in photonic crystal waveguides," *Applied Physics Letters*, vol. 85, p. 4866, 2004.

[35] L.H.Frandsen, A.V.Lavrinenko, J.Fage-Pedersen, and P.I.Borel, "Photonic crystal waveguides with semi-slow light and tailored dispersion properties," *Optics Express*, vol. 14, p. 9444, 2006.

[36] Y.Hamachi, S.Kubo, and T.Baba, "Low dispersion slow light and nonlinearity enhancement in lattice-shifted photonic crystal waveguide," in *QTuC1.pdf*, OSA / CLEO/QELS 2008, 2008.

[37] E. Kuramochi, M. Notomi, S. Hughes, A. Shinya, T. Watanabe, and L. Ramunno, "Disorder-induced scattering loss of line-defect waveguides in photonic crystal slabs," *PHYSICAL REVIEW B*, vol. 72, p. 161318, 2005.

[38] L.O'Faolain, T.P.White, D.O'Brien, X.Yuan, M.D.Settle, and T.F.Krauss, "Dependence of extrinsic loss on group velocity in photonic crystal waveguides," *Optics Express*, vol. 15, p. 13129, 2007.

[39] L. O'Faolain, X. Yuan, D. Mcintyre, S. Thoms, H. Chong, R. M. D. L. Rue, and T. F. Krauss, "Low-loss propagation in photonic crystal waveguides," *Electronics Letters*, vol. 42, p. 1454, 2006.

[40] K. Okamoto, "Progress and technical challenges for integrated optics," No. JTuA1 in OSA/ANIC/IPR/Sensors/SL/SOF/SPPCom/2011, (Washington DC), Optical society of America, 2011.

[41] D. F. Kyser and N. S. Viswanathan, "Monte carlo simulation of spatially distributed beams in electron-beam lithography," *Journal of Vacuum Science and Technology*, vol. 12, pp. 1305 –1308, nov 1975.

[42] T. P. White, L. O'Faolain, J. Li, L. C. Andreani, and T. F. Krauss, "Silica-embedded silicon photonic crystal waveguides," *Opt. Express*, vol. 16, pp. 17076–17081, Oct 2008.

[43] S.-W. Jeon, J. kyu Han, B.-S. Song, and S. Noda, "Glass-embedded two-dimensional silicon photonic crystal devices with a broad bandwidth waveguide and a high quality nanocavity," *Opt. Express*, vol. 18, pp. 19361–19366, Aug 2010.

[44] J. G. Goodberlet, J. T. Hastings, and H. I. Smith, "Performance of the raith 150 electron-beam lithography system," *journal of Vacuum Science Technology B*, vol. 19, p. 2499, 2001.

[45] G. Pagnotta, "Stitching-error reduction in photonic crystals and photonic wires by shot-shifted electron beam lithography," Master's thesis, Politecnico di Torino, University of St Andrews, 2006.

[46] Y.A.Vlasov and S.J.McNab, "Coupling into the slow light mode in slab-type photonic crystal waveguides," *Optics Letters*, vol. 31, p. 50, 2006.

[47] N.Ozaki, Y.Kitagawa, Y.Takata, N.Ikeda, Y.Watanabe, A.Mizutani, Y.Sugimoto, and K.Asakawa, "High transmission recovery of slow light in a photonic crystal waveguide using a hetero groupvelocity waveguide," *Optics Express*, vol. 15, p. 7974, 2007.

[48] J.P.Hugonin, P.Lalanne, T.P.White, and T.F.Krauss, "Coupling into slow-mode photonic crystal waveguides," *Optics Letters*, vol. 32, p. 2638, 2007.

[49] T.P.White, L.C.Botten, C. Sterke, K.B.Dossou, and R.C.McPhedran, "Efficient slow-light coupling in a photonic crystal waveguide without transition region," *Optics Letters*, vol. 33, p. 2644, 2008.

[50] S. Ha, M. Spasenović, A. A. Sukhorukov, T. P. White, C. M. de Sterke, L. K. Kuipers, T. F. Krauss, and Y. S. Kivshar, "Slow-light and evanescent modes at interfaces in photonic crystal waveguides: optimal extraction from experimental near-field measurements," *J. Opt. Soc. Am. B*, vol. 28, p. 955, 2011.

[51] C. J. M. Smith, H. Benisty, S. Olivier, M. Rattier, C. Weisbuch, T. F. Krauss, R. M. D. L. Rue, R. Houdre, and U. Oesterle, "Low-loss channel waveguide with two-dimensional photonic crystal boundaries," *Applied Physics Letters*, vol. 77, p. 2813, 2000.

[52] S. Mazoyer, J. P. Hugonin, and P. lalanne, "Disorder-induced multiple scattering in photonic-crystal waveguides," *Physical Review Letters*, vol. 103, p. 063903, 2009.

[53] D. Hofstetter and R. L. Thornton, "Theory of loss measurements of fabry perot resonators by fourier analysis of the transmission spectra," *Opt. Lett.*, vol. 22, pp. 1831–1833, Dec 1997.

[54] M. V. Kotylar, T. Karle, M. D. Settle, L. O'Faolain, and T. F. Krauss, "Low-loss photonic crystal defect waveguides in inp," *Applied Physics Letters*, vol. 84, p. 3588, 2004.

[55] M. V. Kotlyar, *Photonic Crystal Waveguides and Tunable filters in InP*. PhD thesis, University of St Andrews, 2005.

[56] R. Jacobsen, A. Lavrinenko, L. Frandsen, C. Peucheret, B. Zsigri, G. Moulin, J. Fage-Pedersen, and P. Borel, "Direct experimental and numerical determination of extremely high group indices in photonic crystal waveguides," *Opt. Express*, vol. 13, pp. 7861–7871, Oct 2005.

[57] I. Ïnanç Tarhan, M. P. Zinkin, and G. H. Watson, "Interferometric technique for the measurement of photonic band structure in colloidal crystals," *Opt. Lett.*, vol. 20, pp. 1571–1573, Jul 1995.

[58] M. Galli, D. B. F. Marabelli, L. C. Andreani, L. Pavesi, and G. Pucker, "Photonic bands and group-velocity dispersion in si/sio2 photonic crystals from white-light interferometry," *Phys. Rev. B*, vol. 69, p. 115107, 2004.

[59] Y. A. Vlasov, M. O'Boyle, H. F. Hamann, and S. J. McNab, "Active control of slow light on a chip with photonic crystal waveguides," *Nature*, vol. 438, pp. 65–69, 2005.

[60] A. Gomez-Iglesias, D. O'Brien, L. O'Faolain, A. Miller, and T. F. Krauss, "Direct measurement of the group index of photonic crystal waveguides via fourier transform spectral interferometry," *Appl. Phys. Lett.*, vol. 90, p. 261107, 2007.

[61] J.G.Pedersen, S.Xiao, and N.A.Mortensen, "Limits of slow light in photonic crystals," *Physical Review B*, vol. 78, p. 153101, 2008.

[62] S. Mazoyer, A. Baron, J.-P. Hugonin, P. Lalanne, and A. Melloni, "Slow pulses in disordered photonic-crystal waveguides," *Applied Optics*, vol. 50, p. G113, 2011.

[63] M. Notomi, A. Shinya, K. Yamada, J. ichi Takahashi, C. Takahashi, and I. Yokohama, "Structural tuning of guiding modes of line-defect waveguides of silicon-on-insulator photonic crystal slabs," *IEEE Journal of Quantum Electronics*, vol. 38, p. 736, 2002.

[64] M.Notomi, A.Shinya, S.Mitsugi, E.Kuramochi, and H-Y.Ryu, "Waveguides, resonators and their coupled elements in photonic crystal slabs," *Optics Express*, vol. 12, p. 1551, 2004.

[65] M. Gnan, S. Thoms, D. Macintyre, R. D. L. Rue, and M. Sorel, "Fabrication of low-loss photonic wires in silicon-on-insulator using hydrogen silsesquioxane electron-beam resist," *Electronics Letters*, vol. 44, p. 115, 2008.

[66] S. Hughes, L. Ramunno, J. F. Young, and J. E. Sipe, "Extrinsic optical scattering loss in photonic crystalwaveguides: Role of fabrication disorder and photon group velocity," *Phys. Rev. Lett.*, vol. 94, p. 033903, 2005.

[67] S. JOHNSON, M. POVINELLI, M. SOLJACIC, A. KARALIS, S. JACOBS, and J. JOANNOPOULOS, "Roughness losses and volume-current methods in photonic-crystal waveguides," *Applied Physics B*, vol. 81, p. 283, 2005.

[68] L.C.Andreani and D.Gerace, "Light-matter interaction in photonic crystal slabs," *Physica Status Solidid b*, vol. 244, p. 3528, 2007.

[69] M. Patterson, S. Hughes, S.Combrie, N.-V.-Q. Tran, A. D. Rossie, R. Gabet, and Y. Jaouen, "Disorder-induced coherent scattering in slow-light photonic crystalwaveguides," *Physical Review Letters*, vol. 102, p. 253903, 2009.

[70] M. Patterson and S. Hughes, "Theory of disorder-induced coherent scattering and light localization in slow-light photonic crystal waveguides," *Journal of Optics*, vol. 12, p. 104013, 2010.

[71] S. Johnson and J. Joannopoulos, "Block-iterative frequency-domain methods for maxwell's equations in a planewave basis," *Opt. Express*, vol. 8, pp. 173–190, Jan 2001.

[72] D. Gerace and L. C. Andreani, "Disorder-induced losses in photonic crystal waveguides with line defects," *Opt. Lett.*, vol. 29, pp. 1897–1899, Aug 2004.

[73] B. Wang, S. Mazoyer, J. P. Hugonin, and P. Lalanne, "Backscattering in monomode periodic waveguides," *Physical Review B*, vol. 78, p. 245108, 2008.

[74] A.Petrov, M.Krause, and M.Eich, "Backscattering and disored limits in slow light photonic crystal waveguides," *Optics Express*, vol. 17, p. 8676, 2009.

[75] M. Patterson, "Classical and quantum optical properties of slow light photonic crystal waveguides," Master's thesis, Queen's University, Kingston, Ontario, Canada, August 2009.

[76] G. Lecamp, J. P. Hugonin, and P. Lalanne, "Theoretical and computational concepts for periodic optical waveguides," *Opt. Express*, vol. 15, pp. 11042–11060, Sep 2007.

[77] M. Patterson, S. Hughes, S. Schulz, D. M. Beggs, T. P. White, L. O'Faolain, and T. F. Krauss, "Disorder-induced incoherent scattering losses in photonic crystal waveguides: Bloch mode reshaping, multiple scattering, and breakdown of the beer-lambert law," *Physical Review B*, vol. 80, p. 195305, 2009.

[78] S. Mazoyer, P. Lalanne, J. Rodier, J. Hugonin, M. Spasenović, L. Kuipers, D. Beggs, and T. Krauss, "Statistical fluctuations of transmission in slow light photonic-crystal waveguides," *Opt. Express*, vol. 18, pp. 14654–14663, Jul 2010.

[79] W. Song, R. A. Integlia, , and W. Jiang, "Slow light loss due to roughness in photonic crystal waveguides: An analytic approach," *Phys. Rev. B*, vol. 82, p. 235306, 2010.

[80] D. M. Beggs and S. A. Schulz, "http://www.st-andrews.ac.uk/microphotonics/mpblossextensioncode.php."

[81] L. O'Faolain, S. A. Schulz, D. M. Beggs, T. P. White, M. Sapsenovic, L. Kuipers, F. Morichetti, A. Melloni, S. Mazoyer, J. P. Hugonin, P. Lalanne, and T. F. Krauss, "Loss engineered slow light waveguides," *Opt. Express*, vol. 18, p. 27627, December 2010.

[82] A. Melloni, F. Morichetti, C. Ferrari, and M. Martinelli, "Continuously tunable 1 byte delay in coupled-resonator optical waveguides," *Opt. Lett.*, vol. 33, pp. 2389–2391, Oct 2008.

[83] J. Ma and C. Jiang, "Flatband slow light in asymmetric line-defect photonic crystal waveguide featuring low group velocity and dispersion," *IEEE Journal of Quantum Electronics*, vol. 44, p. 763, 2008.

[84] F. Leng, W. Liang, B. Liu, T. Wang, and H.-Z. Wang, "Wideband slow light and dispersion control in oblique lattice photonic crystal waveguides," *Optics Express*, vol. 18, p. 5707, 2010.

[85] R. Salem, M. A. Foster, A. C. Turner, D. F. Geraghty, M. Lipson, and A. L. Gaeta, "Signal regeneration using low-power four wave mixing on silicon chip," *Nature Photonics*, vol. 2, p. 35, 2008.

[86] R. Claps, D. Dimitropoulos, V. Raghunathan, Y. Han, and B. Jalali, "Observation of stimulated raman amplification in silicon waveguides," *Optics Express*, vol. 11, p. 1731, 2003.

[87] R. Espinola, J. Dadap, J. Richard Osgood, S. McNab, and Y. Vlasov, "Raman amplification in ultrasmall silicon-on-insulator wire waveguides," *Opt. Express*, vol. 12, pp. 3713–3718, Aug 2004.

[88] A. S. Liu, H. S. Rong, R. Jones, O. Cohen, D. Hak, and M. Paniccia, "Optical amplification and lasing by stimulated raman scattering in silicon waveguides," *Journal of Lightwave Technology*, vol. 24, p. 1440, 2006.

[89] A. D. Falco, L. O'Faolain, and T. Krauss, "Photonic crystal slotted slab waveguides," *Photonicd and Nanostructures - Fundamentals and Applications*, vol. 6, p. 38, 2008.

[90] A. D. Falco, L. O'Faolain, and T. Krauss, "Dispersion control and slow light in slotted photonic crystal waveguides," *Appl. Phys. Lett.*, vol. 92, p. 083501, 2008.

[91] T. Yamamoto, M. Notomi, H. Taniyama, E. Kuramochi, Y. Yoshikawa, Y. Torii, and T. Kuga, "Design of a high-q air-slot cavity based on a width-modulated line-defect in a photonic crystal slab," *Opt. Express*, vol. 16, pp. 13809–13817, Sep 2008.

[92] C. Barrios, "Optical slot-waveguide based biochemical sensors," *Sensors*, vol. 9, p. 4751, 2009.

[93] J. Wuelbern, J. Hampe, A. Petrov, M. Eich, J. Luo, A. K.-Y. Jen, A. D. Falco, T. Krauss, and J. Bruns, "Electro-optic modulation in slotted resonant photonic crystal heterostructures," *Appl. Phys. Lett.*, vol. 94, p. 241107, 2009.

[94] G. Pagnotta, L. O'Faolain, D. O'Brien, and T. F. Krauss, "Shot shifting for nanophotonic applications," *Microelectronic Engineering*, vol. 84, p. 1466, 2007.

[95] "Imagej." http://rsb.info.nih.gov/ij/.

[96] R. G. M. Berse. Personal Correspondance, November 2009.

[97] J. Li, L. O'Faolain, S. A. Schulz, and T. F. Krauss, "Low loss propagation in slow light photonic crystal waveguides at group indices up to 60," *submitted to Photonicd and Nanostructures - Fundamentals and Applications.*

[98] M.-C. M. Lee and M. C. Wu, "Thermal annealing in hydrogen for 3-d profile transformation on silicon-on-insulator and sidewall roughness reduction," *Journal of Microelectromechanical Systems*, vol. 15, p. 338, 2006.

[99] M.-C. M. Lee, W.-C. Chiu, T.-M. Yang, and C.-H. Chen, "Monolithically integrated low-loss silicon photonic wires and three dimensional tapered couplers fabricated by self-profile transformation," *Appl. Phys. Lett.*, vol. 91, p. 191114, 2007.

[100] W.-C. Chiu, C.-Y. Lu, and M.-C. M. Lee, "Monolithic integration of three-dimensional multimode interference couplers with silicon photonic wires via self-profile transformation," in *Group IV Photonics*, p. 206, IEEE, IEEE, September 2008.

[101] Y. Cui, L. J. Lauhon, M. S. Gudiksen, J. Wang, and C. M. Lieber, "Diameter-controlled synthesis of single-crystal silicon nanowires," *Appl. Phys. Lett.*, vol. 78, p. 2214, 2001.

[102] Z. M. Wang, ed., *One-Dimensional Nanostructures*, vol. 3 of *Lecture Notes in Nanoscale Science and Technology.* Springer, 2008.